Monte Carlo Simulation Model for Electromagnetic Scattering from Vegetation and Inversion of Vegetation Parameters

by

Li-Fang Wang

B.S. Electrical Engineering,
Massachusetts Institute of Technology, 1990

M.S. Electrical Engineering,
Massachusetts Institute of Technology, 1992

Submitted to the Department of Electrical Engineering and Computer Science
in partial fulfillment of the requirements for the degree of

Doctor of Philosophy

at the

Massachusetts Institute of Technology

February 2007

Signature of Author ....
Department of Electrical Engineering and Computer Science
November 2006

Certified by ....
Jin Au Kong
Thesis Supervisor

Accepted by ....
Arthur C. Smith
Chairman, Department Committee on Graduate Students

Monte Carlo Simulation Model for Electromagnetic Scattering from Vegetation and Inversion of Vegetation Parameters

by

Li-Fang Wang

Submitted to the Department of Electrical Engineering and Computer Science
on November 2006, in partial fulfillment of the
requirements for the degree of
Doctor of Philosophy

Abstract

In this thesis research, a coherent scattering model for microwave remote sensing of vegetation canopy is developed on the basis of Monte Carlo simulations. An accurate model of vegetation structure is essential for the calculation of scattering from vegetations, especially those with closely spaced elements in clusters. The Monte Carlo approach has an advantage over the conventional wave theory in dealing with complex vegetation structures because it is not necessary to find the probability density functions and the pair-distribution functions required in the analytic formulation and usually difficult to obtain for natural vegetation.

To achieve a realistic description of the vegetation structure under consideration, two methods may be employed. One method requires the specification of the number of each type of component and the relative orientations of the components. In a structural model which incorporates this method, the detailed features can be preserved to the desired level of accuracy. This structural model is applied to two types of vegetation—rice crops and sunflowers. The developed structural model for rice crops takes into account the coherent wave interactions made prominent by the clustered and closely spaced structure of rice crops, and is validated with the ERS-1 and RADARSAT data. It is utilized to interpret the experimental observations from the JERS-1 data such as the effects of the structure of rice fields, and to predict the temporal response of rice growth. The structural model developed for sunflowers is validated using the airborne Remote Sensing Campaign Mac-Europe 91 multi-frequency and multi-polarization data acquired for sunflower fields at the Montespertoli test site in Italy.

Another method to characterize vegetation structure uses growth rules. This is especially useful in modeling trees, which are structurally more complex. The Lindenmayer systems (L-systems) are utilized to fully capture the architecture of trees and describe their growth. Monte Carlo simulation results of the scattering returns from trees with different structures and at different growth stages are calculated and analyzed. The concept of the "structure factor" which extracts the structural information of a tree and and provides a measure of the spatial distribution of branches is defined, and computed for trees with different architectures.

After study of the forward scattering problem in which the scattering coefficients are determined on the basis of known physical characteristics of the scattering objects or medium, the inverse scattering problem is considered in which the characteristics of the scattering objects or medium are to be calculated from the scattering data. In this thesis research, neural networks are applied to the inversion of geophysical parameters including soil moisture and surface parameters, sunflower biomass, as well as forest age (or equivalently, forest biomass). They are found to be especially useful for multi-dimensional inputs such as multi-frequency polarimetric scattering data. For the inversion of soil moisture and surface parameters, neural networks are trained with theoretical surface scattering models. To retrieve the sunflower biomass, neural networks are trained with the scattering returns obtained from the developed vegetation scattering model based on the Monte Carlo approach. To assess the performance of the use of experimental data to train the neural networks, the polarimetric radar data acquired by the Spaceborne Imaging Radar-C (SIR-C) over the Landes Forest in France are utilized as the training data to retrieve the forest age. Different combinations of backscattering data are used as input to the neural net in order to determine the combination which yields the best inversion result.

Thesis Supervisor: Jin Au Kong
Title: Professor of Electrical Engineering and Computer Science

Lai for her friendship and support. Her kindness will never be forgotten. I would like to thank Dr. Chih-Chien Hsu for his friendship and his valuable suggestions on many problems. I also want to thank Dr. Shih-En Shih and Dr. Hsiu Chi Han for their friendship. For other friends and colleagues in the group, I would like to acknowledge their friendship: Dr. Jerry Akerson, Dr. Robert Atkins, Dr. William Au, Dr. Lars Bomholt, Pierre Coutu, Makkalon Em, Hong Tat Ewe, Dr. Qizheng Gu, Tza-Jing Gung, Yoshihisa Hara, Dr. Joel Johnson, Dr. Kevin Li, Dr. Son Nghiem, Dr. John Oates, Dr. Liguo Sun, Dr. Ali Tassoudji, Nayon Tomsio, Dr. Murat Veysoglu, Chen-Pang Yeang, Dr. Yi Yuan and Yan Zhang.

Finally, I wish to express my sincere gratitude to my parents and my brother for their love, advice, unwavering support and encouragement during my undergraduate and graduate years at MIT.

Acknowledgments

I wish to thank Professor J. A. Kong for providing me with the opportunity to perform this thesis research and for his support and encouragement through the research years. His immense knowledge and enthusiasm for both research and teaching are an inspiration.

I would also like to thank Dr. Y. Eric Yang for his valuable guidance and advice. His physical insight into many problems is impressive.

I am grateful to Dr. Kung-Hau Ding for his guidance in the course of this research. He made valuable contributions by providing helpful suggestions and comments in our many discussions. I wish to express my appreciation to Dr. Robert T. Shin and other members of the remote sensing group for their comments and suggestions.

I would also like to thank Dr. T. Le Toan, Dr. Florence Ribbes and Dr. Jean-Claude Souyris at Centre d'Etude Spatiale BIOsphere (CESBIO) for ERS-1 and RADARSAT data on the rice fields, and SIR-C data on the Landes Forest in France. Their suggestions facilitate the development of the theoretical models. I also wish to thank Dr. Fabio del Frate at Università Tor Vergata for the airborne Remote Sensing Campaign Mac-Europe 91 data on the sunflower fields in Italy, and Dr. Simon Yueh for introducing me to the application of neural networks to inverse problems.

Many current and former members of our research group helped me in many ways throughout my graduate school years. I wish to thank our late secretary Kit-Wah

To my parents and my brother

Contents

List of Tables

List of Figures

Chapter 1

Introduction

1.1 Background

There have been growing interests in the microwave remote sensing of vegetations especially with recent advances of radar and satellite technology. The use of microwave frequencies for remote sensing can provide day and night coverage and is able to penetrate clouds and rain to some extent. Remote sensing data were obtained from many satellite missions such as European satellites ERS-1, ERS-2 [16], and Japanese Earth Satellite-1 (JERS-1) [49], and spaceborne imaging radar missions such as SIR-A and SIR-B [11, 15]. In 1994, Spaceborne Imaging Radar-C and X-band Synthetic Aperture Radar (SIR-C/XSAR) provided fully polarimetric data at L- and C- bands and single polarization data at X-band [71]. In addition, the RADARSAT data contains information on multiple looking angles [57]. The additional information provided by the multi-frequency polarimetric and multi-angle data is useful for the classification of vegetation type and the estimation of geophysical parameters. Since a large effort is generally needed to conduct experiments, it is important to have a more accurate physical based model for the complex earth terrain to facilitate prediction of scattering returns and interpretation of multi-frequency polarimetric radar backscattering data.

In the past, the electromagnetic scattering from the vegetation canopy has been calculated using the radiative transfer theory and the analytic wave theory [69, 74]. The radiative transfer theory is based on the energy transport equation and describes the propagation of specific intensity in the medium [73]. The analytic wave theory starts from Maxwell's equations and incorporates the scattering and absorption characteristics of the medium. Since the equations are in general complicated, solutions are obtained by making approximations. With the use of dyadic Green's functions together with approximations such as the Born approximation or distorted Born approximation [37, 38, 58], the scattered field from the medium is calculated. To characterize the random media, both the continuous random medium model [9, 17, 18, 72] and the discrete scatterer model [37, 38] have been used in the above two approaches. The continuous random medium model uses a correlation function to describe the permittivity fluctuation of the medium of interest. The key inputs to the model include variances and correlation lengths. The attenuation and phase delay of wave propagation inside the medium are taken into consideration when the effective permittivity is calculated. In the discrete scatterer model, the inhomogeneities are considered as discrete scatterers embedded in a background medium. The inputs to the model include the fractional volume, sizes, shapes, orientation distributions, and permittivities of the scatterers. More recently, the integral equation formulation with the method of moments computational model has been employed to investigate vegetation scattering [79].

In the past, wave scattering from vegetation has been studied extensively using the radiative transfer approach which assumes that particles scatter independently. It is important to take into account the coherent wave interactions among vegetative elements which are usually in clusters and closely spaced. Yueh, *et al.*[90] developed a branching model with the wave approach. However, the probability density functions and the pair-distribution functions required in their analytic formulation are usually difficult to obtain for natural vegetation. Therefore, in this thesis research, a coherent scattering model with analytic wave theory is developed based on Monte Carlo simulation for the microwave remote sensing of vegetation canopy. Unlike the branching model [90], this scattering model does not require the knowledge of the probability density functions and the pair distribution function for the vegetation under interest. Monte Carlo simulation in general is computationally intensive. However, with the rapid advances of computer technology, using Monte Carlo simulation to solve Maxwell's equations for different applications becomes more practical. It has been applied to calculate the scattering returns from the rough surface [30, 50, 77], and from densely packed spheres [76, 93]. For remote sensing of vegetation, the model takes into account of the distinctive structures of vegetations, and especially the coherent wave interactions among plant elements which are usually in clusters and closely spaced. The backscatters from the vegetation are calculated using the Monte Carlo simulation approach in which locations and characteristics of particles are supplied by computer experiments according to the ground truth characterizations. These simulated scenarios are utilized in solving Maxwell's equations. The developed model will be applied to vegetation such as rice crops and sunflowers, and then to trees which are more complicated in form. The developed model are validated by comparisons with airborne and/or spaceborne experimental measurements. These vegetation electromagnetic scattering models are employed to interpret the existing multi-temporal, -frequency, -looking angle, and -polarization remote sensing data.

Another important application of microwave remote sensing is to retrieve the geophysical information from the electromagnetic measurements. There has been an increasing interest in the applications of neural networks [46] to the classification of terrains and inversion of geophysical parameters in the remote sensing research community. In contrast to the conventional method which requires the inversion algorithm to be known exactly, the neural network determines the relationship between the input to the network and output from the network directly from the training data. It is especially useful for the cases of parameter retrieval and classification from remote sensing data since there are many non-linear and poorly understood factors involved which make the development of the inversion algorithm difficult. The potential and capability of neural networks for dealing with complex remote sensing data have been demonstrated. For example, the classification of terrain mappings from satellite data using neural networks showed a better classification rate than the conventional statistical approach [8, 21], and a neural network trained with a theoretical scattering model has been applied to the inversion of snow parameters [75] . Neural networks are flexible for the inversion of geophysical parameters especially for multi-dimensional inputs such as multi-frequency polarimetric scattering data. Another advantage is that one does not need to make any assumption about the analytic form of the statistics of the input data. In this study, neural networks are constructed and applied to the inversion of soil moisture, sunflower biomass, and forest age.

1.2 Description of Thesis

This thesis is divided into six chapters. The motivation of doing this thesis research is given in Chapter 1. In Chapter 2, a coherent scattering model with analytic wave theory developed on the basis of the Monte Carlo simulation for microwave remote sensing of vegetation canopy is described. To calculate scattering from vegetation, it is important to be able to model the vegetation structure as accurately as possible especially for those vegetations with closely spaced elements in clusters. The Monte Carlo approach has the capability of taking the complex vegetation structures into account. It has the advantage over the conventional wave theory approach because it is not necessary to find the probability density functions and the pair-distribution functions which are required in the analytic formulation and are usually difficult to obtain for natural vegetation. The Monte Carlo approach is increasing in popularity with the fast computational speed and memory capacity of modern digital computers because the simulation of random variables is a laborious process. In the Monte Carlo simulation, the coherent wave interactions among vegetative elements are taken into account. The attenuation on the coherent wave caused by the inhomogeneities is considered as well.

To take advantage of the Monte Carlo approach, a realistic description of the vegetation structure under consideration is needed. One method to characterize the structure of vegetation is by specifying the number of each type of component and how the components are oriented with respect to one another. In Chapter 3, a structural model which incorporates this method is developed. In this structural model, the vegetation structure is characterized by levels of details. The detailed features of distinct vegetation structures can be preserved to the desired level of accuracy. In the Monte Carlo simulation, the configurations are generated from the characterization of vegetation structure. Based on the ground truth measurements, the distinct structures for different vegetations can be specified by the types of components, the number and size of each type of component, the orientation and branching angles of the individual components. The applications of the structural model to two types of vegetation are discussed. The first case is rice crops for which it is important to have a good structural model to take into account the coherent wave interactions since rice plants usually occur in clusters and are closely spaced. The developed structural model is validated with RADARSAT and ERS-1 data [41]. It is also utilized to interpret the experimental observations from JERS-1 data [61] such as the effects of the structure of rice fields, and to predict the temporal response of rice growth. In addition to the rice canopy, the application of the structural model to sunflowers is described. The structure of a sunflower is quite different from that of a rice plant. For example, a sunflower doesn't have a cluster structure and has a flower at the developed stage. The simulated results from the structural model are validated by airborne Remote Sensing Campaign Mac-Europe 91, multi-frequency and multi-polarization data acquired for sunflower fields at the test site Montespertoli in Italy [5].

Another method to characterize the structure of vegetation is by applying growth rules. In Chapter 4, a growth rule based model is developed. It is especially useful to apply a growth rule based model to generate trees, which are structurally more complex. To fully capture the architecture of trees and describe their growth, the Lindenmayer systems (L-systems) are utilized. The L-systems approach was proposed by Lindenmayer for simulating the development and growth of living systems [44]. For simulation of trees, it places emphasis on the tree topology which specifies the neighboring relations between tree components. Trees generated by L-systems are quite realistic in appearance as compared to natural trees. With L-systems, trees at different growth stages can be simulated. Monte Carlo simulation results of the scattering returns from trees at different growth stages are shown and analyzed in this chapter. We will also examine the scattering returns from trees with different structures generated using L-systems. The concept of the "structure factor" which extracts the structural information of a tree and gives the spatial distribution of branches is defined. The structure factors are calculated and analyzed for trees with different architectures.

In Chapter 2, we consider a class of problems in which we know the physical characteristics of the scattering objects or medium, and wish to determine the scattering coefficients. In Chapter 5, a different class of problems is considered in which the scattering coefficients are known, and we wish to determine the characteristics of the scattering objects or medium from which the measurements are obtained. This problem is referred to as parameter inversion. In this chapter, the inversion of geophysical parameters is performed using neural networks. Neural networks have been studied for many years in the hope of simulating human intelligence. Because of its ability to learn, neural network can be trained to perform pattern recognition. It is flexible for the inversion of geophysical parameters especially for multi-dimensional inputs such as multi-frequency, multi-polarization scattering data. The applications of neural network to the inversion of soil moisture and surface parameters, the inversion of sunflower biomass, and the inversion of forest age (or equivalently, forest biomass) are described. For the inversion of soil moisture and surface parameters, neural networks are trained with theoretical surface scattering models. To retrieve the sunflower biomass, neural networks are trained with the developed vegetation scattering model described in Chapter 3 where the simulated results from the structural model are validated by airborne Remote Sensing Campaign Mac-Europe 91 multi-frequency and multi-polarization data. To examine the performance of the use of experimental data to train the neural networks, the polarimetric radar data acquired by the Spaceborne Imaging Radar-C (SIR-C) over the Landes Forest in France and the information on the forest age from the biomass map of that area are utilized as the training data to retrieve the forest age. The retrieval of forest age from remote sensing data is important in the studies of global change and has been a subject of great interest in recent years [6, 13, 40]. Different combinations of backscattering data are used as input to the neural net in order to determine the combination which gives the best inversion result.

In Chapter 6, the conclusions of this thesis research are presented.

Chapter 2

Monte Carlo Approach for Vegetation

2.1 Remote Sensing Models for Vegetation

In the past, the electromagnetic scattering from the vegetation canopy has been calculated using the radiative transfer theory and the analytic wave theory [69, 74]. The analytic wave theory starts from Maxwell's equations. To obtain solutions, approximations are made since the equations are in general complicated. The scattered field from the medium is calculated with the use of dyadic Green's functions together with approximations such as the Born approximation [29, 74, 91] or distorted Born approximation [37, 38, 58]. The Born approximation, which was named in honor of Max Born who developed the technique for quantum particle scattering, is the simplest and widely used method. In the Born technique, the basic assumption is that the internal field is not altered by the presence of the particle. In the integral form of the scattered field which is derived from the wave equation with the use of dyadic Green's functions, the internal field is identical to the incident wave inside the integral with this approximation. Although this technique is simple and can be applied without a priori knowledge of the field, it's only valid for weak permittivity fluctuations. The distorted Born approximation is an improvement over the Born approximation since it takes into account the attenuation of the incident and the scattered waves in the equivalent medium. In this technique, the scatterers are assumed to be embedded in the equivalent medium, and then a single scattering theory is employed to calculate the scattered field. This approximation is valid when the scattering albedo of each scatterer is small.

Unlike the analytic wave theory which starts with Maxwell's equations, the radiative transfer theory is based on the energy transport equation and describes the propagation of specific intensity in the scattering medium [73, 74]. The specific intensity is a four-element Stokes vector with the polarization of the electromagnetic radiation described by the four Stokes parameters. One of the assumptions in the radiative transfer theory is that particles scatter independently. Constituents of the radiative transfer equations are the phase matrix, extinction matrix, and emission vector. The phase matrix characterizes the coupling of electromagnetic intensities from other directions into the direction under consideration as the result of scattering. The extinction matrix describes the attenuation due to absorption and scattering loss. It can be evaluated by summing the absorption and scattering coefficients, or can be expressed in terms of the forward scattering functions using the optical theorem [74]. The emission vector provides the source of thermal emission. It is mainly used in the passive remote sensing cases. Different algorithms, such as the iterative approach and the discrete ordinate-eigenanalysis method, have been used to solve the radiative transfer equations. In the iterative approach, scattering is considered as a small perturbation. The solutions can be written as a perturbation series. Using the scattering parameter as the iterative parameter, each order in the series can be calculated by iteration of the previous order. The iterative approach is more applicable when the albedo is small such that the convergence of the solution can be reached quickly. For cases of general albedo, the discrete ordinate-eigenanalysis method can be used. With this method, the radiative transfer equations are solved numerically by discretizing the propagation directions into a finite number of directions in order to convert the differential-integral equation into a system of ordinary differential equations with constant coefficients. The solution can then be obtained by eigenanalysis.

To characterize the random media, both the continuous random medium model [9, 17, 18, 72] and the discrete scatterer model [37, 38] have been used in the above two approaches. The continuous random medium model uses a correlation function to describe the permittivity fluctuation of the medium of interest. The key inputs to the model include variances and correlation lengths, which correspond to the fluctuation strength and geometries of the scatterers, respectively. The effective permittivity is calculated by taking into consideration the attenuation and phase delay of wave propagation inside the medium. This method has been applied to calculate the polarimetric returns for vegetation with selected correlation function parameters [9]. In the discrete scatterer model, the inhomogeneities are considered as discrete scatterers embedded in a background medium. In addition to the background permittivity, the inputs to the model include the fractional volume, sizes, shapes, orientation distributions, and permittivities of the scatterers.

To simulate the electromagnetic scattering from the vegetation using either the analytic wave theory or the radiative transfer theory, the vegetation canopy has been modeled as a layer of randomly oriented leaves with disk shapes [38, 31, 66], or a layer of randomly oriented stems or leaves with cylindrical shapes [33, 39]. The forest has been modeled as a layer of nearly vertical cylinders representing tree trunks and a layer of randomly oriented cylinders representing branches [14]. However, in those models, the form or structure of vegetation has not been addressed. The effect of vegetation architecture on the scattering returns has been studied [90, 27] and was demonstrated to be significant. The results show that it is necessary for theoretical models to take into consideration the different vegetation architectures and growth patterns of trees. The structure of vegetation plays an important role in determining the observed coherent effects. Imhoff [27] did a systematic study on the effect of forest structure on the radar backscattering returns by simulating a series of forest stands having equivalent above ground biomass while allowing the structure to vary. The results indicate that the structure can have a substantial effect on the backscattering returns for forests with equal biomass. To take into account the architecture of vegetation, Yueh, *et al.*[90] developed a branching model for the remote sensing of vegetation with the wave approach. A two-scale branching model was presented for soybean plants with the internal structure and the resulting cluster effects considered. The branching model takes into account the phase interference between each component. However, the probability density functions and the pair-distribution functions required in their analytic formulation are usually difficult to obtain for natural vegetation.

Using Monte Carlo technique to solve Maxwell's equations for different applications becomes more practical in recent years with the rapid advances of computer technology. The Monte Carlo method is a numerical technique which solves mathematical problems by the simulation of random variables [20]. Because simulation of random variables is a laborious process, the use of the Monte Carlo method is becoming increasingly popular with the fast computational speed and memory capacity of the modern digital computer, especially the multiprocessor computing systems which can simulate many independent statistical experiments in parallel. In addition, because of the increasing complexity in mathematical modeling of the phenomena in question, classical computational methods are in many cases unsatisfactory. The Monte Carlo method has been used to solve a variety of problems which are beyond the available resources of theoretical mathematics. It has been applied in areas such as physics, chemistry, biology, medicine, economics, etc. [7, 48, 65, 70]. In the past, the results from the Monte Carlo approach were used to compare with experimental data from real systems in order to check how well the model approximates a real system. The Monte Carlo approach was also utilized to compare its results with analytic theories which start with the same model in order to determine the validity of some approximations made in the analytic calculation. In addition, Monte Carlo simulation can provide more insight into some complex problems which may not be obtained with other means. It has been applied to calculate the scattering returns from the rough surface [30, 50, 77], and from densely packed spheres [76, 93].

In this thesis research, a coherent scattering model with analytic wave theory is proposed based on Monte Carlo simulation for the microwave remote sensing of vegetation canopy. The statistical scattering properties of the canopy are obtained from the Monte Carlo simulation. Unlike the models using the radiative transfer approach which assumes particles scatter independently, this scattering model takes into account of the distinctive structures of vegetations, and especially the coherent wave interactions among vegetative elements which are usually in clusters and closely spaced. Compared to the branching model, this scattering model utilizing the Monte Carlo approach also has the advantage of eliminating the need for assuming the correlation information between the vegetative elements. With the information on the location and orientation of a vegetative element considered as the first order statistics, the correlation between the vegetative elements is considered as the higher order statistics and is very difficult to measure. Since the Monte Carlo approach implicitly generates the higher order statistics, it is not necessary to make the assumption on the probability density functions and the pair-distribution functions as required in the branching model. Besides its capability of taking the complex vegetation structures into account, this scattering model can also easily incorporate the growth rules of vegetation in the simulation.

2.2 Characterization of the Vegetation Structure

Since the vegetation structure can have a significant effect on the scattering returns, it is important to have a realistic description of the vegetation structure under consideration. In general, vegetation consists of structures of many length scales. Each type of vegetation has its own particular structure and form. Crops have simpler structures and fewer scales while trees have more scales and more complicated in forms. In our proposed coherent scattering model based on Monte Carlo approach, two methods to characterize the structure of vegetation are incorporated. The first method requires the specification of the number of each type of component and the relative orientations of the components. Another method uses growth rules. The structural model and growth rule based model which incorporate these two methods respectively are described below.

2.2.1 Structural Model

One method of characterizing the structure of vegetation is by specifying the number of components and how the components are oriented with respect to one another. In the past, vegetation has been modeled with simple structure such as same-size cylinders [39]. Other examples include a soybean plant modeled as a vertical branching plant having a stem and terminal branches with attached leaves [90], a grass canopy represented by elongated elliptical discs [64], and a pine tree modeled with multiple scale cylinders where very thin cylinders are used to represent the needles [3, 25]. In the structural model, vegetation structure is characterized by levels of details where the fine features of distinct vegetation structures can be preserved to the desired level of accuracy. The first level consists of stems and trunks. The next level includes the branches, with the specification of the number of branches grown from a single stem or trunk, their orientation angles and branching angles. The third level includes leaves in the vegetation structure. At this level, the number of leaves grown from each terminal branch or stem, the orientations of the leaves and their connections to the terminal branches or stems provide a more detailed description of the vegetation structure. At later growth stages, some vegetations have flowers. Therefore, the next level incorporates flowers grown from stems or terminal branches.

2.2.2 Growth Rule Based Model

Another method of defining the structure of vegetation utilizes growth rules. In the past, fractals have been used to simulate trees [4, 47, 51]. In his book, Benoit Mandelbrot used the "pipe model" to simulate trees, in which the trees are described as bundles of non-branching vessels of fixed diameters, connecting roots to leaves [47]. The basic idea behind fractal geometry is self-similarity, which can be observed in certain aspects of plant structures. Some of the trees generated are quite realistic because some of the plant developmental processes result in self-similarity. To fully capture and describe plant development in time, the formalism of Lindenmayer systems, or L-systems, has been utilized [52, 53, 54, 55, 68]. The L-systems technique was proposed by Lindenmayer for simulating the development and growth of living systems [44]. The central concept of L-systems is that of rewriting, which is a technique for defining complex objects by successively replacing parts of a simple initial object using a set of rewriting or production rules. It is especially useful in generating structurally complex trees. Trees generated by Lindenmayer systems are quite realistic in appearance compared to natural trees.

2.3 Monte Carlo Approach

In this section, the developed coherent scattering model based on Monte Carlo simulation is described. This model takes into account the coherent wave interactions among vegetative elements which are usually closely spaced and in clusters. In the Monte Carlo simulation approach, the first step is to create simulated scenarios for the vegetation canopy of interest. The configurations are created by computer experiments on the basis of the ground truth characterizations such as the fractional volumes, sizes, and shapes of stems and leaves, or some growth rules which are applied to the Lindenmayer systems. Therefore, the location, orientation, and distribution of every vegetation component can be obtained from computer simulations. Given a created realization, the scattering can be calculated by solving Maxwell's equations.

Consider a configuration of a vegetation field where the top of the vegetation canopy is indicated by $z = 0$ and the boundary between the vegetation canopy and the ground is $z = -h$. Given the configuration of the vegetation field and an incident wave $\bar{E}^i$ in the direction (θ_i, ϕ_i), the first-order solution of the backscattered electric field can be expressed as the sum of four terms which describes the four major scattering mechanisms in a vegetation canopy (Figure 2-1).

$$E_q^s(\overline{r}) = \frac{e^{ikr}}{r}\left(S_1 + S_2 + S_3 + S_4\right) E_p^i \tag{2.1}$$

where q and p are the polarization components (q, p $=$ h or v) of the scattered and incident waves, respectively.

S_1 describes the the direct scattering from a particle (Figure 2-1a) and can be expressed as

$$S_1 = \sum_{\substack{t=\text{stem,branch,}\\ \text{leaf, or flower}}} \sum_{j=1}^{N_t} f_{qp}^t(\pi - \theta_i, \pi + \phi_i; \theta_i, \phi_i) e^{i[\overline{k}_p^i(\theta_i,\phi_i) - \overline{k}_q^s(\pi-\theta_i,\pi+\phi_i)]\cdot\overline{r}_j^t} \tag{2.2}$$

where t is the index for the scatterer type—stem, branch, leaf, or flower, and N_t is the number of scatterers. f_{qp}^t is the scattering matrix element. $\overline{k}_p^i$ is the propagation vector of the incident wave, $\overline{k}_q^s$ is the propagation vector of the backscattered field. θ_i is the incident angle from the vertical direction and ϕ_i is the azimuthal angle. $\overline{r}_j^t = \hat{x}x_j^t + \hat{y}y_j^t - \hat{z}z_j^t$ is the location of the element j of scatterer type t.

The second term S_2 is a single scattering from the scatterer followed by a reflection off the boundary (Figure 2-1b).

$$S_2 = \sum_{\substack{t=\text{stem,branch,}\\ \text{leaf, or flower}}} \sum_{j=1}^{N_t} R_q(\theta_i) f_{qp}^t(\theta_i, \pi + \phi_i; \theta_i, \phi_i) e^{i[\overline{k}_p^i(\theta_i,\phi_i) - \overline{k}_q^s(\theta_i,\pi+\phi_i)]\cdot\overline{r}_j^t} \tag{2.3}$$

The third term is the reverse of the second term; *i.e.*, it represents surface scattering followed by single scattering (Figure 2-1c).

$$S_3 = \sum_{\substack{t=\text{stem,branch,}\\ \text{leaf, or flower}}} \sum_{j=1}^{N_t} f_{qp}^t(\pi - \theta_i, \pi + \phi_i; \pi - \theta_i, \phi_i) R_p(\theta_i) e^{i[\overline{k}_p^i(\pi-\theta_i,\phi_i) - \overline{k}_q^s(\pi-\theta_i,\pi+\phi_i)]\cdot\overline{r}_j^t} \tag{2.4}$$

$R_p(\theta_i)$ and $R_q(\theta_i)$ are the Fresnel reflection coefficients. Since the permeability for the ground and the region above the ground is assumed to be equal to the free space permeability, the Fresnel reflection coefficients for the horizontally and vertically polarized waves are

$$\begin{aligned} R_h &= \frac{k_0 \cos\theta_i - k_1 \cos\theta_i}{k_0 \cos\theta_i + k_1 \cos\theta_i} \\ R_v &= \frac{\epsilon_1 k_0 \cos\theta_i - k_1 \cos\theta_i}{\epsilon_1 k_0 \cos\theta_i + k_1 \cos\theta_i} \end{aligned} \tag{2.5}$$

where k_0 is the free space wavenumber, and k_1 is the wavenumber of the ground with dielectric constant ϵ_1.

The fourth term S_4 describes a reflection by the boundary followed by a single scattering from the particle and further followed by a reflection off the boundary (Figure 2-1d).

$$S_4 = \sum_{\substack{t=\text{stem,branch,} \\ \text{leaf, or flower}}} \sum_{j=1}^{N_t} R_q(\theta_i) f_{qp}^t(\theta_i, \pi+\phi_i; \pi-\theta_i, \phi_i) R_p(\theta_i) e^{i[\overline{k}_p^i(\pi-\theta_i,\phi_i)-\overline{k}_q^s(\theta_i,\pi+\phi_i)]\cdot\overline{r}_j^t} \tag{2.6}$$

For stems and branches, the scattering is calculated using the finite cylinder approximation [32] in which the induced current in the dielectric cylinder is assumed to be the same as that of the infinitely long cylinder of the same radius. It is a fairly good approximation for a circular dielectric cylinder with length longer than the wavelength of incident wave and radius much smaller than the wavelength of incident wave. The scattered field is approximated by evaluating the field radiated from this induced current source.

The scattering matrix elements of a finite cylinder with dielectric constant ϵ_s, permeability equal to that of free space, radius a and length l are given by

$$
\begin{aligned}
f_{hh}^{t} &= \frac{k_0^2(\epsilon_s - 1)u}{2}\left\{-B_0\eta h_{0h} + 2\sum_{n=1}^{\infty}(iA_n\cos\theta_i e_{nh} - B_n\eta h_{nh})\cos[n(\phi_s - \phi_i)]\right\} \\
f_{vv}^{t} &= \frac{k_0^2(\epsilon_s - 1)u}{2}\left\{ e_{0v}(B_0\cos\theta_i\cos\theta_s + Z_0\sin\theta_s)\right. \\
&\quad \left. +2\sum_{n=1}^{\infty}[(B_n\cos\theta_i e_{nv} + iA_n\eta h_{nv})\cos\theta_s + e_{nv}Z_n\sin\theta_s]\cos[n(\phi_s - \phi_i)]\right\} \\
f_{hv}^{t} &= \frac{k_0^2(\epsilon_s - 1)u}{2}\,2i\sum_{n=1}^{\infty}(iA_n\cos\theta_i e_{nv} - B_n\eta h_{nv})\sin[n(\phi_s - \phi_i)] \\
f_{vh}^{t} &= \frac{k_0^2(\epsilon_s - 1)u}{2}\,2i\sum_{n=1}^{\infty}[(B_n\cos\theta_i e_{nh} + iA_n\eta h_{nh})\cos\theta_s + e_{nh}Z_n\sin\theta_s]\sin[n(\phi_s - \phi_i)]
\end{aligned}
\tag{2.7}
$$

where

$$
u = \frac{e^{i(k_{zi} - k_{zs})l} - 1}{i(k_{zi} - k_{zs})} \tag{2.8}
$$

k_{zi} and k_{zs} are the $\hat{z}$-components of the incident and scattered wave vectors, respectively. Z_n, A_n and B_n in Equation 2.7 are as follows.

$$
\begin{aligned}
Z_n &= \frac{a}{k_{1\rho i}^2 - k_{\rho s}^2}[k_{1\rho i}J_n(k_{\rho s}a)J_{n+1}(k_{1\rho i}a) - k_{\rho s}J_n(k_{1\rho i}a)J_{n+1}(k_{\rho s}a)] \\
A_n &= \frac{k_0}{2k_{1\rho i}}(Z_{n-1} - Z_{n+1}) \\
B_n &= \frac{k_0}{2k_{1\rho i}}(Z_{n-1} + Z_{n+1})
\end{aligned}
\tag{2.9}
$$

The coefficients e_{nh}, e_{nv}, h_{nh} and h_{nv} are given by the following equations

$$
\begin{aligned}
e_{nh} &= \left(\frac{k_{\rho i}}{k_0}\right)\frac{1}{R_nJ_n(k_{1\rho i}a)}\left[\frac{1}{(k_{\rho i}a)^2} - \frac{1}{(k_{1\rho i}a)^2}\right]\frac{k_{zi}}{k_0}n \\
\eta h_{nh} &= -i\left(\frac{k_{\rho i}}{k_0}\right)\frac{1}{R_nJ_n(k_{1\rho i}a)}\left[\frac{\epsilon_s J_n'(k_{1\rho i}a)}{k_{1\rho i}aJ_n(k_{1\rho i}a)} - \frac{H_n^{(1)\prime}(k_{\rho i}a)}{k_{\rho i}aH_n^{(1)}(k_{\rho i}a)}\right]
\end{aligned}
$$

$$\begin{aligned} e_{nv} &= i\left(\frac{k_{\rho i}}{k_0}\right)\frac{1}{R_n J_n(k_{1\rho i}a)}\left[\frac{J_n'(k_{1\rho i}a)}{k_{1\rho i}aJ_n(k_{1\rho i}a)}-\frac{H_n^{(1)'}(k_{\rho i}a)}{k_{\rho i}aH_n^{(1)}(k_{\rho i}a)}\right] \\ \eta h_{nv} &= e_{nh} \end{aligned} \tag{2.10}$$

where

$$\begin{aligned} R_n = \frac{\pi(k_{\rho i}a)^2H_n^{(1)}(k_{\rho i}a)}{2}&\left\{\left(\frac{k_{zi}}{k_0}\right)^2\left(\frac{1}{(k_{\rho i}a)^2}-\frac{1}{(k_{1\rho i}a)^2}\right)^2 n^2\right. \\ &\left.-\left[\frac{\epsilon_s J_n'(k_{1\rho i}a)}{k_{1\rho i}aJ_n(k_{1\rho i}a)}-\frac{H_n^{(1)'}(k_{\rho i}a)}{k_{\rho i}aH_n^{(1)}(k_{\rho i}a)}\right]\left[\frac{J_n'(k_{1\rho i}a)}{k_{1\rho i}aJ_n(k_{1\rho i}a)}-\frac{H_n^{(1)'}(k_{\rho i}a)}{k_{\rho i}aH_n^{(1)}(k_{\rho i}a)}\right]\right\} \end{aligned}$$

and

$$\begin{aligned} k_{1\rho i} &= \sqrt{k_0^2\epsilon_s - k_{zi}^2} \\ k_{\rho i} &= \sqrt{k_0^2 - k_{zi}^2} \end{aligned} \tag{2.11}$$

k_0 is the free space wavenumber. J_n and $H_n^{(1)}$ are the Bessel function and the Hankel function of the first kind, respectively.

For scattering from leaves or flowers, the returns are calculated using the physical optics approximation for elliptic discs [43], which assumes the internal field inside the disc to be the same as that of the infinitely extended dielectric layer of the same thickness. For a thin circular disk with dielectric constant ϵ_ℓ and free space permeability, the scattering matrix elements are as follows.

$$\begin{aligned} f_{hh}^t &= \frac{k_0^2}{4\pi}(\epsilon_\ell - 1)\cos(\phi_s-\phi_i)\frac{d}{2}V\left[A_{1h}\mathrm{sinc}((k_{1zi}-k_{zs})\frac{d}{2}) + B_{1h}\mathrm{sinc}((k_{1zi}+k_{zs})\frac{d}{2})\right] \\ f_{vv}^t &= \frac{k_0^2}{4\pi}(\epsilon_\ell - 1)\frac{k_0}{k_1^2}\frac{d}{2}V \\ &\left[(k_{1zi}\cos\theta_s\cos(\phi_s-\phi_i) + k_0\sin\theta_i\sin\theta_s)A_{1v}\mathrm{sinc}((k_{1zi}-k_{zs})\frac{d}{2})\right. \end{aligned}$$

$$
\begin{aligned}
&\quad +(-k_{1zi}\cos\theta_s\cos(\phi_s-\phi_i)+k_0\sin\theta_i\sin\theta_s)B_{1v}\mathrm{sinc}((k_{1zi}+k_{zs})\frac{d}{2})\Big] \\
f^t_{hv} &= \frac{k_0^2}{4\pi}(\epsilon_\ell-1)\frac{k_0}{k_1^2}k_{1zi}\sin(\phi_s-\phi_i)\frac{d}{2}V \\
&\quad \left[-A_{1v}\mathrm{sinc}((k_{1zi}-k_{zs})\frac{d}{2})+B_{1v}\mathrm{sinc}((k_{1zi}+k_{zs})\frac{d}{2})\right] \\
f^t_{vh} &= \frac{k_0^2}{4\pi}(\epsilon_\ell-1)\cos\theta_s\sin(\phi_s-\phi_i) \\
&\quad \left[A_{1h}\mathrm{sinc}((k_{1zi}-k_{zs})\frac{d}{2})+B_{1h}\mathrm{sinc}((k_{1zi}+k_{zs})\frac{d}{2})\right]
\end{aligned}
\tag{2.12}
$$

where

$$k_{1zi}=\sqrt{k_0^2\epsilon_\ell-k_{xi}^2-k_{yi}^2} \tag{2.13}$$

k_{xi}, k_{yi} and k_{zi} are the $\hat{x}$-, $\hat{y}$- and $\hat{z}$-components of the incident wave vector, respectively. A_{1h} and B_{1h} are the amplitudes of upgoing and downgoing horizontally polarized incident waves in the disk and have the following expressions.

$$A_{1h} = \frac{2e^{i(-k_{zi}+k_{1zi})\frac{d}{2}}(\rho_{01}-1)}{(1+\rho_{01h})^2e^{-ik_{1zi}d}-(1-\rho_{01})^2e^{ik_{1zi}d}} \tag{2.14}$$

$$B_{1h} = \frac{2e^{-i(k_{zi}+k_{1zi})\frac{d}{2}}(\rho_{01}+1)}{(1+\rho_{01h})^2e^{-ik_{1zi}d}-(1-\rho_{01})^2e^{ik_{1zi}d}} \tag{2.15}$$

where $\rho_{01h}=k_{1zi}/k_{zi}$. A_{1v} and B_{1v} are the amplitudes of upgoing and downgoing vertically polarized incident waves in the disk and can be obtained by substituting $\rho_{01v}=k_{1zi}/\epsilon_\ell k_{zi}$ for ρ_{01h} in Equations 2.14 and 2.15. For a circular disk,

$$V=\pi a^2\frac{2J_1(|\bar{k}_{\rho i}-\bar{k}_{\rho s}|a)}{|\bar{k}_{\rho i}-\bar{k}_{\rho s}|a} \tag{2.16}$$

where

$$
\begin{aligned}
\bar{k}_{\rho i} &= \hat{x}k_{xi}+\hat{y}k_{yi} \\
\bar{k}_{\rho s} &= \hat{x}k_{xs}+\hat{y}k_{ys}
\end{aligned}
\tag{2.17}
$$

k_{xs}, k_{ys} and k_{zs} are the $\hat{x}$-, $\hat{y}$- and $\hat{z}$-components of the scattered wave vector, respectively.

The effects of attenuation on the coherent wave caused by the inhomogeneities are also taken into account using Foldy's approximation [74, 90]. The attenuation is obtained by averaging the forward scattering returns of each scattering component. The canopy components are assumed to be excited by this coherent wave. The coherent wave along the propagation direction (θ, ϕ) is governed by

$$\frac{dE_h}{ds} = (ik_0 + M_{hh})E_h + M_{hv}E_v \tag{2.18}$$

$$\frac{dE_v}{ds} = M_{vh}E_h + (ik_0 + M_{vv})E_v \tag{2.19}$$

where E_h and E_v are the horizontally and vertically polarized components of the electric field, and s is the distance along the propagation direction. In equations 2.18 and 2.19,

$$M_{qp} = \frac{i2\pi}{k_0 Ah} \sum_{\substack{t=\text{stem,branch,}\\ \text{leaf, or flower}}} N_t < f^t_{qp}(\theta, \phi; \theta, \phi) > \tag{2.20}$$

where q and p are again the polarization components (q, $p = h$ or v). The angular brackets denote the configurational average, h is the height of the vegetation canopy, A is the area of the vegetation field, and k_0 is the wavenumber of free space. The horizontally and vertically polarized waves propagate along the direction (θ, ϕ) inside the vegetation canopy with the propagation constants

$$k_h = k_0 - iM_{hh} \tag{2.21}$$

$$k_v = k_0 - iM_{vv} \tag{2.22}$$

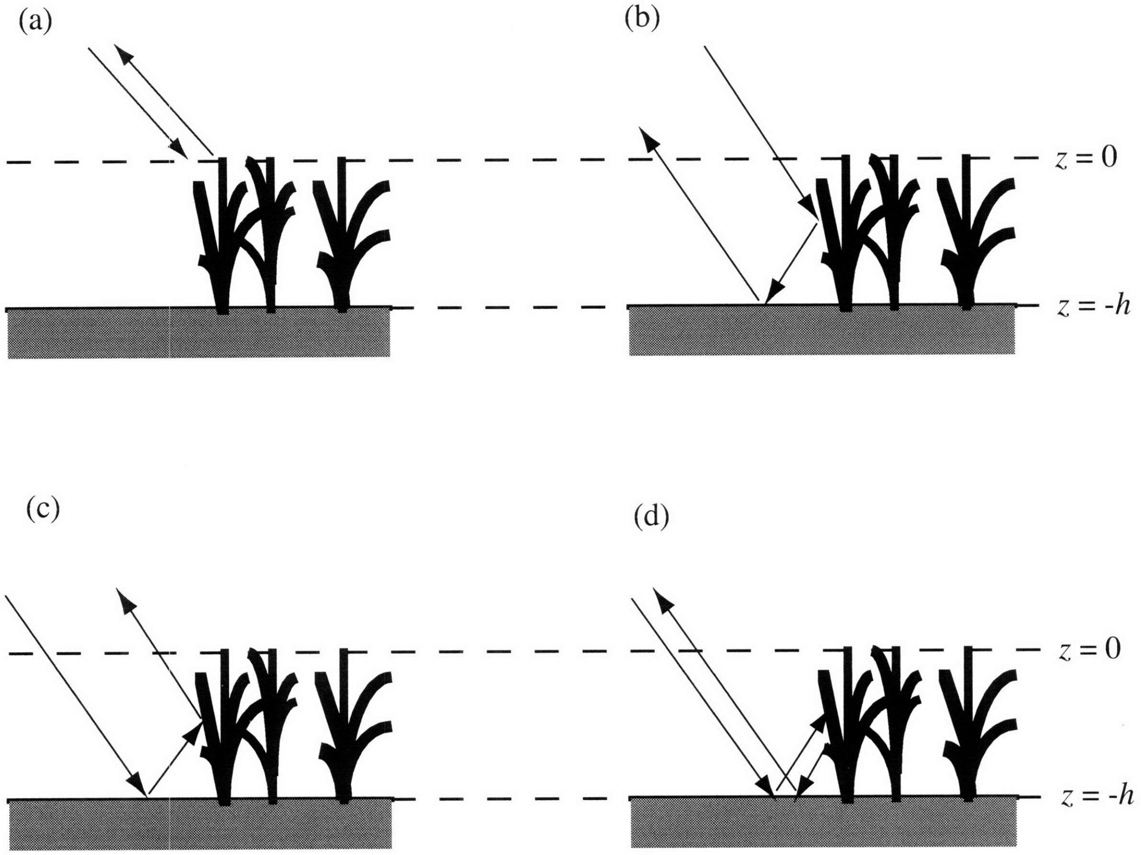

Figure 2-1: Four major scattering mechanisms: (a) direct scattering from scatterers, (b) single scattering from a scatterer followed by reflection off the boundary, (c) surface scattering followed by single scattering, (d) reflection by the boundary followed by single scattering from a scatterer and further followed by reflection off the boundary.

for horizontally and vertically polarized components, respectively. Since the calculated k_h and k_v are quite close to k_0, the effects of reflection and refraction at the top boundary of the vegetation canopy layer are neglected here. On the basis of equations 2.21 and 2.22, equation 2.1 can be expressed as

$$\begin{aligned} E_q^s(\bar{r}) &= \frac{e^{ikr}}{r} \sum_{\substack{t=\text{stem,branch,}\\ \text{leaf, or flower}}} \sum_{j=1}^{N_t} \Bigg[f_{qp}^t(\pi-\theta_i, \pi+\phi_i; \theta_i, \phi_i) e^{-M_{qq}\frac{z_j^t}{\cos\theta_i}} e^{-M_{pp}\frac{z_j^t}{\cos\theta_i}} e^{2i(k_x^i x_j^t + k_y^i y_j^t - k_z^i z_j^t)} \\ &+ R_q(\theta_i) f_{qp}^t(\theta_i, \pi+\phi_i; \theta_i, \phi_i) e^{M_{qq}\frac{2h+z_j^t}{\cos\theta_i}} e^{-M_{pp}\frac{z_j^t}{\cos\theta_i}} e^{2i(k_x^i x_j^t + k_y^i y_j^t + k_z^i h)} \\ &+ f_{qp}^t(\pi-\theta_i, \pi+\phi_i; \pi-\theta_i, \phi_i) R_p(\theta_i) e^{-M_{qq}\frac{z_j^t}{\cos\theta_i}} e^{M_{pp}\frac{2h+z_j^t}{\cos\theta_i}} e^{2i(k_x^i x_j^t + k_y^i y_j^t + k_z^i h)} \\ &+ R_q(\theta_i) f_{qp}^t(\theta_i, \pi+\phi_i; \pi-\theta_i, \phi_i) R_p(\theta_i) \\ &\quad e^{M_{qq}\frac{2h+z_j^t}{\cos\theta_i}} e^{M_{pp}\frac{2h+z_j^t}{\cos\theta_i}} e^{2i(k_x^i x_j^t + k_y^i y_j^t + k_z^i(2h+z_j^t))} \Bigg] E_p^i \end{aligned} \tag{2.23}$$

where $k_x^i = k_0 \sin\theta_i \cos\phi_i$, $k_y^i = k_0 \sin\theta_i \sin\phi_i$, and $k_z^i = k_0 \cos\theta_i$. The attenuation is from the real part of M_{pp} and M_{qq}. The coherent addition method is adopted in which the total scattered field from the canopy is obtained by adding the scattered field from each component coherently.

The scattered electric field E_q^s from each realization is calculated according to equation 2.23. The backscattering coefficient is then computed from

$$\sigma_{qp} = \frac{4\pi r^2}{A} \frac{< |E_q^s|^2 >}{|E_p^i|^2} \tag{2.24}$$

where A is the illuminated area. The results are obtained by averaging over an ensemble of realizations. The convergence of the Monte Carlo simulation is checked numerically with respect to the number of scatterers and realizations.

2.4 Summary

In this chapter, a coherent scattering model is developed based on Monte Carlo simulation for the microwave remote sensing of vegetation canopy. The Monte Carlo approach is capable of taking the complex vegetation structures into account. It has the advantage over the conventional wave theory because it is not necessary to find the probability density functions and the pair-distribution functions, which are required in the analytic formulation and are usually difficult to obtain for natural vegetation. This model takes into consideration the coherent wave interactions among vegetative elements which are usually closely spaced and in clusters. Four major scattering mechanisms in a vegetation canopy are considered, including the direct scattering from a vegetation component, and three types of volume-surface interactions. The effects of attenuation caused by inhomogeneities on the coherent wave are incorporated in the model using Foldy's approximation, in which the attenuation is obtained by averaging the forward scattering returns of each scattering component. The scattering from stems and branches is calculated using the finite cylinder approximation, while scattering from leaves or flowers is calculated using the physical optics approximation for elliptical discs.

To take advantage of the Monte Carlo approach, a realistic description of the vegetation structure under consideration is needed. Two methods to characterize the structure of vegetation are introduced in this chapter. One method requires the specification of the number of each type of component and the relative orientations of the components. A structural model which incorporates this method is described in more detail in Chapter 3. Another method to characterize the structure of vegetation uses growth rules. A more detailed description of a growth rule based model is presented in Chapter 4.

Chapter 3

Structural Model

3.1 Structure of Vegetation

To calculate scattering from vegetation, it is important to be able to model the vegetation structure as accurately as possible especially for vegetations with their clustered and closely spaced elements. One method to characterize the structure of vegetation is by specifying the number of each type of component and the relative orientations of the components.

In the structural model, vegetation structure is characterized by levels of detail. The detailed features of distinct vegetation structures can be preserved to the desired level of accuracy. The first level consists of the primary components of the vegetation structure, such as stems or trunks. They are in general the major scatterers. The second level considers the branches. The orientation angles, branching angles, and the number of branches contribute toward forming the distinct structure of vegetation.

For vegetation with leaves, the next level includes the leaves in the model. A more detailed description of the structure is achieved by specifying the number of leaves and how the leaves are oriented and connected to the branches and stems. Although in general the leaves may not have a large contribution to the scattering, the attenuation caused by leaves at high frequencies cannot be ignored. Since some vegetations have flowers at later growth stages, the next level consists of flowers grown from stems or terminal branches.

In the Monte Carlo simulation, the configurations are generated from the characterization of vegetation structure. Based on the ground truth measurements, the distinct structures for different vegetations can be specified by the types of components, the number and size of each type of component, and the orientation and branching angles of the components. In this chapter, the applications of the structural model to two types of vegetation are described. One is the rice crop, which is an essential food source in many regions of the world such as Asia and forms the basis of the economy in many countries. Since rice plants usually occur in clusters and are closely spaced, a good structural model which takes into account the coherent wave interaction is essential. In addition to the rice canopy, the application of the structural model to sunflowers will also be discussed in this chapter.

3.2 Application to Rice Fields

3.2.1 Introduction

Rice is an essential food source in many regions of the world such as Asia. It forms the basis of the economy in many countries. As a consequence, rice monitoring is economically useful in predicting the yield of rice crops. In addition, rice monitoring is important environmentally. The knowledge of rice growing areas can be used to estimate the flux of methane from the irrigated rice fields to the atmosphere [28]. Methane is second in importance only to carbon dioxide as a greenhouse gas. Flooding a rice field cuts off the oxygen supply from the atmosphere to the soil; methane is the major product in the process.

In recent years, satellite remote sensing has played an important role in most crop monitoring programs. Investigations have been carried out using X-band airborne synthetic aperture radar (SAR) [39]. There have also been some pilot studies that use European Satellite ERS-1 Synthetic Aperture Radar (SAR) data to estimate rice crop acreage and growth at several places in the world such as Japan [35, 36], Thailand [2], and Indonesia [41]. Temporal variations of the radar backscattering coefficients observed by ERS-1 at several test-sites were analyzed to derive a general trend for the response of electromagnetic sensors in a whole growth cycle of rice [41]. It shows a large increase in radar backscatter when the rice plants grow from 0 to 100 days. This large increase can be explained by the increase in biomass and the fact that rice fields have flooded ground surfaces during a large portion of the growing period. Therefore, the increase is enhanced by this highly reflective underlying flooded surface through the volume-surface interaction. Investigations on the use of satellite data for rice monitoring have also been carried out using the Japanese Earth Satellite-1 (JERS-1) data with the operating frequency at L-band. Rosenqvist, *et al.* [61] pointed out that there is a significant difference in the backscattering results from the rice fields in Niigata, Japan, depending on the planting directions of the rice plants. However, this phenomenon was not observed in the backscattering returns from the rice fields in Malaysia as the result of different planting practices between the two countries. Therefore, the structure of the rice fields, that is, how the rice plants are planted in the field, can have an important effect on the scattering returns. There were also studies that use the multiple temporal RADARSAT images to monitor the rice growth status [67]. From the RADARSAT data, we recently obtained the rice field scattering returns at two looking angles. To interpret those experimental observations such as the effects of the structure of rice fields, and to predict the temporal response of rice growth, we utilize the structural model which takes into account the distinctive structure of rice plants and the coherent wave interactions among plant elements which are in clusters.

In Section 3.2.2, the structure of rice plants and how the rice plants are planted in the rice field are described. Given the configuration of the rice field, the backscattered electric field is then calculated using the developed scattering model based on Monte Carlo approach described in Chapter 2. In Section 3.2.3, simulation results are compared with ERS-1 data [41] which has VV polarization and RADARSAT data

[57] which has HH polarization. The model is then applied to investigate the effects of the structure of rice field on scattering returns in Section 3.2.4. Backscattering results are shown for both L- and C-band frequencies. The ratio of HH over VV versus the age of rice canopy for different cases of rice field structures is also given to show the possibility of using HH/VV to eliminate ambiguities for the inversion problem at L-band.

3.2.2 Structure of Rice Plants

In a previous modeling study [39], rice plants were modeled as thin dielectric cylinders over a rough underlying surface, and the backscattering coefficients were obtained using the first-order solution of the radiative transfer theory. However, it is important to take into account the coherent wave interactions among vegetative elements of the rice canopy which usually occur in clusters and are closely spaced.

In the model, rice plants are planted with spacing a in the x-direction and spacing b in the y-direction over a square area A (Figure 3-1). Small random variations in the spacing between rice plants are also considered. Each rice plant contains a bunch of N_s vertical dielectric cylindrical stems with height H, radius c, and complex dielectric constant ϵ_s. Each rice stem has N_ℓ leaves of elliptical disc shape with length ℓ, width w, thickness d, and complex dielectric constant ϵ_ℓ. The orientation of leaves is characterized by three Euler angles α, β, and γ. Within a rice bunch, the stems are randomly placed inside a circle of radius c_b with uniform distribution [78]. There are N_c bunches such that the total number of stems in the rice canopy is $N_c \times N_s$, and

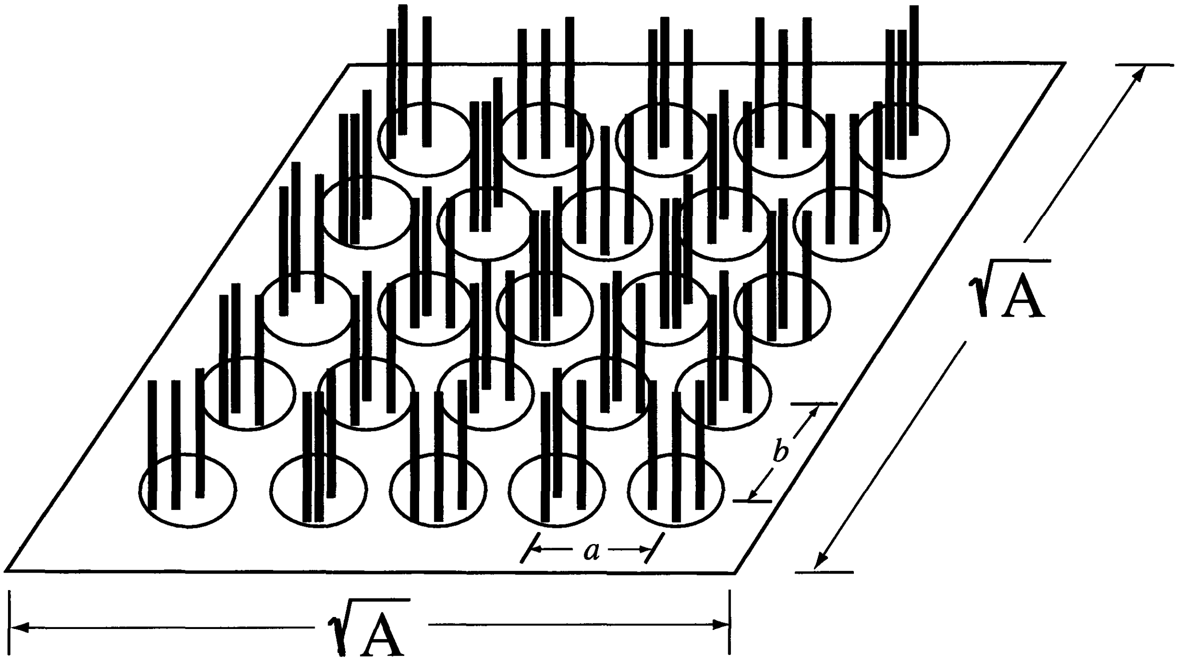

Figure 3-1: Configuration of a rice field for the scattering model. Rice plants are planted with spacing a in the x-direction and spacing b in the y-direction over a square area A. Within a rice bunch, the stems are randomly placed inside a circle with uniform distribution.

the total number of leaves is $N_c \times N_s \times N_\ell$. The height of the stems are also generated randomly with Gaussian distribution given the mean and the standard deviation of the height. The lower half space is water, with complex dielectric constant ϵ_1.

Consider a configuration of a rice field where the top of the rice field is indicated by $z = 0$ and the boundary between the rice canopy and the ground (water in our case) is $z = -h$. Given the configuration of the rice field and an incident wave $\bar{E}_i$ in the direction (θ_i, ϕ_i), the first-order solution of the backscattered electric field which is described in equation 2.23 consists of the summation of two types of scatterers: stems and leaves. In the equation, $N_t = N_c \times N_s$ for stems, and $N_c \times N_s \times N_\ell$ for leaves. For the rice field, equation 2.20 becomes

$$M_{qp} = \frac{i2\pi}{k_0} \frac{N_c N_s}{Ah} \left(< f_{qp}^{\text{stem}}(\theta, \phi; \theta, \phi) > + N_\ell < f_{qp}^{\text{leaf}}(\theta, \phi; \theta, \phi) > \right) \tag{3.1}$$

Since the bottom of rice plants is immersed in water, the contribution to the scattering from the second, third and fourth scattering mechanisms described in Chapter 2 is very large compared to other types of vegetation. The backscatter from the rice canopy is calculated with Monte Carlo simulations. In each realization of the rice field, the center positions of N_c rice clusters are first created and then the positions of the N_s stems within every bunch are generated using a random number generator with a uniform distribution. The positions of rice stems are checked so that there is no overlap between stems. The positions and orientations of the attached leaves on each stem are also generated randomly.

3.2.3 Comparison with Experimental Data

To validate the model, the simulated backscattering results at different growth stages are compared with the ERS-1 data [41]. The operating frequency is at C-band (5.3 GHz), and the angle is 23 degrees. There is only one polarization, VV. The data were obtained from Semarang and Akita test sites in Indonesia. The parameters used in the simulation are determined either directly from the measurements obtained during the experiment or from the existing literature (mainly from IRRI [28]).

The parameters used in the simulation of backscattering coefficients of rice fields are summarized in Table 3.1. The values for the height, gravimetric water content, leaf width, and leaf length of a rice plant are the mean values of experimental data. The stem radius, number of stems per bunch, number of bunches per unit area, and number of leaves per stem are derived from measurements, or completed with data from the literature [12]. The leaf thickness and the tilt angles for stems and leaves are estimated from another study [26]. The dielectric constants of rice plants at various growth stages are calculated from the gravimetric water content with an empirical formula by Ulaby, etal [82]. The formula for the dielectric constant of vegetation (ϵ_v) is a function of gravimetric water content M_g and frequency f.

$$\epsilon_v = \epsilon_r + v_{fw}[4.9 + \frac{75.0}{1 + if/18} - i\frac{22.86}{f}] + v_b[2.9 + \frac{55.0}{1 + (if/0.18)^{0.5}}] \tag{3.2}$$

where

$$\epsilon_r = 1.7 - 0.74M_g + 6.16M_g^2 \tag{3.3}$$

$$v_{fw} = M_g(0.55M_g - 0.076) \tag{3.4}$$

$$v_b = 4.64M_g^2/(1 + 7.36M_g^2) \tag{3.5}$$

v_{fw} and v_b are the volume fraction of free water and the bulk vegetation-bound water mixture respectively. Equation 3.2 consists of three terms which include a nondispersive residual component ϵ_r, a free water component, and a bulk vegetation-bound component. Since the bottom portion of the rice plants is in the water, the dielectric constant of the surface is that of water at the frequency of 5.3 GHz at 20°, which is $\epsilon_1 = 74 + i21$ [81]. In the simulation, the average spacing between two rice bunches is about 22 cm. We also assume that the height of a stem has a normal distribution with the standard deviation of 1 cm. The backscattering coefficients are obtained from the averaged scattered field of the rice field using equation 2.24. The scattered field is averaged over 50 realizations until it is converged.

In Figure 3-2, the model backscattering results of VV polarization at different growth stages are compared with the ERS-1 data [41]. The comparison shows good agreements between the simulation results and experimental data. The increasing trend of the temporal radar response is well described by the modeling results. The backscattering returns are mainly from the volume-surface interactions. Since the bottom portion of rice plants is immersed in water, the contribution of the second, third and fourth scattering mechanisms described in Chapter 2 to the total scattering from the rice canopy is very large compared to the case of other vegetation fields.

The simulated backscattering results at different growth stages are also compared with the RADARSAT data [57]. The operating frequency is at C-band (5.3 GHz), and there is only one polarization, HH. Data were obtained at two incident angles,

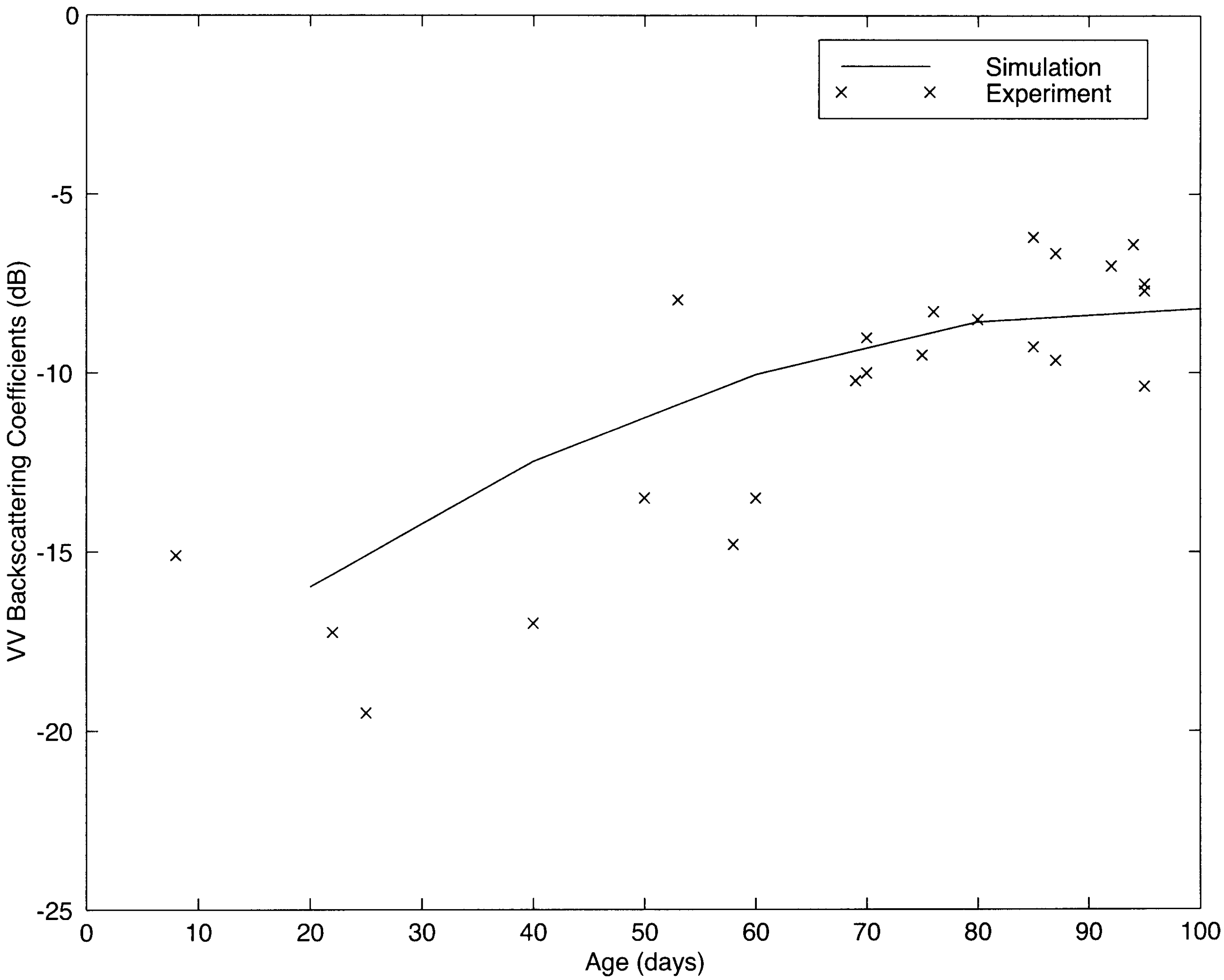

Figure 3-2: Comparison between the simulated VV backscattering coefficients and ERS-1 data [41] as a function of rice age. The operating frequency is at C-band.

age (days)	20	40	60	80	100
height H (cm)	20.0	35.0	50.0	68.4	76.7
stem radius c (cm)	0.1	0.12	0.14	0.16	0.18
# stems per bunch N_s	10	10	10	10	10
# bunches N_c/A (m^{-2})	20	20	20	20	20
gravimetric water content	0.7	0.72	0.74	0.71	0.71
dielectric constant ϵ_s, ϵ_ℓ	25.1+i7.9	26.3+i8.2	27.6+i8.6	25.7+i8.0	25.7+i8.0
leaf width w (cm)	0.41	0.74	0.98	1.15	1.24
leaf length ℓ (cm)	14.08	24.72	31.92	35.68	36
leaf thickness d (cm)	0.02	0.02	0.02	0.02	0.02
# leaves per stem N_ℓ	5	7	7	7	7
fractional volume (%)	0.06	0.09	0.123	0.161	0.204
stem max tilt angle θ_{ms} (deg)	0	0	0	5	10
leaf max tilt angle $\theta_{m\ell}$ (deg)	5	10	20	30	40

Table 3.1: Input parameters for the simulation of backscattering coefficients of a rice field for comparison with ERS-1 data [41]. The parameters used in the simulation are determined either directly from the measurements obtained during the experiment or from the existing literature (mainly from IRRI [28]).

23 and 43 degrees. The parameters used in the simulation are determined either directly from the measurements obtained during the experiment or from the existing literature (mainly from IRRI [28]). The parameters used in the simulation of backscattering coefficients of rice fields are summarized in Table 3.2. Using equation 3.2, the dielectric constants of rice plants at various growth stages are obtained from the gravimetric water content [82]. With the bottom part of the rice plants in water, the dielectric constant of the surface is $\epsilon_1 = 74 + i21$, the dielectric constant of water at the frequency of 5.3 GHz at 20° [81]. In the simulation, the average spacing between two rice bunches is about 25 cm. We also assume that the height of a stem has a normal distribution with the standard deviation of 1 cm. The backscattering coefficients are calculated using equation 2.24. The scattered field is averaged over 50 realizations until it is converged.

In Figure 3-3, the simulated HH backscattering returns at 23° incident angle are compared with the RADARSAT data [57] for different growth stages. The comparison shows good agreements between the simulation results and experimental data. The increasing trend of the temporal radar response is well described by the modeling results. The backscattering returns are mainly from the volume-surface interactions. Since the bottom parts of rice plants are immersed in water, the contribution of the second, third and fourth scattering mechanisms described in Chapter 2 to the total scattering from the rice canopy is very large compared to the case of other vegetation fields. Figure 3-4 shows the temporal response of HH backscattering coefficients when the incident angle is 43 degrees. The result shows a trend similar to the case of 23

age (days)	20	40	60	80	100
height H (cm)	11.2	26.3	43.6	61.0	76.7
stem radius c (cm)	0.11	0.15	0.18	0.21	0.23
# stems per bunch N_s	3	6	13	20	24
# bunches N_c/A (m^{-2})	9	9	9	9	9
gravimetric water content	0.71	0.77	0.80	0.80	0.75
dielectric constant ϵ_s, ϵ_ℓ	25.7+i8.1	29.6+i9.2	31.7+i9.8	31.7+i9.8	28.3+i8.8
leaf width w (cm)	0.43	0.78	1.06	1.3	1.34
leaf length ℓ (cm)	11.75	21.89	30.44	40	40.5
leaf thickness d (cm)	0.02	0.02	0.03	0.03	0.03
# leaves per stem N_ℓ	3	3	4	5	5
stem mean tilt angle θ_{ms} (deg)	0	2	7	11	11
leaf mean tilt angle $\theta_{m\ell}$ (deg)	0	7	14	20	25

Table 3.2: Input parameters for the simulation of backscattering coefficients of a rice field for comparison with RADARSAT data [57]. The parameters used in the simulation are determined either directly from the measurements obtained during the experiment or from the existing literature (mainly from IRRI [28]).

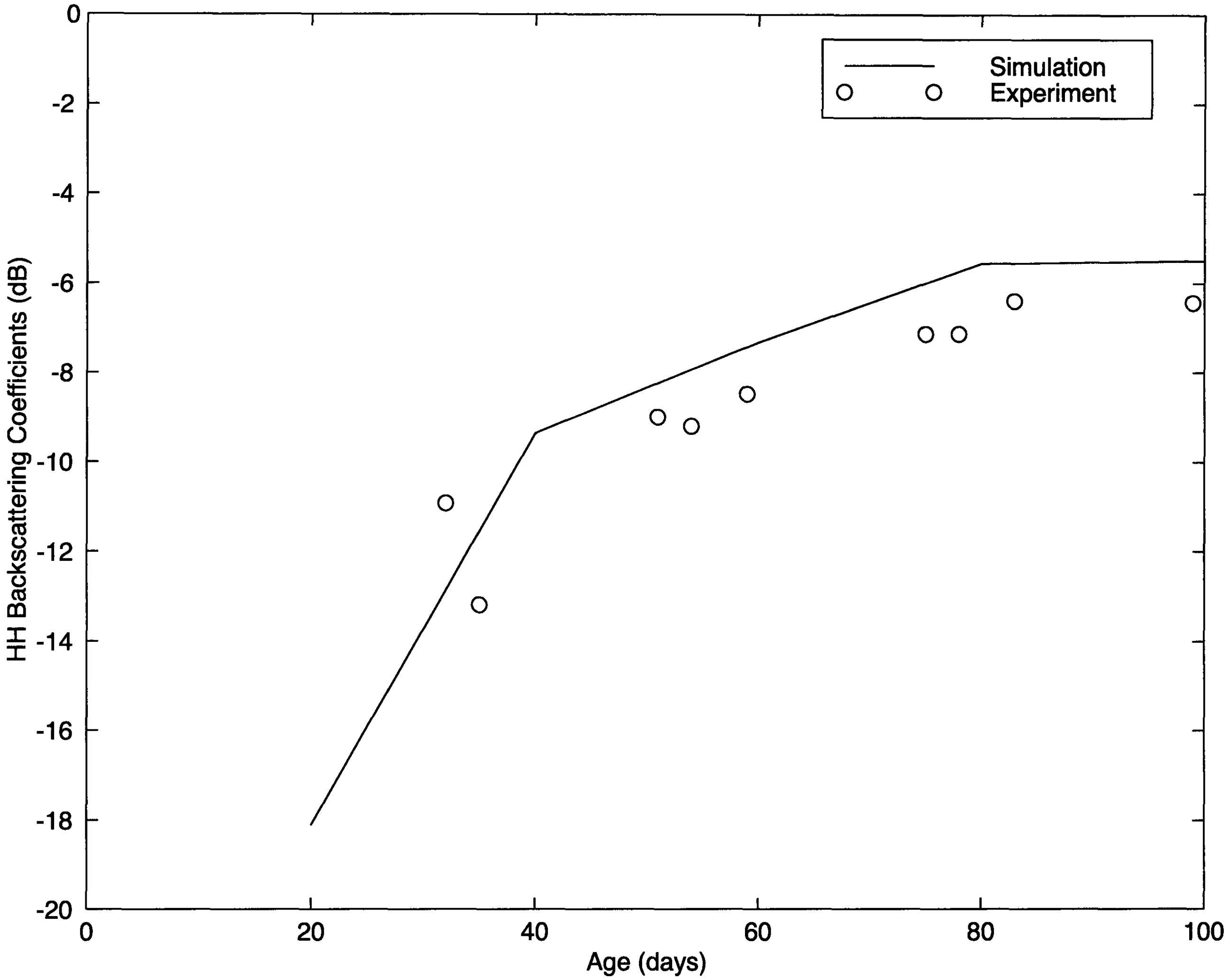

Figure 3-3: Comparison between the simulated HH backscattering coefficients and RADARSAT data [57] as a function of rice age. The frequency is at C-band, and the incident angle is 23°.

degrees except that there is only a very small increase in backscattering coefficients at higher growth stages. This is as expected because the attenuation caused by inhomogeneities in the medium is larger at the 43° incident angle than that at the 23° incident angle. This is a consequence of the fact that the distance traversed by the waves in the medium is longer with a greater incidence angle. This effect is more dominant at higher growth stages when the stems and leaves become larger.

3.2.4 Structure of Rice Fields

The scattering returns from the rice fields in Niigata, Japan acquired by JERS-1, which operated at L-band (1.25 GHz) with the incident angle of 35 degrees and one polarization HH, show that the structure of rice fields has a large effect on the returns [61]. Rice cultivation practices in Japan are different from those in Malaysia. Planting is performed by mechanical planting devices mounted on the back of small tractors. The spacing between rice plants in one direction can be very different from the spacing in the other direction. A question was raised in the paper by Rosenqvist and Oguma [61] regarding the planting direction which results in a higher scattering return. With the developed model and input parameters in Table 3.1, the dependence of radar backscattering returns on the geometric properties of the fields is investigated.

Assuming that the looking direction of the radar is in the x-direction and that the area is the same for all fields, the field structures considered include the following cases.

1. fields with equal spacing between rice plants ($a = b = 22$ cm)

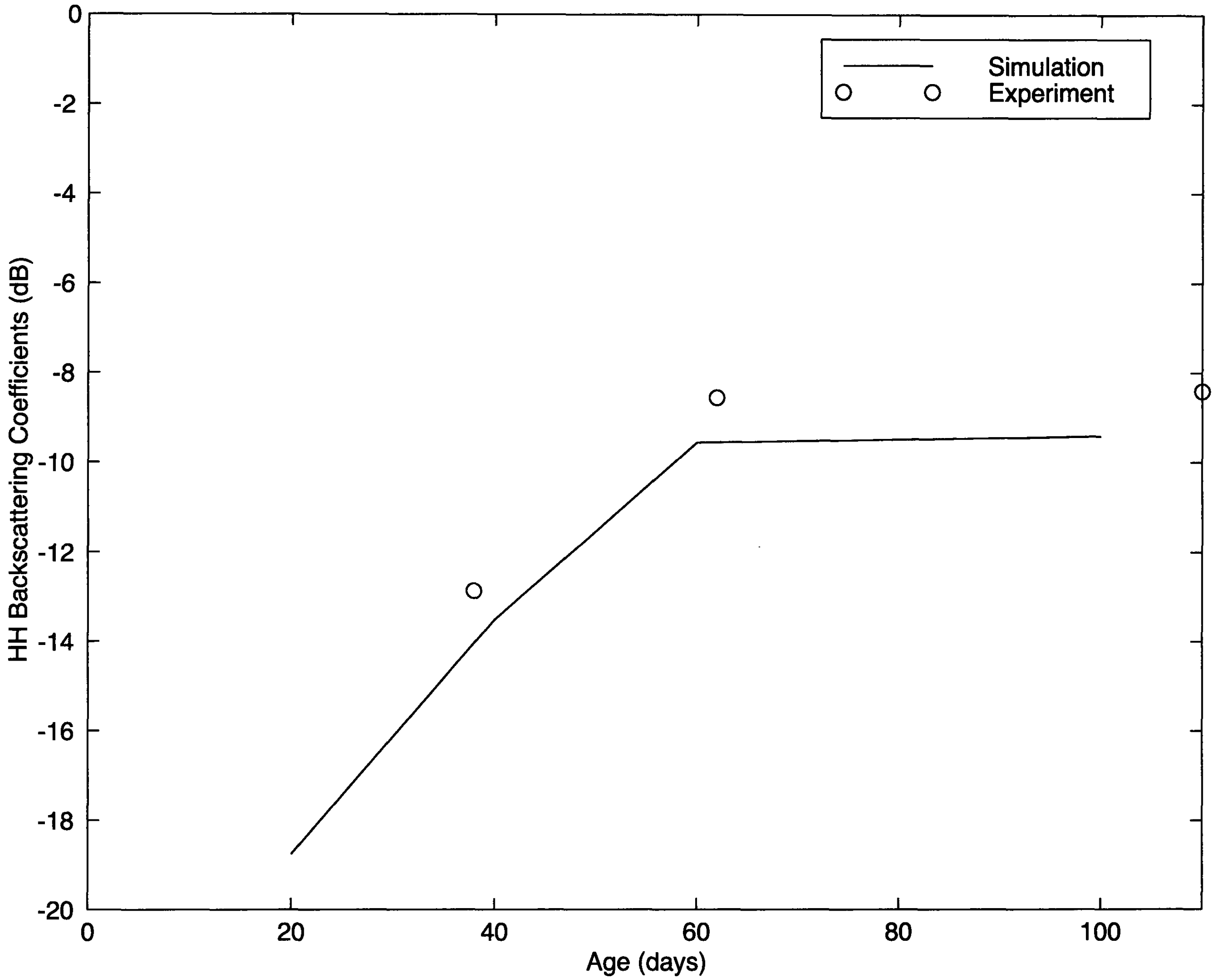

Figure 3-4: Comparison between the simulated HH backscattering coefficients and RADARSAT data [57] as a function of rice age. The frequency is at C-band, and the incident angle is 43°.

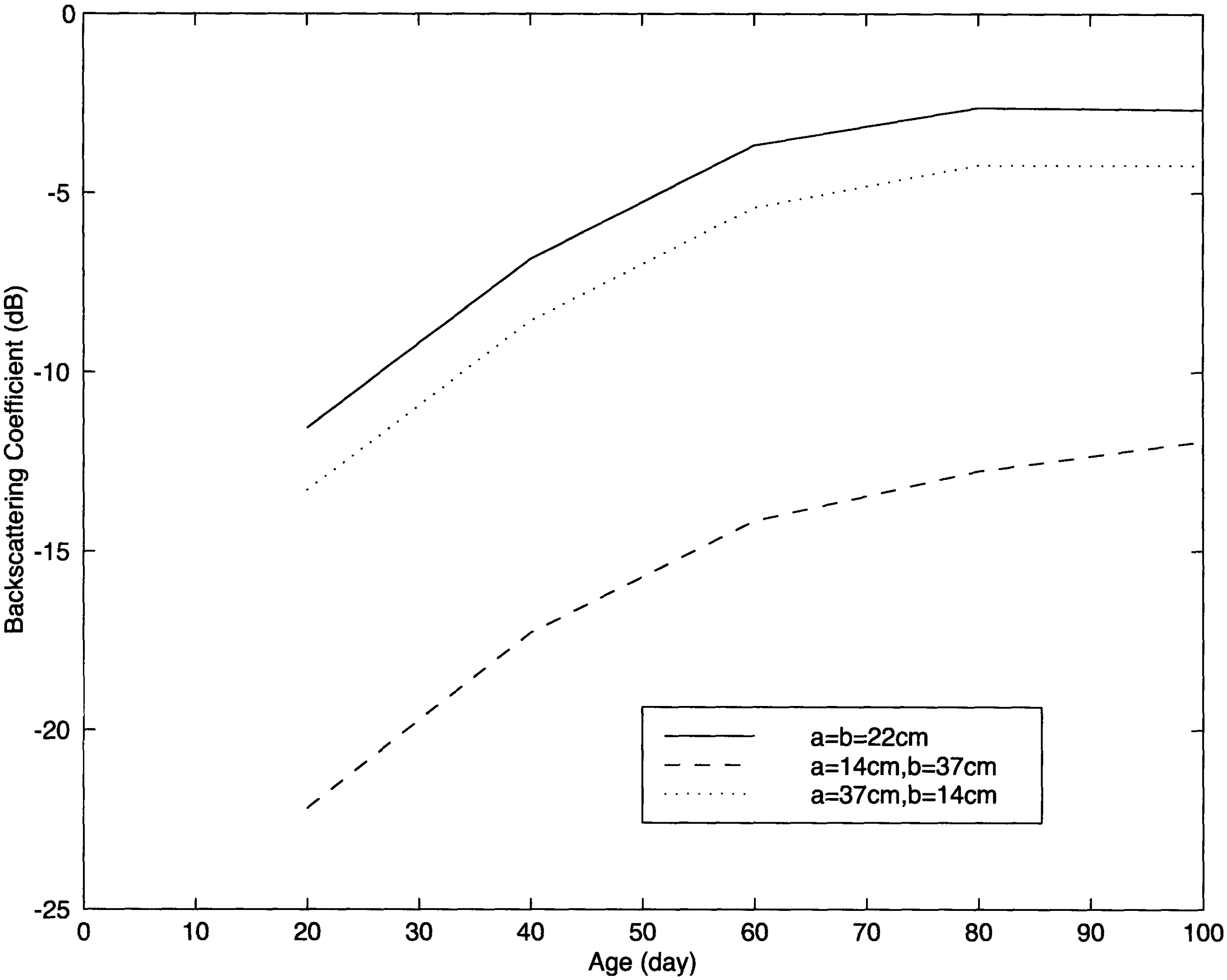

Figure 3-5: Simulated temporal variation of the L-band backscattering returns assuming the looking direction of the radar to be the x-direction. Simulated cases include fields with equal spacing between rice plants ($a = b = 22$ cm), fields with spacings $a = 14$ cm and $b = 37$ cm, and fields with spacings $a = 37$ cm and $b = 14$ cm.

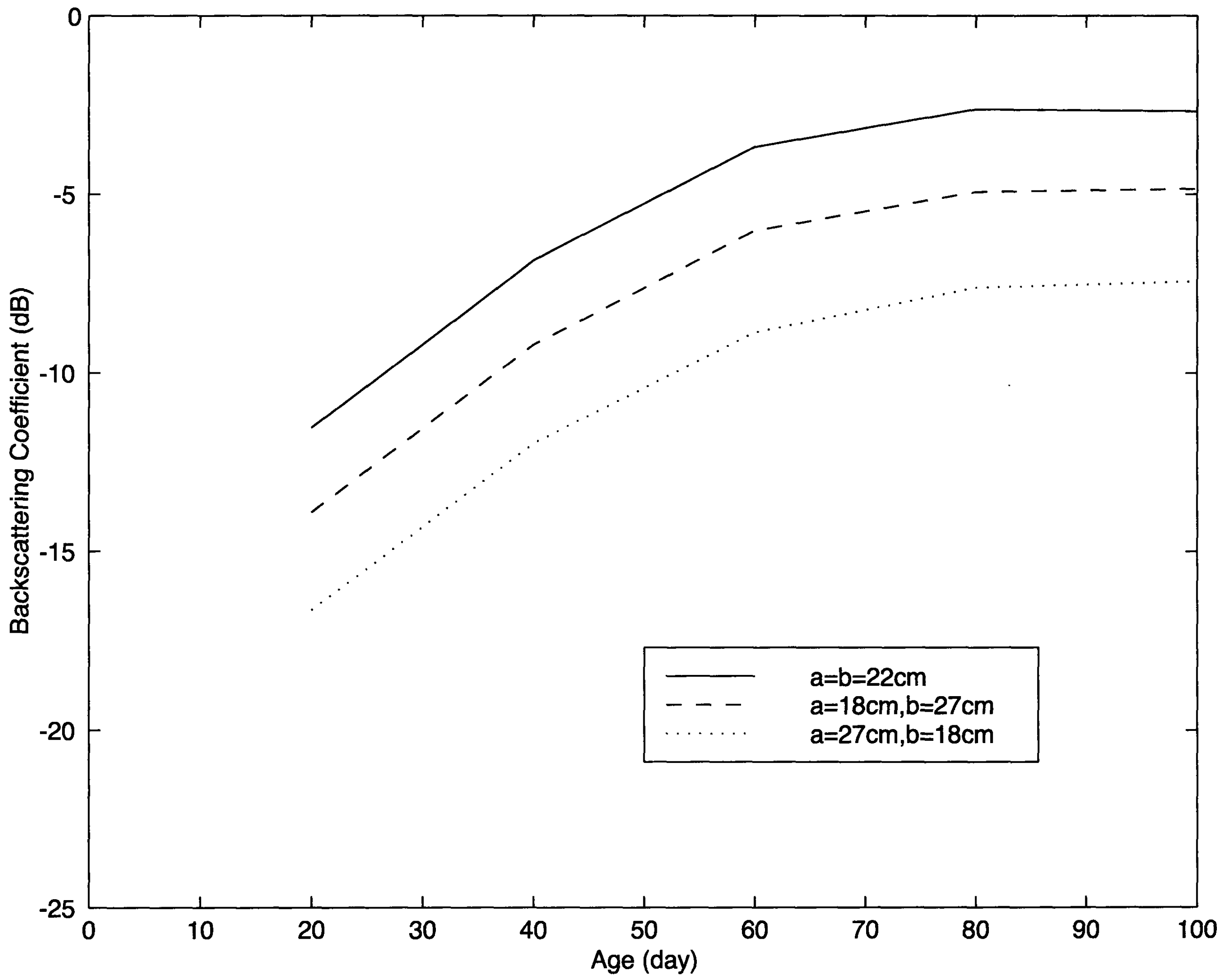

Figure 3-6: Simulated temporal variation of the L-band backscattering returns assuming the looking direction of the radar to be the x-direction. Simulated cases include fields with equal spacing between rice plants ($a = b = 22$ cm), fields with spacings $a = 18$ cm and $b = 27$ cm, and fields with spacings $a = 27$ cm and $b = 18$ cm.

2. fields with spacings $a = 14$ cm and $b = 37$ cm
3. fields with spacings $a = 37$ cm and $b = 14$ cm
4. fields with spacings $a = 18$ cm and $b = 27$ cm
5. fields with spacings $a = 27$ cm and $b = 18$ cm

a and b are the spacings in the x and y directions, respectively (Figure 3-1).

Figure 3-5 shows the simulated temporal variation of the L-band backscattering returns for cases 1 to 3. The overall shapes of the temporal curves are similar for all three cases. Compared to case 3, the backscattering return is about 8 dB lower for case 2 where a, the spacing in the radar looking direction, is smaller than spacing b in the direction perpendicular to the radar looking direction. The simulated L-band backscattering returns versus rice age for cases 1, 4 and 5 are given in Figure 3-6. Again, the overall shapes of the temporal curves are similar for all three cases. However, compare to case 5, the backscattering return is about 4 dB higher for case 4 where spacing a is smaller than spacing b. Therefore, it is not necessarily true that scattering returns are higher when the spacing in the radar looking direction is smaller than the spacing in the perpendicular direction. The magnitude of scattering returns depends on whether we have a constructive or destructive interference between rice plants, which is related to the spacing between the plants. With a large difference in the backscattering results because of the different structures of the rice fields, inversion will be difficult without the measurements on the plant spacings. However, we can expect less effect of the rice field structure on the returns since the wavelength at C-band is about 6 cm compared to 24 cm at L-band. Figure 3-7, which shows simulated temporal variations of the C-band backscattering results for cases 2 to 5 described above, confirms this point. The variations in backscattering returns are small for different directions and plant spacings.

If an L-band data set has both HH and VV polarizations, one possible way to perform the inversion without the measurements on the plant spacings is by taking the ratio of HH over VV. The plot of the L-band ratio versus the age of rice canopy for different plant spacings is shown in Figure 3-8. For the first 95 days, HH backscattering returns are higher than the VV returns since the dominant scattering mechanism is the volume-surface interactions. The reflection coefficient of the horizontal polarization is higher than that of the vertical polarization. The ratios have a decreasing trend after 40 days because the attenuation increases. With water as the underlying surface, the plot for the ratio of HH over VV is different from that of other types of vegetation. This ratio of HH over VV can therefore be utilized for the classification of the rice canopy. The results are very close for different spacing between rice plants. Taking the ratio has the effect of canceling out the phase interactions from the structure of the rice field and provides a useful parameter for the inversion of rice biomass.

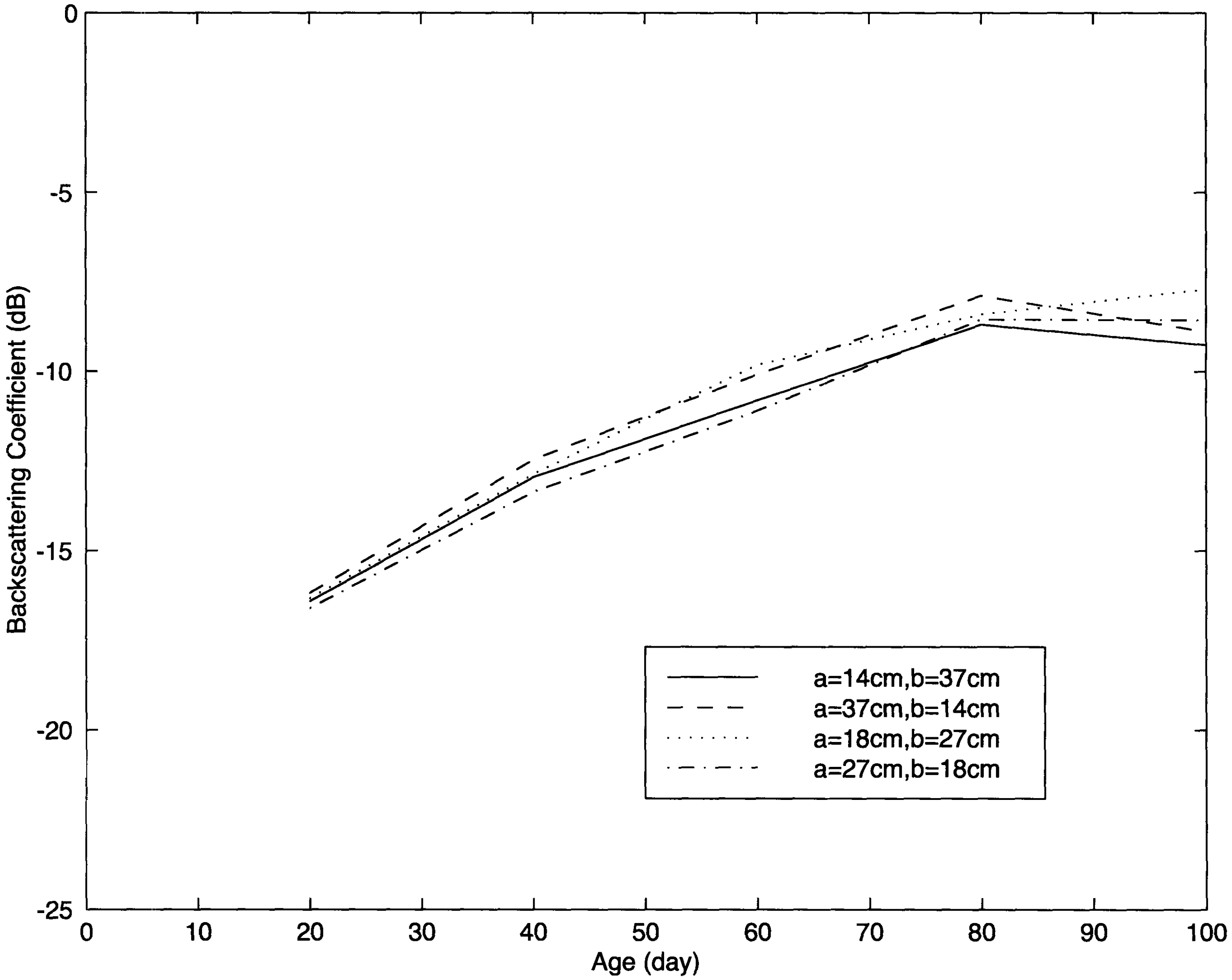

Figure 3-7: Simulated temporal variation of the C-band backscattering returns assuming the looking direction of the radar to be the x-direction. Simulated cases include fields with spacings $a = 14$ cm and $b = 37$ cm, fields with spacings $a = 37$ cm and $b = 14$ cm, fields with spacings $a = 18$ cm and $b = 27$ cm, and fields with spacings $a = 27$ cm and $b = 18$ cm.

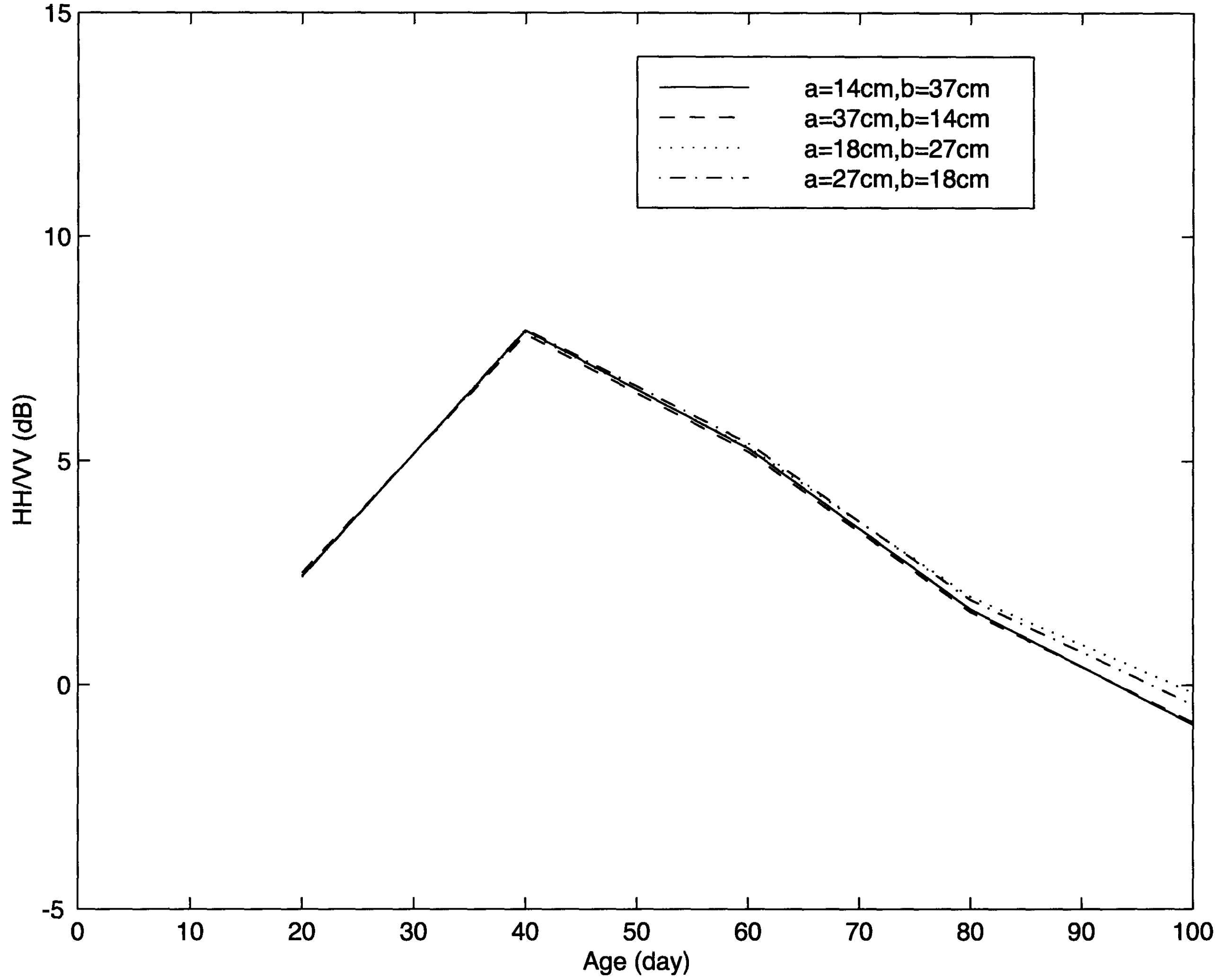

Figure 3-8: Simulated temporal variation of the ratio of L-band co-polarized backscattering coefficients, HH over VV, assuming the looking direction of the radar to be the x-direction. Simulated cases include fields with spacings $a = 14$ cm and $b = 37$ cm, fields with spacings $a = 37$ cm and $b = 14$ cm, fields with spacings $a = 18$ cm and $b = 27$ cm, and fields with spacings $a = 27$ cm and $b = 18$ cm.

3.3 Application to Sunflower Fields

During the airborne Remote Sensing Campaign Mac-Europe 91, multi-frequency and multi-polarization data were acquired for sunflower fields at the test site Montespertoli in Italy [5]. The structure of a sunflower is quite different from that of a rice plant. It does not have a cluster structure, and its more circular shaped leaves are connected to a stem through petioles. In addition, there is a flower at the developed stage. Unlike rice fields, the bottom of a sunflower field is the rough soil surface instead of water. In this section, the structural model is applied to interpret the radar backscattering returns from sunflower fields, and the simulation results are validated by the experimental data.

3.3.1 Structure of Sunflowers

To model the scattering from sunflower fields, we consider the field of sunflowers planted with nearly constant spacing over a square area A (Figure 3-9). Small random variations are introduced into the spacing between sunflowers. In the early growth stage, each sunflower contains a main vertical dielectric cylindrical stem, and leaves of elliptical disc shape connected to the main stem through cylindrical petioles. In the later stages, sunflowers also include flowers of circular disc shape. The height of the vertical stems are generated randomly with a Gaussian distribution given the mean and the standard deviation of the height. The tilted stems, leaves, and petioles have random orientations; the tilt angles vary randomly within a specified range. In

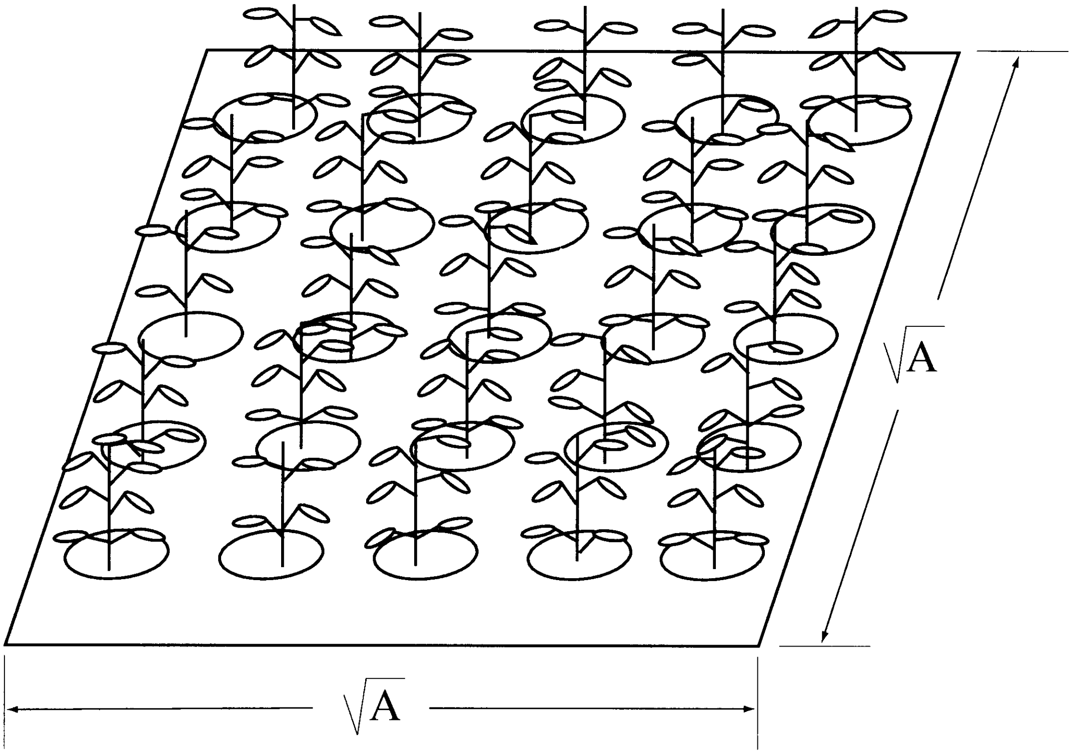

Figure 3-9: Configuration of a sunflower field for the scattering model. Sunflowers are planted over a square area A.

the early growth stage, the tilt angles for most leaves are less than 90 degrees from the vertical direction. As the leaves become larger at the developed stage, the tilt angles for most leaves become greater than 90 degrees from the vertical direction.

Given the configuration of the sunflower field and an incident wave $\bar{E}_i$ in the direction (θ_i, ϕ_i), the total backscattered electric field includes the direct scattering from the ground which is modeled as a rough surface, and the field due to the four scattering mechanisms described in equation 2.23. It consists of the summation of three types of scatterers in the early growth stage: stems, leaves, and petioles. In the developed stage, flowers are added. For a sunflower field, equation 2.20 becomes

$$M_{qp} = \frac{i2\pi}{k_0}\frac{N_s}{Ah}\left(< f_{qp}^{\text{stem}}(\theta,\phi;\theta,\phi) > + N_\ell < f_{qp}^{\text{leaf}}(\theta,\phi;\theta,\phi) > + N_\ell < f_{qp}^{\text{petiole}}(\theta,\phi;\theta,\phi) >\right) \tag{3.6}$$

where N_s is the number of stems, and N_ℓ is the number of leaves or petioles for a single sunflower. The Kirchhoff approximation [74] is employed to calculate the direct scattering from the rough soil surface, and the reflection coefficients for the second, third and fourth scattering mechanisms. In this approximation, the field at a given point of a surface is assumed to be the same as the field that would be present on the tangent plane at that point . The surface height and the surface correlation function are assumed to have a Gaussian distribution. The rough surface is described by the surface root-mean-square (rms) height and correlation length.

In each realization of the Monte Carlo simulation, the center positions of stems are first specified. Then the positions and orientations of the petioles on each stem and the leaf on each petiole are generated randomly. The scattered electric field is calculated in each realization. The backscattering coefficient of the sunflower field is obtained from equation 2.24and by averaging over an ensemble of realizations.

3.3.2 Comparison with Experimental Data

In this section, the simulated backscattering results at different growth stages are compared with the experimental data obtained from the Montespertoli test site during the airborne Remote Sensing Campaign Mac-Europe 91 which has four polarizations: HH, VV, HV and VH, and include two frequencies: L-band (1.25 GHz) and C-band (5.3 GHz) [5]. The incident angle is 35 degrees. The data are from four different sunflower fields collected during three flights on different dates over these fields. Figure 3-10 shows the L-band backscattering coefficient versus the sunflower biomass. Since there are three flights and four areas for each flight, there are twelve data points for each polarization. The increasing trend of co-polarized and cross-polarized scattering returns is observed with the increase in sunflower biomass. The backscattering returns for C-band are shown in Figure 3-11. The co-polarized and cross-polarized returns remain constant when the sunflower biomass increases because scattering from the rough surface becomes larger at C-band.

The parameters used in the simulation of backscattering coefficients of sunflower fields are summarized in Table 3.3. There were four fields: field 12, field 16, field 17 and field 54. For the first flight, all four fields were in the early growth stage and there were no flowers. For the second flight, there were still no flowers for fields 12 and 16, but sunflowers in fields 17 and 54 began to enter the developed stage

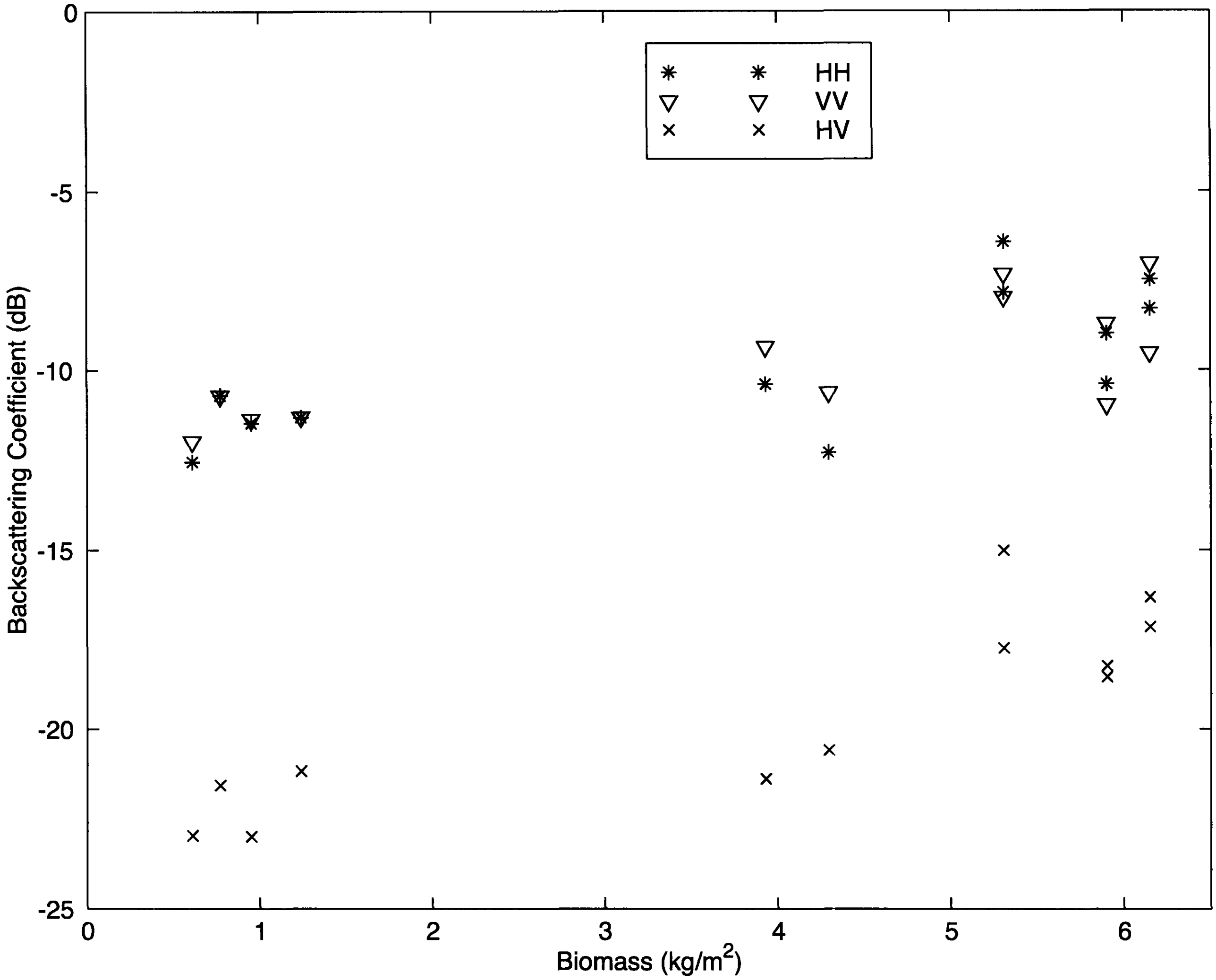

Figure 3-10: L-band Mac-Europe 91 data [5] for sunflower fields at 35° incident angle. The data are from four different sunflower fields collected during three flights on different dates over these fields.

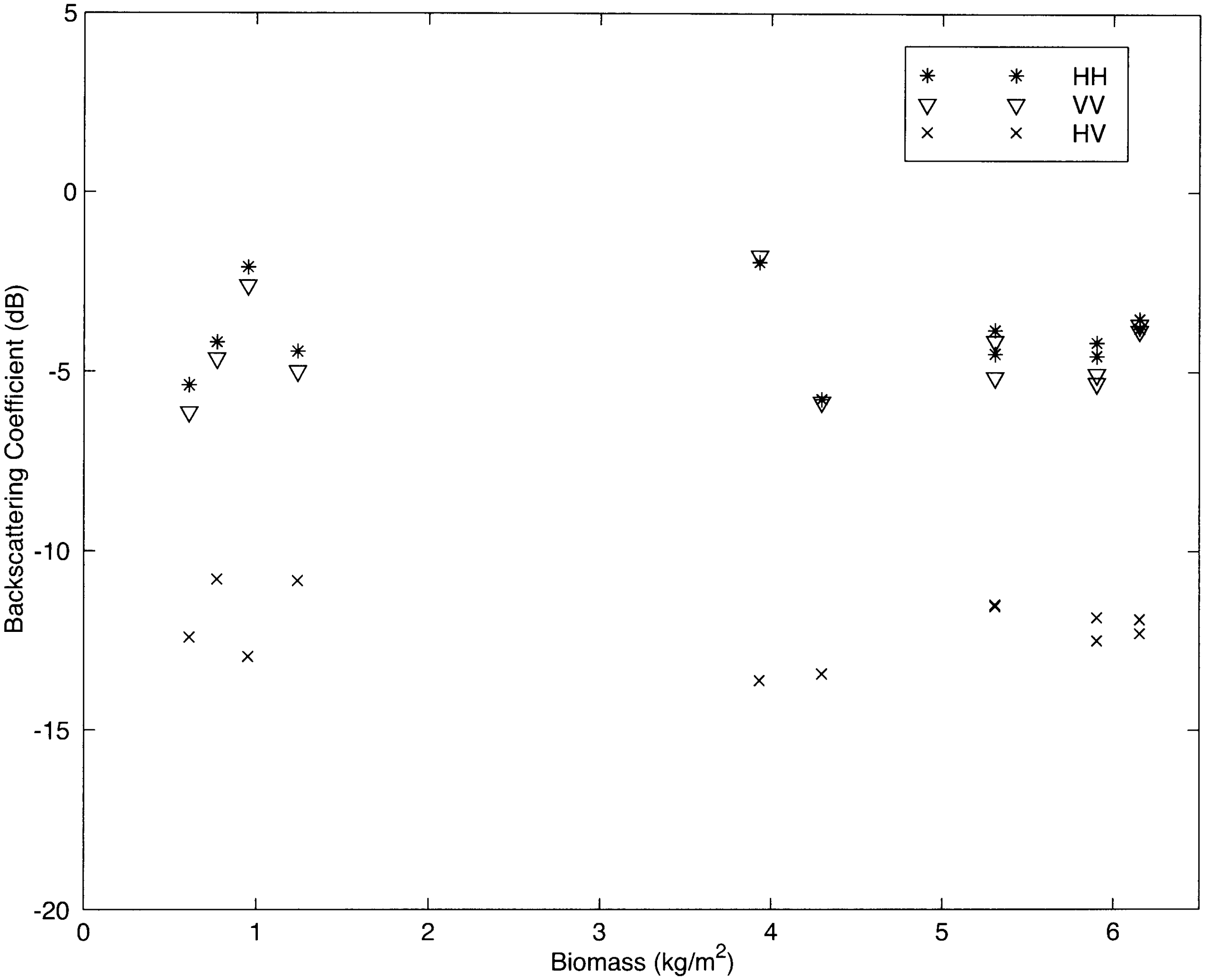

Figure 3-11: C-band Mac-Europe 91 data [5] for sunflower fields at 35° incident angle. The data are from four different sunflower fields collected during three flights on different dates over these fields.

with the growth of flowers. The sunflowers in all four fields were in the developed stage during the third flight. The parameters used in the simulation are determined from the measurements. Using equation 3.2, the dielectric constants of sunflowers are calculated from the gravimetric water content [82]. Leaf area index in Table 3.3 is the area of all the leaves in a unit area of the field. Therefore, it is equal to the product of the area of a leaf, the number of leaves per plant and the plant density. The thickness of a sunflower leaf changes from 0.01 cm in the early growth stage to 0.04 cm in the developed stage. The tilt angle for leaves varies from 40° to 120° from the vertical direction, with the larger tilt angle at the developed stage. The rms height and correlation length which characterize the rough soil surface are 1.25 cm and 5.0 cm, respectively. The soil permittivity is calculated from the soil moisture and the assumed soil texture shown in Table 3.3 from an empirical formula [19]. In the simulation, the average spacing between two sunflowers is about 30 cm. The backscattering coefficients are obtained using equation 2.24. The scattered field is averaged over 50 realizations until it is converged. Figure 3-12 and Figure 3-13 depict the simulation results versus the experimental data for L-band and C-band, respectively. The solid line in the figures represents the ideal case where there is an exact match. Both figures show a good agreement between the simulation results and the experimental data for co-polarized returns and cross-polarized returns.

flight #	field #	main stem height (cm)	main stem radius (cm)	plant density ($\#/m^2$)	gravimetric water content	leaf area index	leaf diameter (cm)	soil moisture (%)
1	12	40	0.61	10	0.9	0.6	8	12.2
1	16	40	0.61	9	0.9	0.4	8	14.8
1	17	95	1.225	8	0.9	3.6	16	17.4
1	54	95	1.225	8	0.9	3.6	16	17.4
2	12	65	0.575	10	0.88	0.9	9	11.6
2	16	65	0.575	10	0.87	0.5	9	11.6
2	17	110	1.335	10	0.91	4.1	26	4
2	54	110	1.335	10	0.91	4.1	26	4
3	12	110	1.07	10	0.86	2.6	15	6.3
3	16	110	1.07	10	0.86	1	15	5.8
3	17	160	1.065	9	0.85	2.8	20	6.7
3	54	160	1.065	9	0.85	2.8	20	6.7

Table 3.3: Input parameters for the simulation of backscattering coefficients of sunflower fields for comparison with Mac-Europe 91 data [5]. The parameters used in the simulation are determined from measurements.

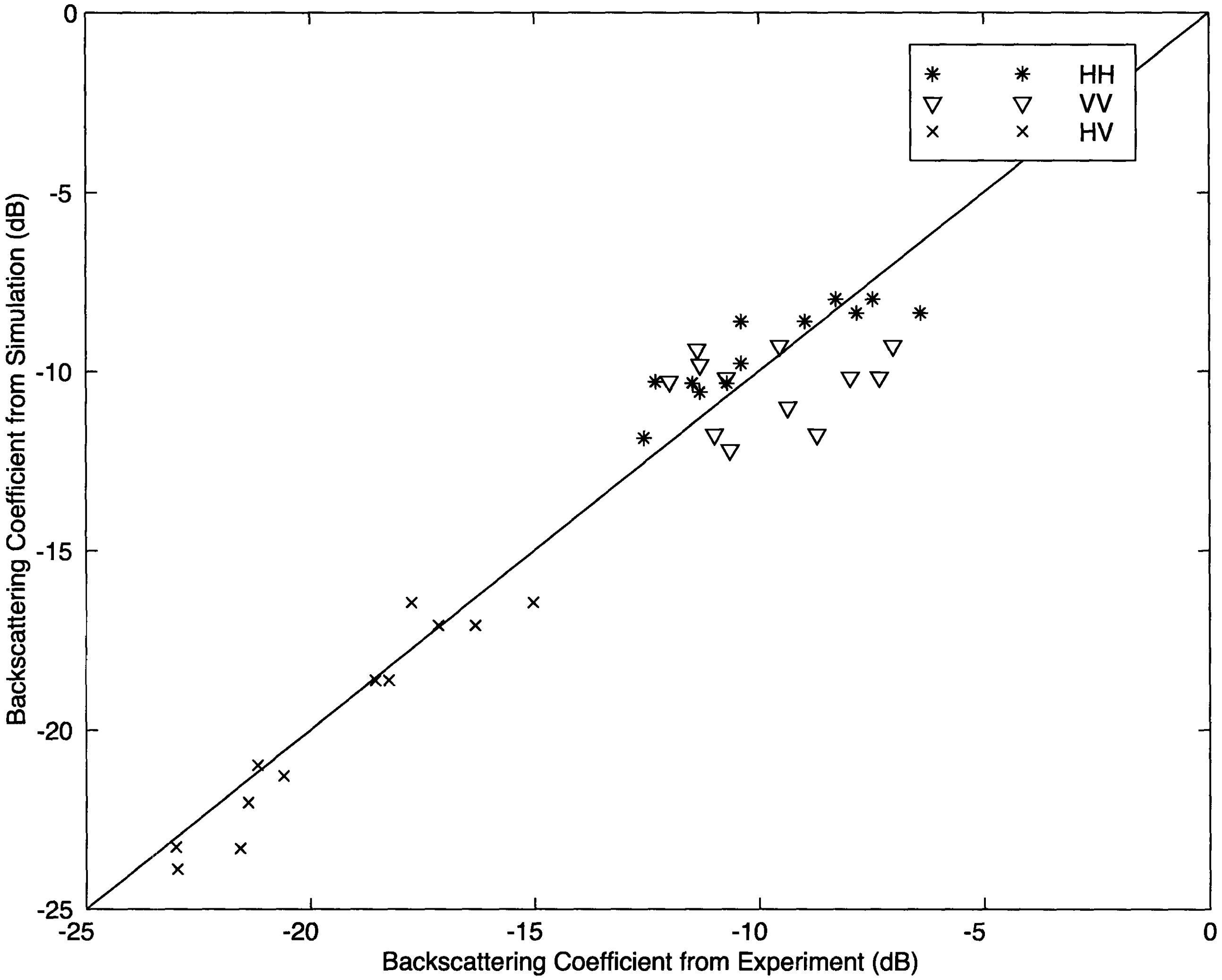

Figure 3-12: Comparison between the simulated backscattering coefficients from a sunflower field and Mac-Europe 91 data [5]. The frequency is at L-band.

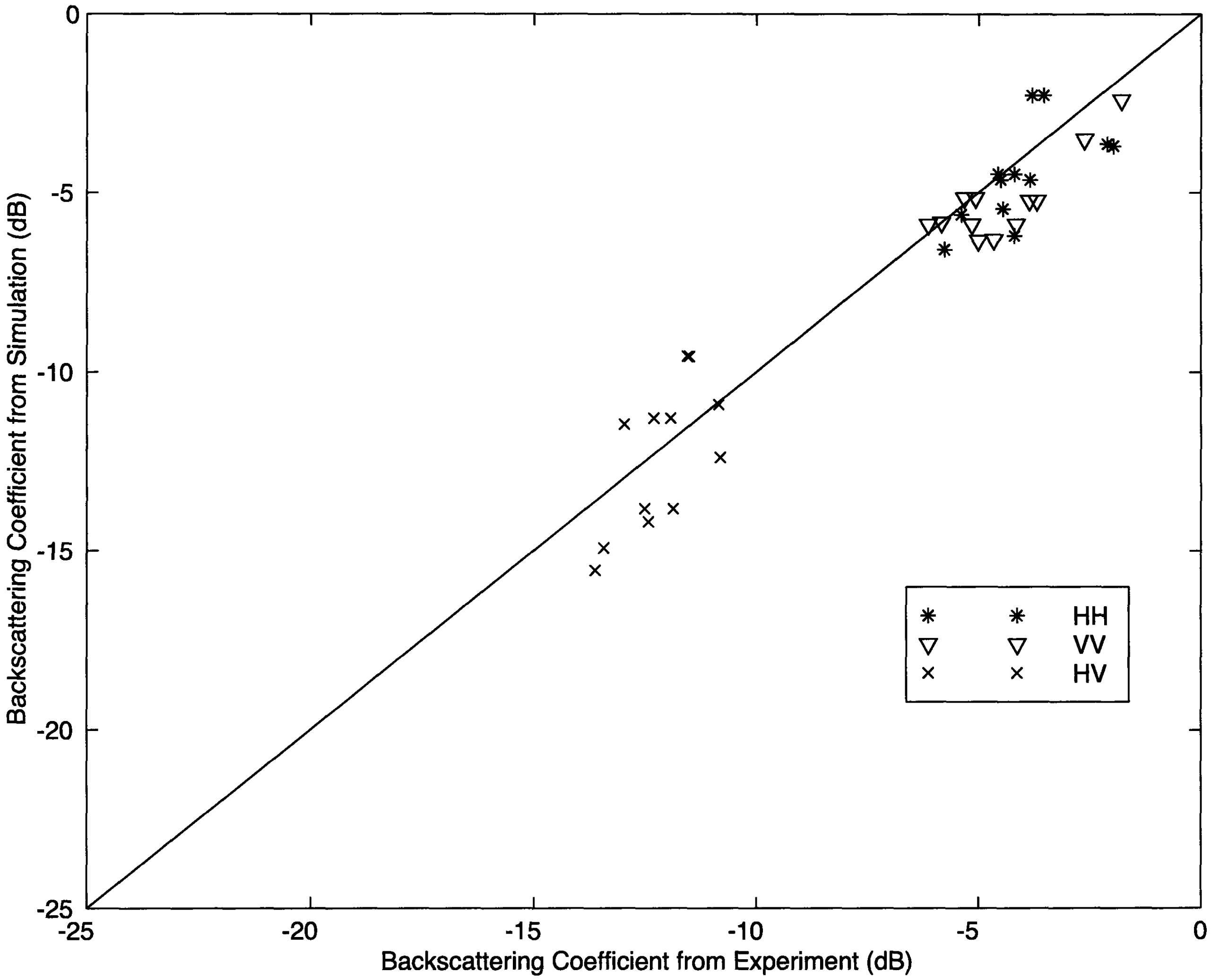

Figure 3-13: Comparison between the simulated backscattering coefficients of a sunflower field and Mac-Europe 91 data [5]. The frequency is at C-band.

3.4 Summary

In this chapter, a structural model is developed. Based on the ground truth measurements, the distinct structures for different vegetations can be specified by the types of components, the number and size of each type of component, and the orientation and branching angles of the components. By characterizing the vegetation structure with levels of detail, the detailed features of distinct vegetation structures can be preserved to the desired level of accuracy. In the Monte Carlo simulation, the configurations are generated from the characterization of vegetation structure. The applications of the structural model to rice crops and sunflowers are described in this chapter.

Since rice plants usually occur in clusters and are closely spaced, a good structural model which takes into account the structure of rice plants and rice fields and the coherence or phase interference among vegetative elements is essential. It is validated with the ERS-1 data acquired at the C-band frequency of 5.3 GHz and the incident angle of 23 degrees [41], and with the RADARSAT data at the C-band frequency of 5.3 GHz and two incident angles of 23 and 43 degrees [57]. The polarizations of the ERS-1 and RADARSAT data are VV and HH, respectively. The comparison between the simulated backscattering results and both the ERS-1 and RADARSAT data show good agreement. The increasing trend of the temporal radar response is well described by the modeling results. This increase can be explained by the increase in biomass and by the highly reflective underlying flooded surface of the rice fields during the growth period.

To answer a question raised in the paper by Rosenqvist and Oguma [61] regarding the planting direction which results in a higher scattering return, the structural model is also applied to investigate the dependence of radar backscattering returns on the geometric properties of the fields. Simulations were performed to interpret the returns at different growth stages for various rice field structures. The result shows that at L-band, the variation in the scattering returns from rice fields with different structures can be large because of constructive and destructive interferences between rice plants as the result of different plant spacings. Without knowing of the plant spacing, inversion of rice biomass from the scattering results will be difficult at L-band. For C-band, the rice field structure has less effect on the returns because the wavelength at C-band is about 6 cm compared to 24 cm at L-band. However, if the L-band data has both HH and VV polarizations, taking the ratio of HH over VV has the effect of canceling out the phase interactions from the structures of rice fields and is useful for the inversion of biomass without the knowledge of plant spacings.

In addition to the rice canopy, the application of the structural model to sunflowers is also discussed in this chapter. In contrast to a rice plant, a sunflower does not have a cluster structure, its more circular shaped leaves are connected to a stem through petioles, and there is a flower at the developed stage. In addition, the bottom of a sunflower field is the rough soil surface instead of water. The structural model is applied to interpret the multi-frequency, multi-polarization radar backscattering returns from four different sunflower fields acquired during three flights on different dates for the airborne Remote Sensing Campaign Mac-Europe 91 at the Montespertoli test site in Italy [5]. The result shows a good agreement between the model simulation and the experimental data for co-polarized returns and cross-polarized returns.

Chapter 4

Lindenmayer Systems

A major problem in the modeling of vegetation lies in the modeling of their complex structural and time-varying properties. The application of growth rule-based model is especially useful to generate trees which are more complex in structure. To fully capture and describe the architecture and growth of plants, the formalism of Lindenmayer systems has been utilized [52, 53, 54, 55, 68]. Trees generated by L-systems are quite realistic in appearance. In the first section of this chapter, an introduction to L-systems is given. From L-systems, the position, size, and orientation of every element in a generated tree can be obtained. Monte Carlo simulation results of the scattering returns from trees generated by L-systems at different growth stages and of different types are analyzed in Sections 2 and 3, respectively.

4.1 Introduction

The L-systems approach was proposed by Lindenmayer for simulating the development and growth of living systems [44]. For simulation of plants, it emphasizes the plant topology which specifies the neighboring relations between plant modules. The central concept of L-systems is rewriting which defines complex objects by successively replacing parts of a simple initial object using a set of rewriting or production rules. The rewriting rules are applied in parallel and are carried out recursively in the simulation of plant growth processes.

Prusinkiewicz used a LOGO-style turtle [1] to interpret L-systems graphically. The state of the turtle is specified using a triplet (x,y,α), where (x,y) represents the position of the turtle, and the angle α specifies the direction which the turtle is facing. To denote the movement of the turtle, four symbols F, f, $+$, $-$ are used. "F" represents a movement of a given step size s with a line drawn from (x,y) to the new point (x',y'), where $x' = x + s \cos\alpha$ and $y' = y + s \sin\alpha$. "f" is the same as "F" except that a line is not drawn between the two points. "$+$" and "$-$" control angle movement. "$+$" makes the turtle rotate in the counterclockwise direction by the angle increment δ. Thus, the next state of the turtle is $(x,y,\alpha+\delta)$. "$-$" represents rotation by angle δ in the clockwise direction such that the next state of the turtle is $(x,y,\alpha - \delta)$.

For modeling in three dimensions, the orientation of the turtle is represented by three unit vectors $\overline{U}$, $\overline{V}$, and $\overline{W}$. The unit vector $\overline{U}$ points to the direction the turtle is facing. These vectors are perpendicular to one another and satisfy the equation $\overline{U} \times \overline{V} = \overline{W}$. Rotating the turtle is represented by applying rotation matrices to these three vectors. The rotation by angle δ about the vector $\overline{W}$, that is, the rotation on the plane formed by vectors $\overline{U}$ and $\overline{V}$, can be represented by the rotation matrix $R_W(\delta)$.

$$R_W(\delta) = \begin{pmatrix} \cos\delta & \sin\delta & 0 \\ -\sin\delta & \cos\delta & 0 \\ 0 & 0 & 1 \end{pmatrix} \tag{4.1}$$

Similarly, the rotation by angle δ about the vector $\overline{V}$ (on the plane formed by vectors $\overline{U}$ and $\overline{W}$) and about the vector $\overline{U}$ (on the plane formed by vectors $\overline{V}$ and $\overline{W}$) are represented by rotation matrices $R_V(\delta)$ and $R_U(\delta)$, respectively.

$$R_V(\delta) = \begin{pmatrix} \cos\delta & 0 & -\sin\delta \\ 0 & 1 & 0 \\ \sin\delta & 0 & \cos\delta \end{pmatrix} \tag{4.2}$$

$$R_U(\delta) = \begin{pmatrix} 1 & 0 & 0 \\ 0 & \cos\delta & \sin\delta \\ 0 & -\sin\delta & \cos\delta \end{pmatrix} \tag{4.3}$$

Therefore, the new state of the turtle is

$$\begin{pmatrix} \overline{U'} & \overline{V'} & \overline{W'} \end{pmatrix} = \begin{pmatrix} \overline{U} & \overline{V} & \overline{W} \end{pmatrix} R \tag{4.4}$$

The symbols used to control the turtle orientation are summarized in the following table.

Symbol	Rotation Matrix
$+$	$R_W(\delta)$
$-$	$R_W(-\delta)$
&	$R_V(\delta)$
$\wedge$	$R_V(-\delta)$
$\backslash$	$R_U(\delta)$
$/$	$R_U(-\delta)$
$\vert$	$R_W(180°)$

Although the use of turtle interpretation described above provides L-systems with the capability of generating a variety of objects, it has limited ability to capture some phenomena associated with plant development. To overcome these limitations, parametric L-systems were developed [45, 56]. With parametric L-systems, numerical parameters can be associated with L-system symbols, allowing the specification of the condition for application of the production rule, where the symbols : and → are used to separate the three components of a production rule—the predecessor, the condition, and the successor. For example, the production rule `p1` specified by

$$\texttt{p1 : A(x) : x>=1} \rightarrow \texttt{A(x-1)}$$

means that $A(x)$ will be replaced by $A(x-1)$ if $x \geq 1$. To control the turtle movement in the parametric L-system, the symbols used are similar to those described previously, and are modified to include the parameters introduced. $F(a)$ represents a forward movement of a step size $a > 0$ with a line drawn between the previous location and the new point. For a forward movement with step size a without drawing a line, lower-case $f(a)$ is used. The symbols $+(a)$, $\&(a)$ and $/(a)$ represent rotation by angle a around the three orthonormal vectors $\overline{W}$, $\overline{V}$ and $\overline{U}$, respectively. As in the non-parametric case, default values will be used if a symbol is not followed by any parameter.

To model the branching structure of a plant, several other symbols are introduced. To delimit a branch, the symbol " [" represents the start of a branch, and "] " represents the completion of a branch. When the symbol " [" is encountered, the current state of the turtle is put on a stack which stores the information such as the position and orientation of the turtle, and color and width of lines being drawn. The information is retrieved from the stack with the symbol "] ", and the state popped from the stack becomes the current state of the turtle. Other useful operations include $!(w)$ which sets the line width to w, and \$ which rolls the turtle around its own axis such that the unit vector $\overline{V}$ pointing to the left of the turtle becomes horizontal. The latter \$ is especially useful for specifying the growth of certain types of trees where the branch plane is closest to a horizontal plane.

Since in reality, there are variations among plants of the same type, it is useful to introduce variations in the L-systems which preserve the general aspects of a plant while allowing variation in its details. There are two approaches to achieve this effect. The first one incorporates randomization of the turtle interpretation; that is, the geometric aspects of a plant such as the branch angles and stem lengths are randomized. However, limited effects are achieved since the underlying topology remains unchanged. In the second approach to randomize the L-system, a production rule specifies a probability distribution of state transitions. This affects both the topology and the geometry of the plant. The trees generated using such stochastic L-systems are quite realistic in appearance.

The inputs for generating different kinds of trees using L-systems include the definition section, the initial string, and the production rules. The following is an example of an input to the L-systems. It is based on the model proposed by H. Honda who has studied extensively the forms of trees [22, 23]. In his model, tree segments are assumed to be straight. For one branching process, two daughter segments are produced by a mother segment. The mother segment and its two daughter segments lie on the same branch plane, which is fixed with respect to the direction of gravity such that the branch plane is closest to a horizontal plane. In other words, the line on the branch plane perpendicular to the mother segment is horizontal.

```
#define maxgen 10


#define r1 0.85+0.1*rand()   /* contraction ratio for the straight branch */

#define r2 0.6               /* contraction ratio for the lateral branch */

#define a0 40+10*rand()      /* branching angle from the trunk */

#define a2 40+10*rand()

                    /* branching angle for branches not attached to the trunk*/

#define d  132.5+10*rand()   /* divergence angle */

#define wr 0.707             /* width decrease rate */
```

```
START : A(1,10)


p1 : A(l,w) : * -> !(w)F(l)[&(a0)B(l*r2,w*wr)]/(d)A(l*r1,w*wr)

p2 : B(l,w) : * -> !(w)F(l)[-(a2)$C(l*r2,w*wr)]C(l*r1,w*wr)

p3 : C(l,w) : * -> !(w)F(l)[+(a2)$B(l*r2,w*wr)]B(l*r1,w*wr)
```

In the first section of the above example, we specify the maximum number of growth stages `maxgen`, which is also the default value if the number of growth stages is not given during the simulation. The relationship between a mother segment and daughter segments during the growth process is specified by changes in length and width, as well as the branching angles. These are specified in the definition section by the contraction ratio for the straight daughter branch (`r1`), the contraction ratio for the lateral daughter branch (`r2`), the width decrease rate (`wr`), the branching angle for branches arising from the trunk (`a0`), and the branching angle for branches not directly attached to the trunk (`a2`). The divergence angle `d` specifies the angle between two successive branch planes for branches coming off the trunk. Since there are variations among real trees of the same type, certain aspects of the geometry of a tree are randomized with the use of a random number generator `rand()` in the example above.

The initial string `A(1,10)` specifies a starting trunk which has one unit of length and 10 units of width. The production rules `p1`, `p2` and `p3` are then defined. Each application of the production rule `p1` results in an extension (`F`) of the trunk giving off a straight branch (`A`, which is applied recursively) and a lateral branch (`B`). The production rule `p1` decreases the length and width of the daughter segments with respect to the mother segment by the factors `r2` and `wr`, respectively. The subsequent development of the lateral branches are described by production rules `p2` and `p3`. In each growth step, a lateral branch of the next order is generated at angle `a2` or `-a2` with respect to the mother axis using the production rule `p2` or `p3`. Two production rules are needed in order to create lateral branches alternately to the left and right of the mother branch. Figure 4-1 shows the generated tree at growth stage 10.

From L-systems, we have the information on the position, size, and orientation of every element in a generated tree. Scattering from the generated tree can then be calculated using the Monte Carlo approach described in Chapter 2. In each realization, the finite cylinder approximation is applied to compute the scattering from each branch. The scattered fields from all branches are added coherently to calculate the total scattered field. The results from many tree realizations are then averaged. Using this growth rule-based model, we can study the scattered returns from trees of different structures at different growth stages.

4.2 Application to Trees at Different Growth Stages

With L-systems, we can simulate trees at different growth stages. In this section, the simulation of the growth of a ternary tree is described. The output of L-systems is

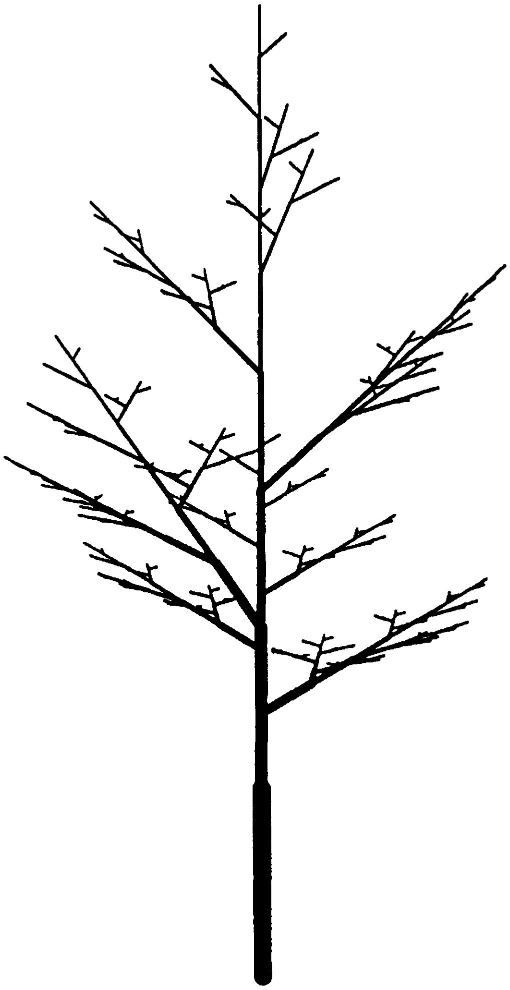

Figure 4-1: A tree generated using L-systems based on the model proposed by Honda.

then utilized to calculate the scattering from ternary trees at different growth stages.

"Ternary" trees are so named because in each growth stage, three branches are produced from every terminal branch of the previous stage. In contrast to the Honda tree structure we described in the previous section where all tree segments are assigned their final lengths when they are created, the lengths of previously created segments in a ternary tree are increased by a constant factor when new segments are created in each growth step. The following is an input to L-systems to generate a ternary tree.

```
#define maxgen 6


#define d1 100.00+rand(40) /* divergence angle */

#define a  15.0+rand(15)   /* branching angle */

#define lr 1.2    /* average length increase rate */

#define vr 1.2    /* average width increase rate */

#define le 12     /* average initial length */



START :

!(vr*(0.9+0.1*rand(2)))F(20*(0.9+0.1*rand(2)))/(180+rand(180))A


p1 : A   ->

!(vr*(0.9+0.1*rand(2)))[&(a)F(le*(0.9+0.1*rand(2)))A]

/(d1)[&(a)F(le*(0.9+0.1*rand(2)))A]
```

```
/(d1)[&(a)F(le*(0.9+0.1*rand(2)))A]

p2 : F(l) -> F(l*lr*(0.9+0.1*rand(2)))

p3 : !(w) -> !(w*vr*(0.9+0.1*rand(2)))
```

Here, we again utilize stochastic L-systems to introduce variations among trees of the same type. The function `rand(2)` is a random number generator which returns a number between 0 and 2 with a uniform probability distribution. Thus, the expression `0.9+0.1*rand(2)` returns a uniformly distributed random number between 0.9 and 1.1 with a mean value of 1.

The production rule `p1` defines the overall structure. Apex `A` produces three new branches terminated by their own apices in each growth step. The relationship between the new branches and the mother branch is specified by changes in length, width, and branching angles. The new branches have a mean length of 12 with the length uniformly distributed between 12×0.9 and 12×1.1, mean width of 1.2 with the width uniformly distributed between 1.2×0.9 and 1.2×1.1. The branching angles have a mean value of 22.5° with a uniform distribution between 15° and 30°. The divergence angle, that is, the angle between two successive branch planes, has a mean value of 120° with a uniform distribution between 100° and 140°. Production rules `p2` and `p3` describe the elongation and thickening of the branches over time; both parameters have an average growth rate of 1.2, uniformly distributed between 1.2×0.9 and 1.2×1.1.

From the above input, ternary trees at different growth stages can be generated (Figures 4-2 and 4-3). Figure 4-2 shows the two-dimensional pictures of stages 2, 3

Stage	Volume (cm^3)	Number of Branches	Height of Trunk (cm)	Radius of Trunk (cm)
2	7.9	15	53	0.18
3	33.4	51	70	0.31
4	131.8	159	88	0.54
5	501.4	483	109	0.94
6	1885.6	1455	132	1.62

Table 4.1: Input parameters for the simulation of the growth of ternary trees.

and 4 of a ternary tree. The two-dimensional pictures of stages 5 and 6 of a ternary tree are displayed in Figure 4-3. Table 4.1 summarizes some of the parameters of a ternary tree generated from L-systems at the five growth stages described above. For each growth stage, the number of branches and the volume they occupy, and the height and radius of the trunk are shown.

The simulated HH, VV, HV backscattering radar cross sections of ternary trees at different growth stages using the growth rule-based model are shown in Figures 4-4 and 4-5. The incident angle is 34°. The dielectric constant of tree branches used in the simulation is 11+i4. Since a stochastic L-system is utilized, ternary trees used to calculate the scattering returns are not identical in each realization of the Monte Carlo approach. Figure 4-4 depicts the results at L-band frequency (1.5 GHz). The backscattering radar cross section is calculated at growth stages 2 to 6. The

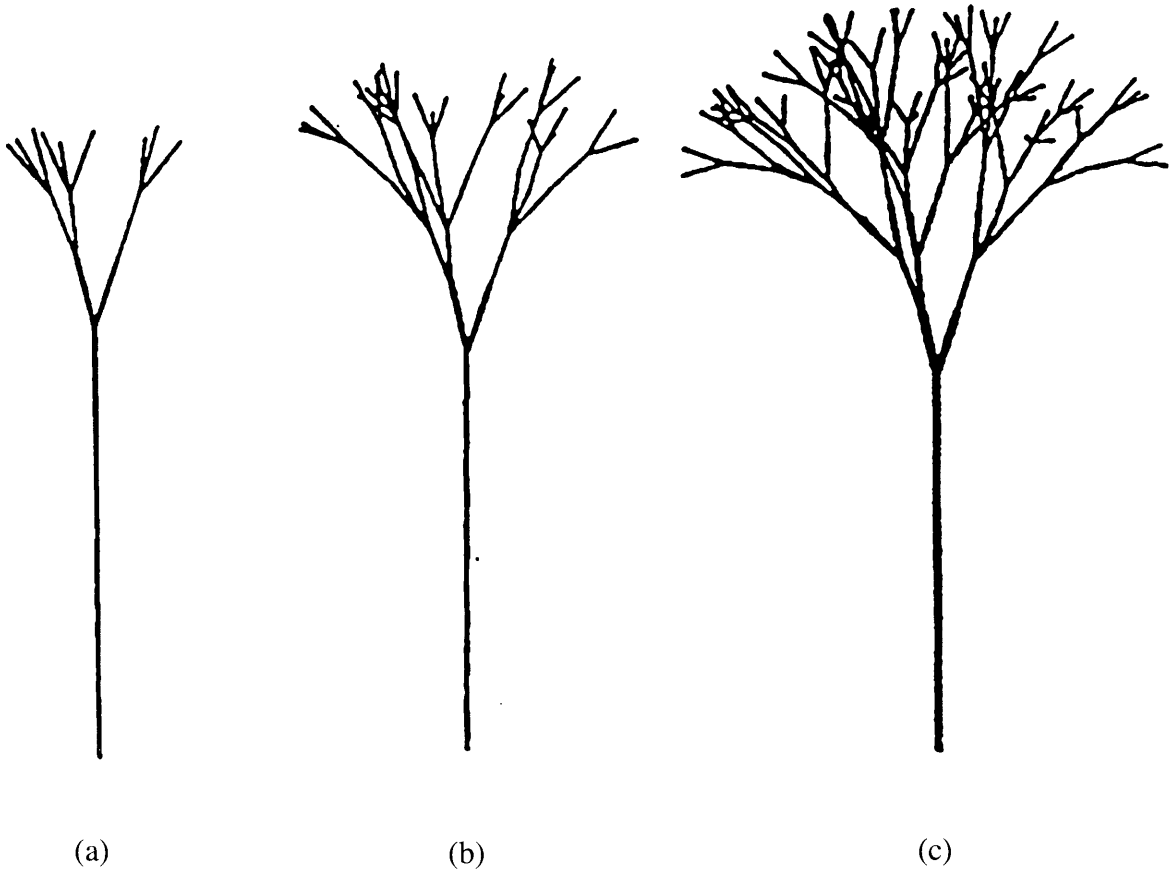

(a) (b) (c)

Figure 4-2: Growth of a ternary tree generated with L-systems: (a) second stage, (b) third stage, (c) fourth stage.

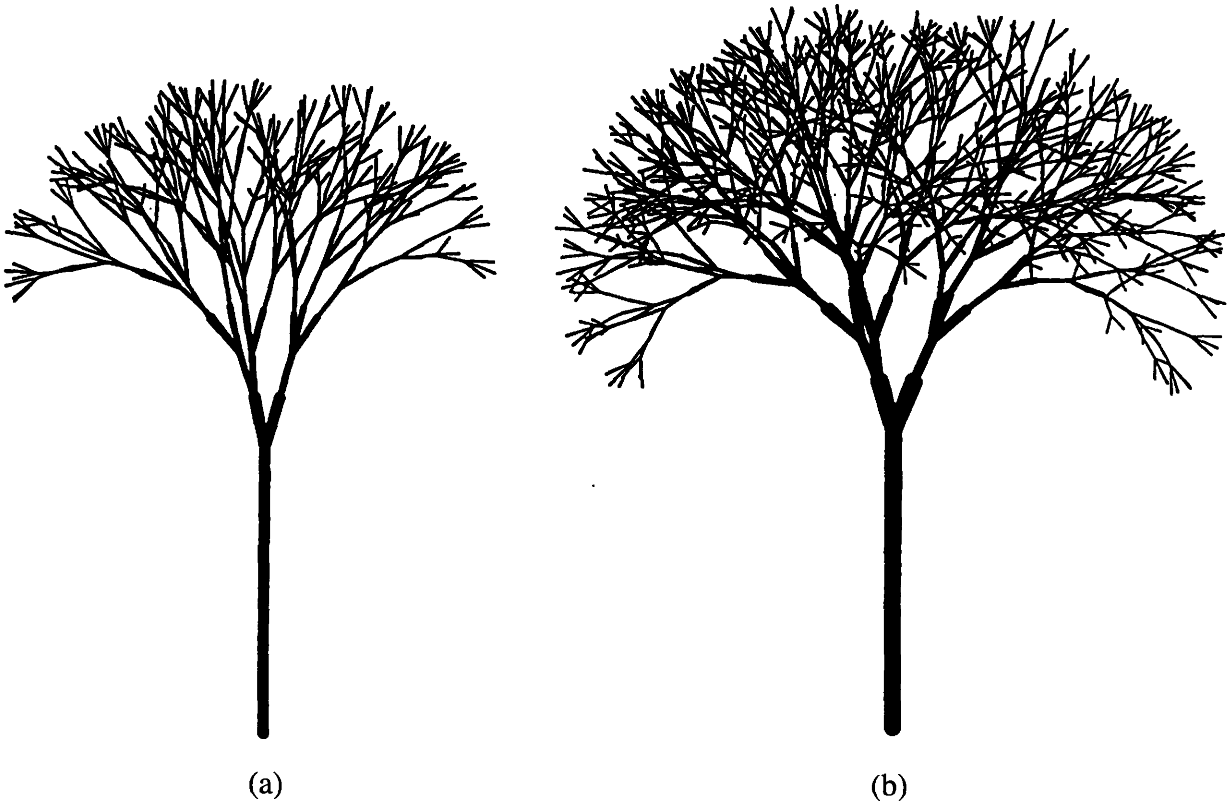

Figure 4-3: Growth of a ternary tree generated with L-systems: (a) fifth stage, (b) sixth stage.

curves rise sharply in the lower growth stages and then reach a plateau. This is expected since new branches are larger at the initial growth stages than those at later stages. Initially, the return with VV polarization is higher than the return with HH polarization. However, after growth stage 5, the HH return is larger than the VV return. This is a consequence of the fact that the large branches contribute the most to scattering at L-band, and the fact that the orientations of large branches become more horizontal at higher growth stages.

The backscattering radar cross section at C-band frequency (5.3 GHz) versus the total volume of branches is shown in Figure 4-5. Like the curves in the case of L-band, there is a large increase in the C-band scattering returns at lower growth stages, and the rate of increase becomes smaller when the trees grow older. However, for C-band, the return with VV polarization is always higher than the return with HH polarization because small branches contribute more toward scattering at C-band, and the small branches tend to be more vertical than horizontal.

4.3 Application to Different Types of Trees

With L-systems, trees with different structure can be simulated. In this section, the concept of "structure factor" which extracts the structural information of a tree and gives the spatial distribution of branches will be defined. The structure factors are then calculated for three different kinds of trees generated using L-systems.

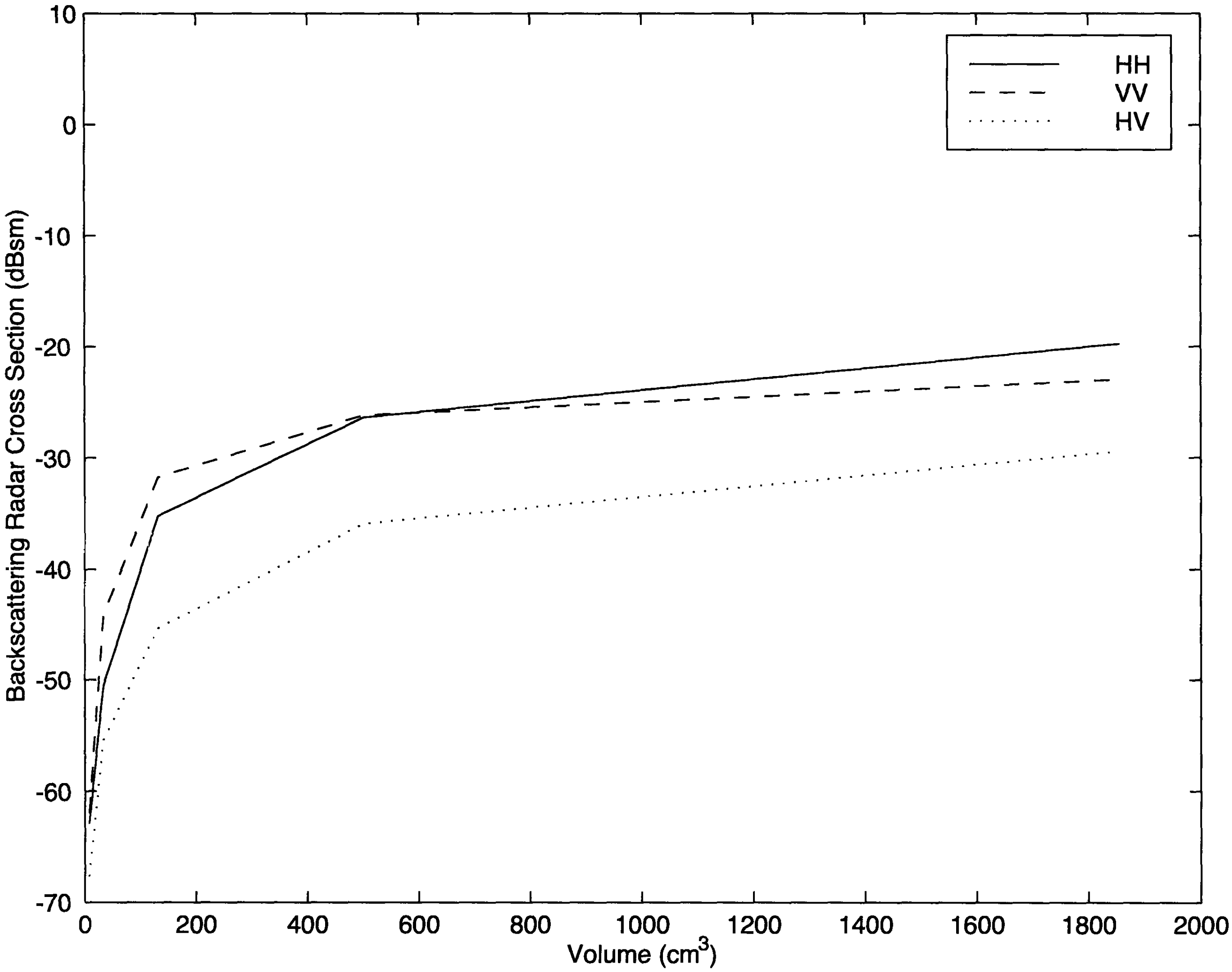

Figure 4-4: L-Band HH, VV, HV backscattering radar cross sections of ternary trees at different growth stages. The incident angle is 34°.

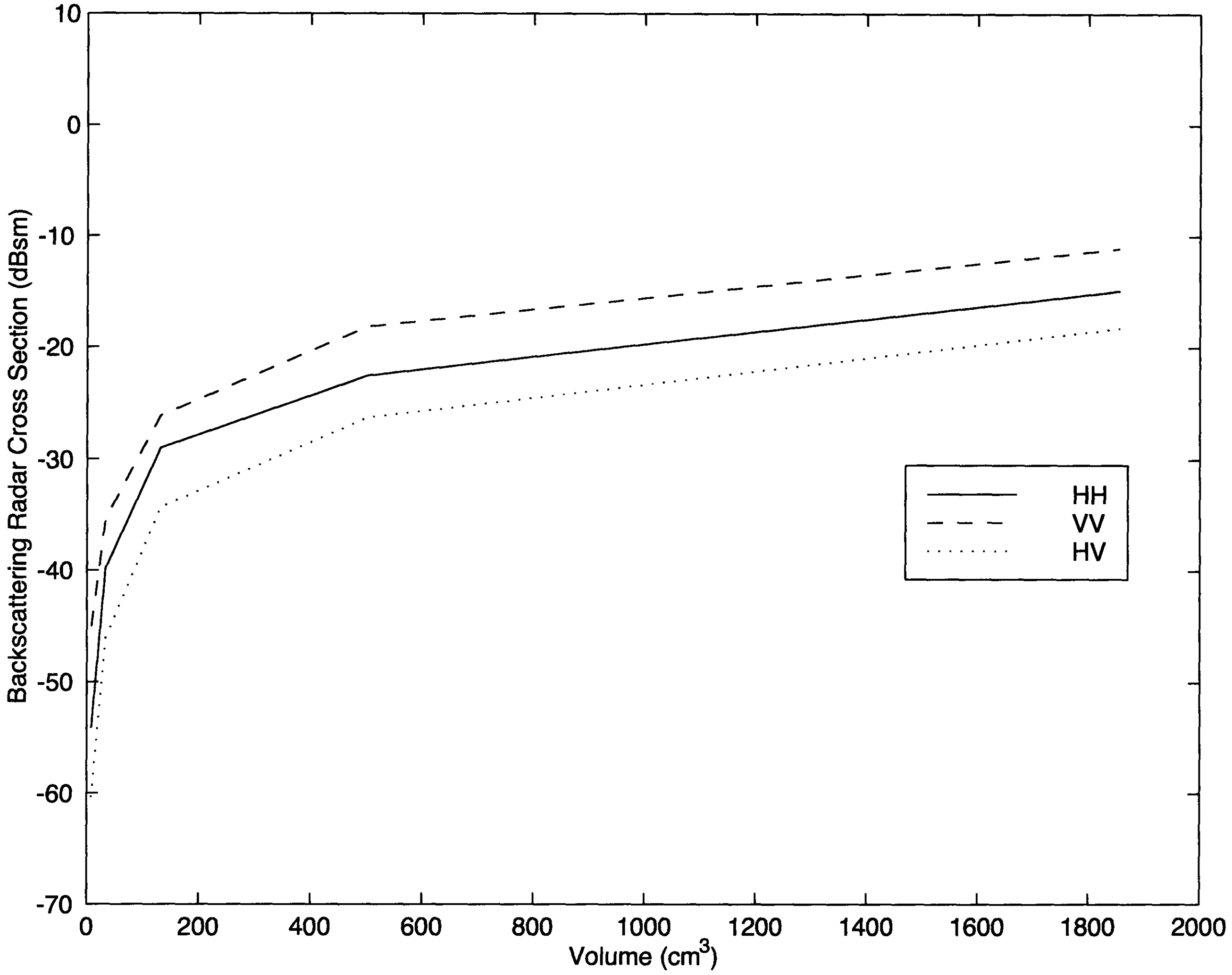

Figure 4-5: C-Band HH, VV, HV backscattering radar cross sections of ternary trees at different growth stages. The incident angle is 34°.

4.3.1 Structural Factor

To examine the scattering returns from trees with different structures, it is useful to define a quantity which extracts the structural information of a tree and gives the spatial distribution of its branches. The structural factor is defined as

$$S = \frac{I_{\text{incoh}}}{I_{\text{ind}}} \tag{4.5}$$

where I_{incoh} and I_{ind} are the powers of incoherent scattering and independent scattering, respectively. The structural factor is related to the pair distribution function which is used to describe the correlation of branch positions. To see how they are related, let's define the scattered field to be

$$F = \sum_{\ell=1}^{N} f_\ell e^{i(\bar{k}_i - \bar{k}_s)\cdot\bar{r}_\ell} \tag{4.6}$$

where N is the number of scatterers, $\bar{r}_\ell$ is the location of the ℓth scatterer, and $\bar{k}_i$ and $\bar{k}_s$ are the propagation vectors of the incident field and scattered field, respectively. The power of independent scattering which does not take the phase interaction between branches into consideration is

$$I_{\text{ind}} = \left\langle \sum_{\ell=1}^{N} |f_\ell|^2 \right\rangle \tag{4.7}$$

which is an average over many realizations of the tree. The average power is the sum of the independent scattering power plus the cross terms.

$$\begin{aligned} \left\langle |F|^2 \right\rangle &= \langle F\, F^* \rangle \\ &= \left\langle \sum_{\ell=1}^{N} \sum_{m=1}^{N} f_\ell f_m^* e^{i(\bar{k}_i - \bar{k}_s)\cdot(\bar{r}_\ell - \bar{r}_m)} \right\rangle \end{aligned}$$

$$= \left\langle \sum_{\ell=1}^{N} |f_\ell|^2 + \sum\sum_{\ell \neq m} f_\ell f_m^* e^{i(\bar{k}_i - \bar{k}_s)\cdot(\bar{r}_\ell - \bar{r}_m)} \right\rangle$$

$$= \left\langle \sum_{\ell=1}^{N} |f_\ell|^2 \right\rangle + \sum\sum_{\ell \neq m} \left\langle f_\ell f_m^* e^{i(\bar{k}_i - \bar{k}_s)\cdot(\bar{r}_\ell - \bar{r}_m)} \right\rangle \tag{4.8}$$

The power of coherent field is

$$\begin{aligned} |\langle F \rangle|^2 &= \langle F \rangle \langle F \rangle^* \\ &= \sum_{\ell=1}^{N}\sum_{m=1}^{N} \left\langle f_\ell e^{i(\bar{k}_i - \bar{k}_s)\cdot\bar{r}_\ell} \right\rangle \left\langle f_m^* e^{i(\bar{k}_i - \bar{k}_s)\cdot\bar{r}_m} \right\rangle \end{aligned} \tag{4.9}$$

We can then calculate the power of incoherent scattering from the average power and power of coherent field.

$$I_{\text{incoh}} = \left\langle |F|^2 \right\rangle - |\langle F \rangle|^2 \tag{4.10}$$

Therefore, the structural factor can be derived from Equations 4.5, 4.7, 4.8, 4.9, and 4.10.

$$\begin{aligned} S &= 1 + \frac{\sum\sum_{\ell \neq m} \left\langle f_\ell f_m^* e^{i(\bar{k}_i - \bar{k}_s)\cdot(\bar{r}_\ell - \bar{r}_m)} \right\rangle - \sum_{\ell=1}^{N}\sum_{m=1}^{N} \left\langle f_\ell e^{i(\bar{k}_i - \bar{k}_s)\cdot\bar{r}_\ell} \right\rangle \left\langle f_m^* e^{i(\bar{k}_i - \bar{k}_s)\cdot\bar{r}_m} \right\rangle}{\sum_{\ell=1}^{N} \left\langle |f_\ell|^2 \right\rangle} \\ &= 1 + \frac{\sum_{\alpha=1}^{L}\sum_{\beta=1}^{L} n_\alpha n_\beta f_\alpha f_\beta^* \int g_{\alpha\beta}(\bar{r}) e^{i(\bar{k}_i - \bar{k}_s)\cdot\bar{r}}\, d\bar{r} - \sum_{\alpha=1}^{L}\sum_{\beta=1}^{L} n_\alpha n_\beta f_\alpha f_\beta^* \int e^{i(\bar{k}_i - \bar{k}_s)\cdot\bar{r}}\, d\bar{r}}{\sum_{\alpha=1}^{L} n_\alpha |f_\alpha|^2} \\ &= 1 + \frac{\sum_{\alpha=1}^{L}\sum_{\beta=1}^{L} n_\alpha n_\beta f_\alpha f_\beta^* \int [g_{\alpha\beta}(\bar{r}) - 1] e^{i(\bar{k}_i - \bar{k}_s)\cdot\bar{r}}\, d\bar{r}}{\sum_{\alpha=1}^{L} n_\alpha |f_\alpha|^2} \end{aligned} \tag{4.11}$$

where α and β are indices of size categories, n_α and n_β are the number densities of α and β size categories, respectively, and $g_{\alpha\beta}(\bar{r})$ is the pair distribution function. A size category consists of branches of size within a specific range. Equation 4.11 is the expression for the structure factor which is a function of the wavenumber k. It is the Fourier transform of the pair distribution function.

4.3.2 Simulation Results

Three different kinds of trees are generated using L-systems. The first kind is based on the growth rule proposed by Honda (Figure 4-1). The Honda tree input to the L-systems is discussed in Section 1. The second kind is a ternary tree discussed in Section 2 and shown in Figure 4-6. The third kind is a binary tree which has a simple structure with one big stem and a binary branching pattern. The following is the input to L-systems to generate a binary tree.

```
#define maxgen 5

#define d1 160+rand(40)       /* divergence angle */
#define a0 40+rand(10)        /* branching angle */
#define lm 0.04*(9+rand(2))   /* stem length */
#define wm 0.01*(9+rand(2))   /* stem width */
#define lb 0.04*(9+rand(2))   /* branch length */
#define wb 0.004*(9+rand(2)) /* branch width */

START : !(wm)F(lm)/(180+rand(180))A
```

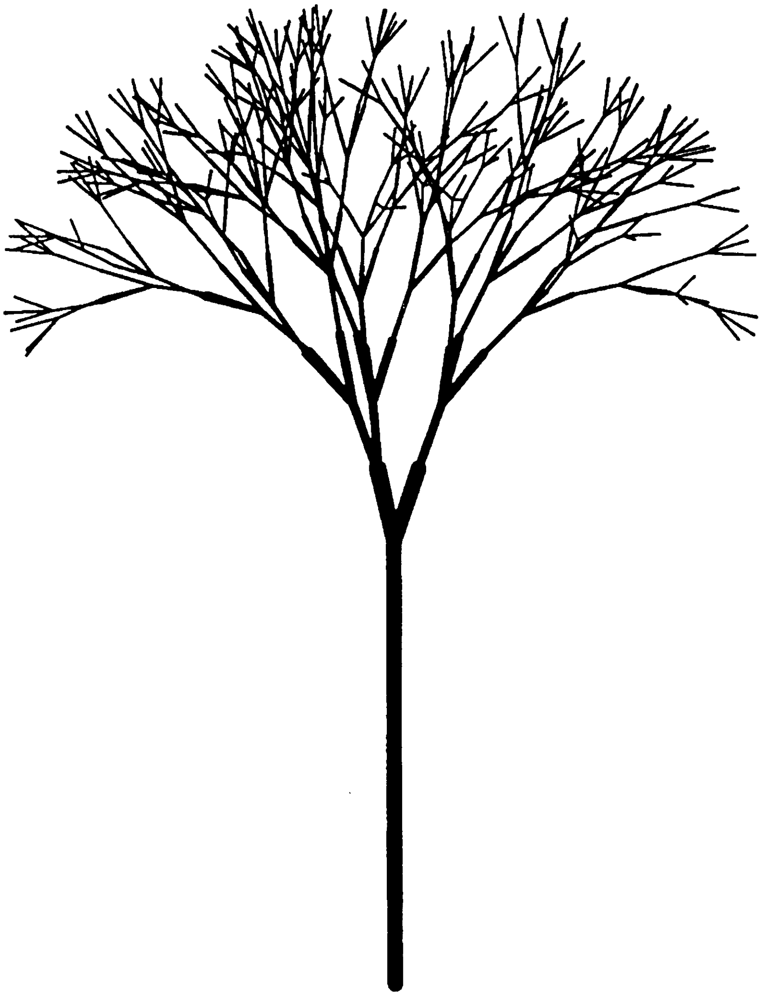

Figure 4-6: A tree with a ternary branching structure generated using L-systems at the fifth growth stage.

```
pl : A ->
[&(a0)!(wb)F(lb)]
/(d1)[&(a0)!(wb)F(lb)]
/(d1)!(wm)F(lm)A
```

Like the inputs for the Honda and ternary trees, stochastic L-systems are utilized to provide variations among trees of the same type. The random number generator `rand(n)` returns a number between 0 and n with uniform probability density distribution. The overall structure of the tree is defined by the production rule `p1`. In each growth step, apex `A` produces two new branches and the main stem. The new branches have a mean length of 0.4 with the length uniformly distributed between 0.4×0.9 and 0.4×1.1, mean width of 0.04 with the width uniformly distributed between 0.04×0.9 and 0.04×1.1. The branching angle is uniformly distributed between 40° and 50° with a mean of 45°. The growth part of the trunk has a mean length of 0.4 with the length uniformly distributed between 0.4×0.9 and 0.4×1.1, and mean width of 0.01 with the width uniformly distributed between 0.01×0.9 and 0.01×1.1. The divergence angle is uniformly distributed between 160° and 200° with a mean of 180°. A two-dimensional picture of the generated binary tree is depicted in Figure 4-7.

Using L-systems and the Monte Carlo approach, the structural factors at approximately the same tree trunk height are calculated as a function of frequency. In our simulation, Honda trees are at the ninth growth stage, and ternary trees and binary

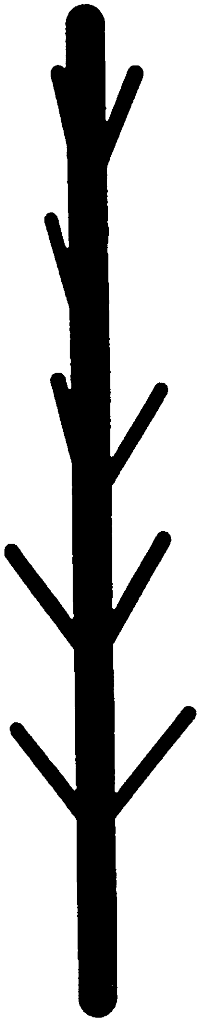

Figure 4-7: A tree with a binary branching structure generated using L-systems at the fifth growth stage.

trees are at the fifth growth stage. The incident angle is 45°. The dielectric constant of tree branches is 11+i4. Figures 4-8, 4-9 and 4-10 display graphs of the structure factor as a function of frequency with the center frequency at L-band (1.5 GHz) for HH, VV, and HV polarizations, respectively. The frequency varies from 1.25 GHz to 1.75 GHz. As shown in the figures, the structure factors are very different for these three kinds of trees for all polarizations. The shapes of the curves are formed as the result of interference between branches. Since the binary tree has a simpler structure, the curve of the structure factor is also simpler.

The structure factor can also be calculated as a function of frequency with the center frequency at C-band (5.3 GHz). Since we expect less difference in the shapes of structure factor curves between trees with different structures at C-band than at L-band, we will concentrate on Honda and ternary trees for this case. Figures 4-11, 4-12 and 4-13 show the graphs of the structure factor versus frequency for HH, VV, and HV polarizations, respectively. The frequency varies from 5.06 GHz to 5.56 GHz. These plots confirm our prediction that there is less difference in the structure factor curves at C-band because the small branches contribute the most to scattering at C-band, and have similar orientations for most trees.

4.4 Summary

In this chapter, the fundamentals of L-systems are introduced. Using L-systems, we are able to capture the architecture of trees and describe their growth. The stochastic

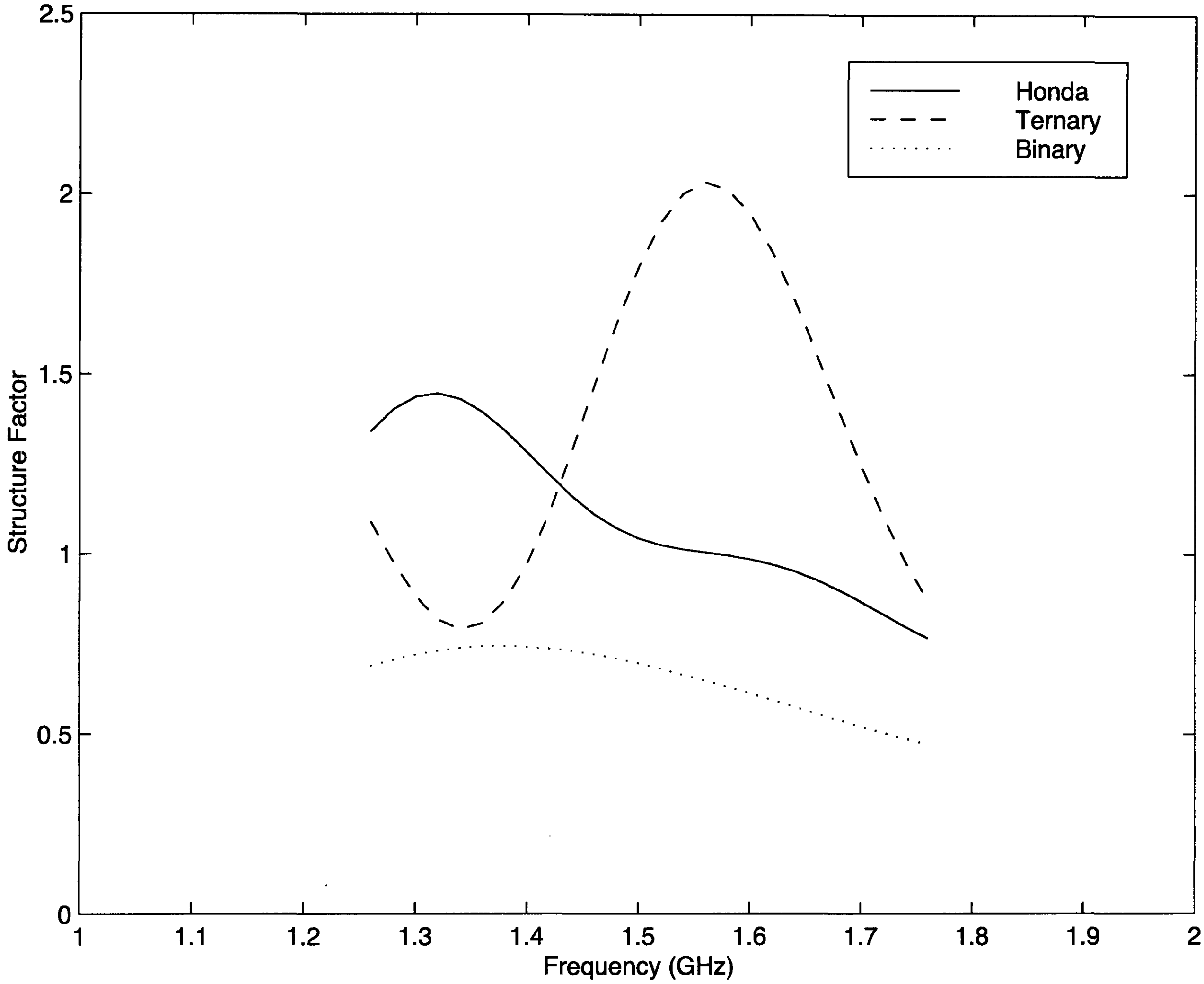

Figure 4-8: L-Band structure factor for HH polarization as a function of frequency for trees with different structures

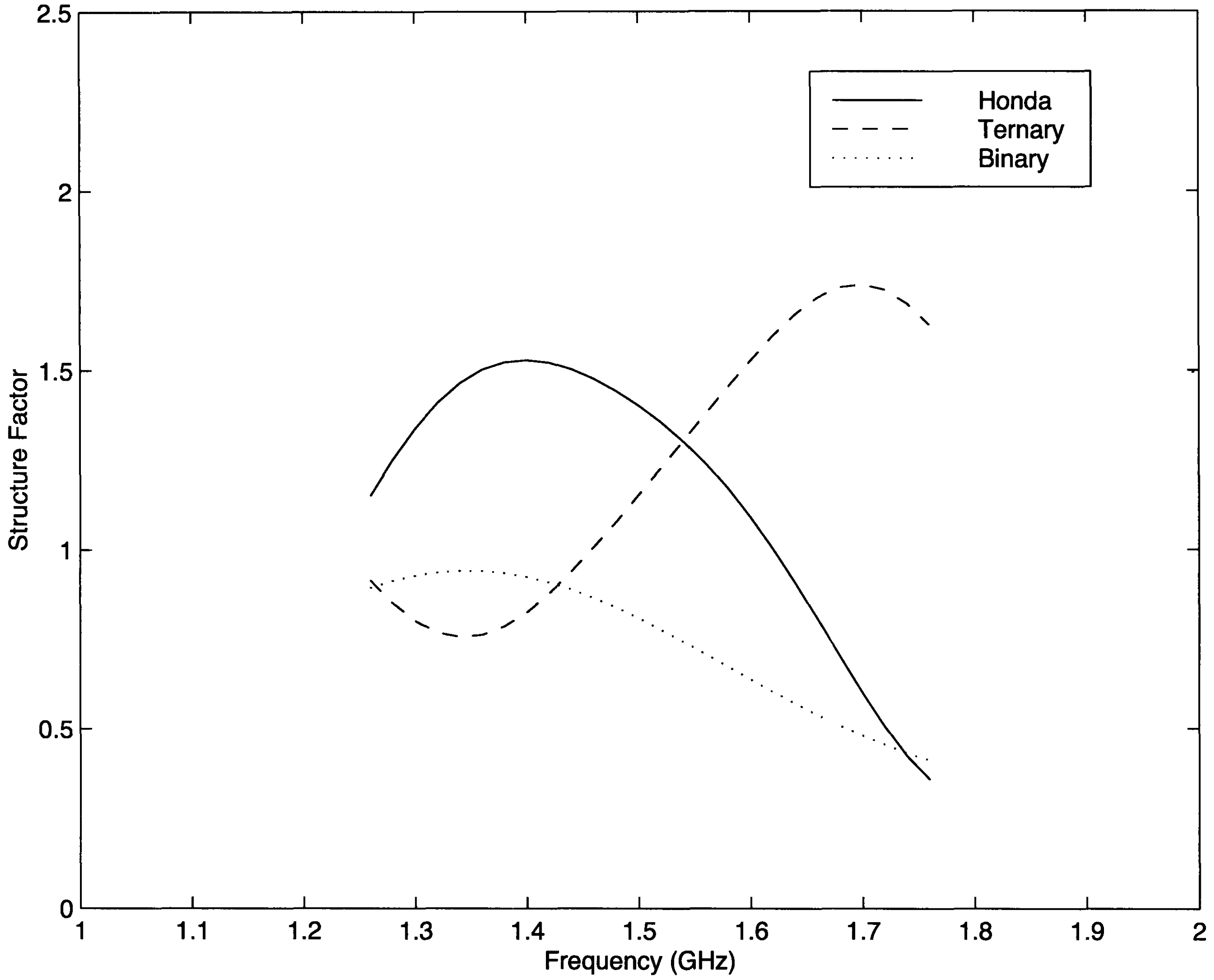

Figure 4-9: L-Band structure factor for VV polarization as a function of frequency for trees with different structures

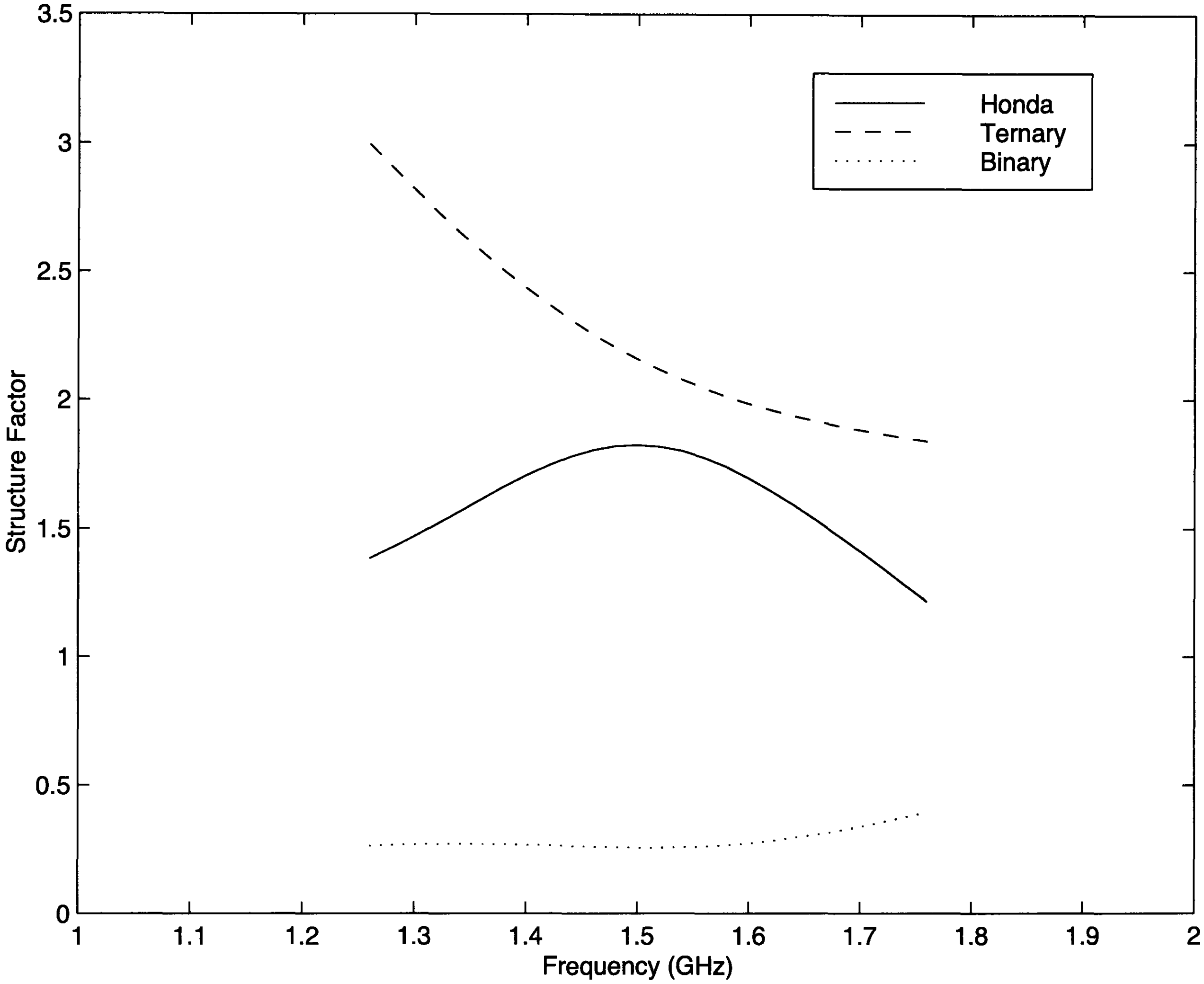

Figure 4-10: L-Band structure factor for HV polarization as a function of frequency for trees with different structures

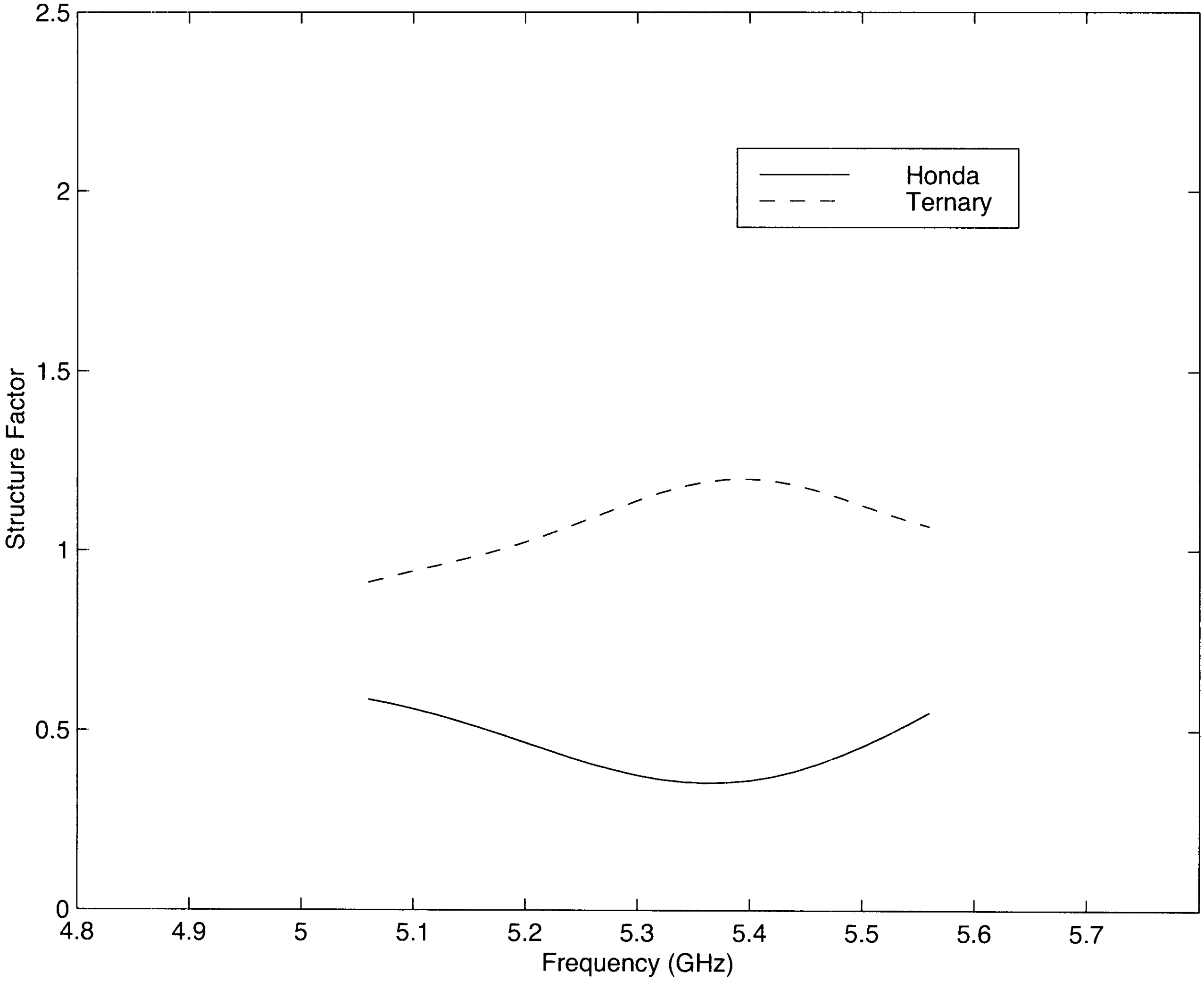

Figure 4-11: C-Band structure factor for HH polarization as a function of frequency for trees with different structures

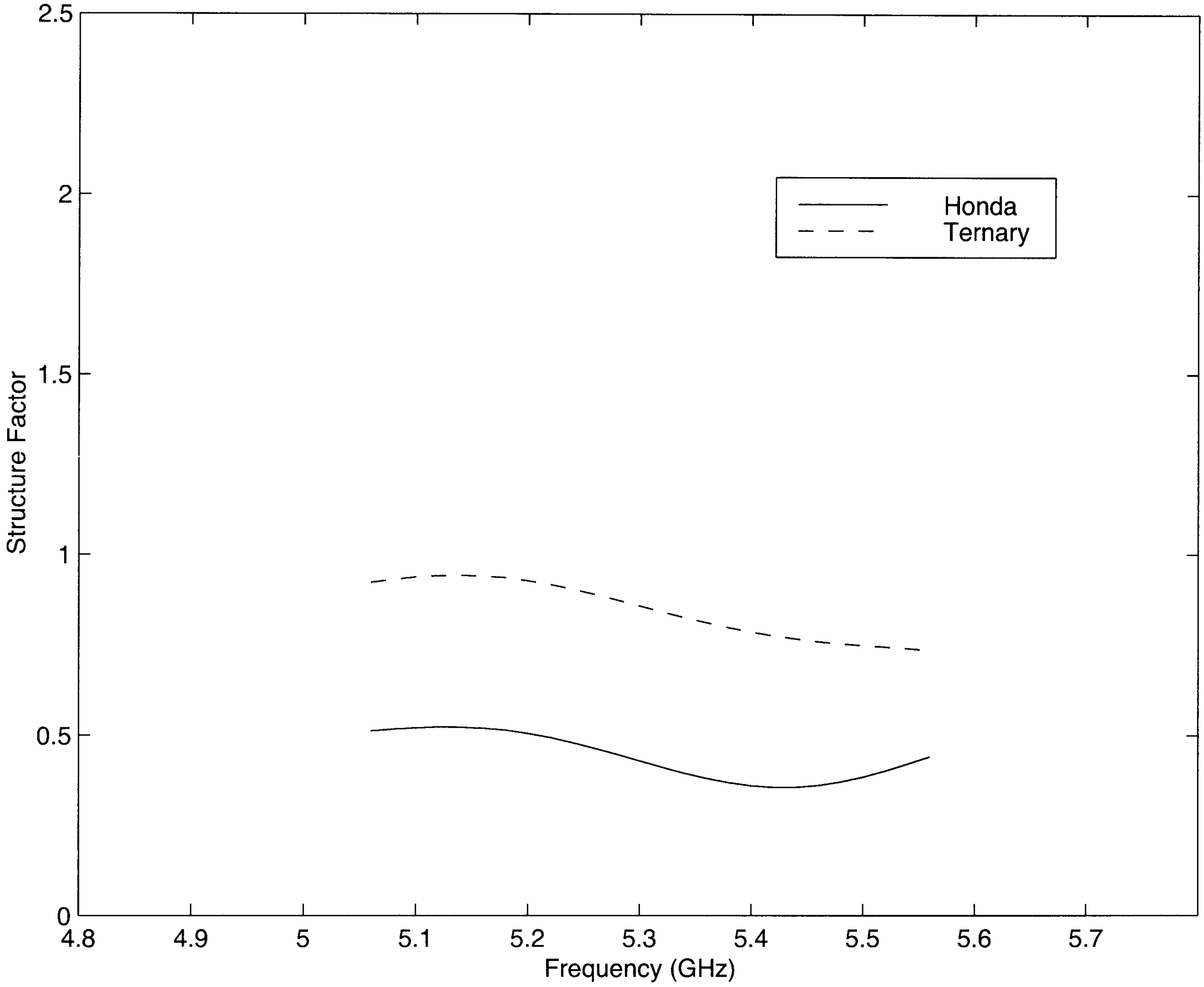

Figure 4-12: C-Band structure factor for VV polarization as a function of frequency for trees with different structures

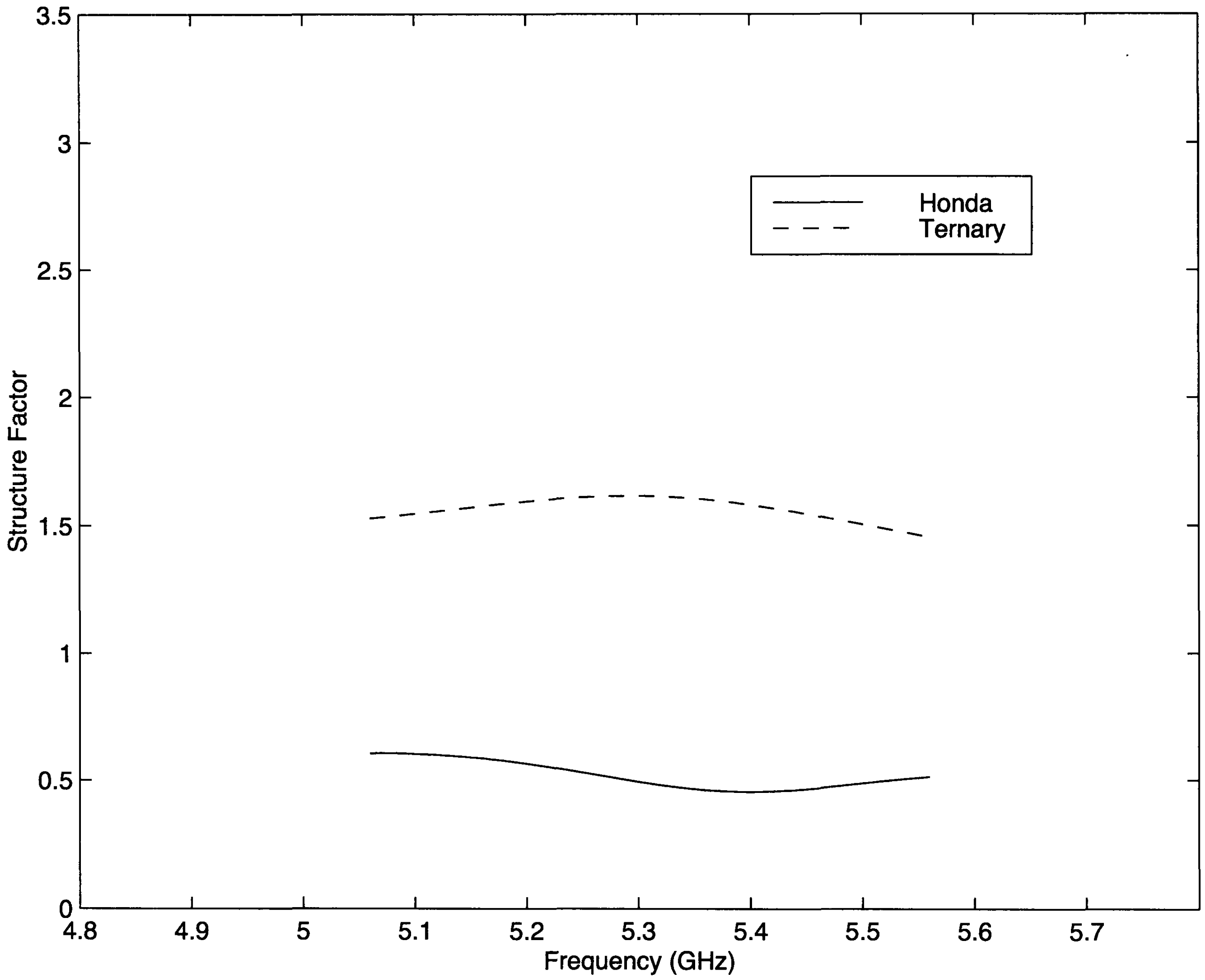

Figure 4-13: C-Band structure factor for HV polarization as a function of frequency for trees with different structures

L-systems are utilized to incorporate random variations among trees of the same type. The output of L-systems contains information on the position, size, and orientation of every branch in the generated tree. From the L-system output, we can calculate the scattering of electromagnetic waves by these architecturally realistic trees using the Monte Carlo approach, which also takes into consideration the coherent interactions among branches. Using this growth rule-based model, the scattered returns from trees of different structures at different growth stages are calculated and analyzed.

Ternary trees are used as an example in our study of scattering from trees at different growth stages. Backscattering radar cross sections for HH, VV ,and HV polarizations are obtained and interpreted for L-band and C-band frequencies. To study the scattering results from trees with different structures, we defined and calculated the structure factor which extracts the structural information of a tree and gives the spatial distribution of branches. Structure factors for HH, VV, and HV polarizations of trees with different structures are obtained for L-band and C-band frequencies. The results show larger variation in structure factors among different types of trees at L-band as compared to C-band. This result is consistent with our prediction.

Chapter 5

Retrieval of Geophysical Parameters Using Neural Networks

In the previous chapter, we considered a class of problems in which we know the physical characteristics of the scattering objects or medium, and wish to determine the scattering coefficients. We now consider a different class of problems in which the scattering coefficients are known, and we wish to determine the characteristics of the scattering objects or medium from which the measurements are obtained. This problem is referred to as parameter inversion. Inversion of the geophysical information from electromagnetic measurements is an important application of microwave remote sensing. There has been an increasing interest in the applications of neural networks [46] to the classification of terrains and inversion of geophysical parameters in the remote sensing research community. The potential and capability of neural networks for dealing with complex remote sensing data have been demonstrated. For example, the classification of terrain mappings from satellite data using neural networks showed a better classification rate than the conventional statistical approach [8, 21], and a neural network trained with a theoretical scattering model has been applied to the inversion of snow parameters [75]. Neural networks are flexible for the inversion of geophysical parameters especially for multi-dimensional inputs such as multi-frequency polarimetric scattering data. Another advantage is that one does not need to make any assumption about the analytic form of the statistics of the input data.

In the first section of this chapter, an introduction to neural networks is given. In Sections 2, the inversion of soil moisture and surface parameters using neural networks trained with theoretical surface scattering models are described. In Section 3, the description of the inversion of sunflower biomass using neural networks trained with the scattering returns obtained from the developed structural model (discussed in Chapter 3) is given. To assess the performance of the use of experimental data to train the neural networks, the polarimetric radar data acquired by the Spaceborne Imaging Radar-C (SIR-C) over the Landes Forest in France [40] are utilized as the training data to retrieve the forest age (or equivalently, forest biomass). SIR-C data and forest age inversion results are discussed in Section 4.

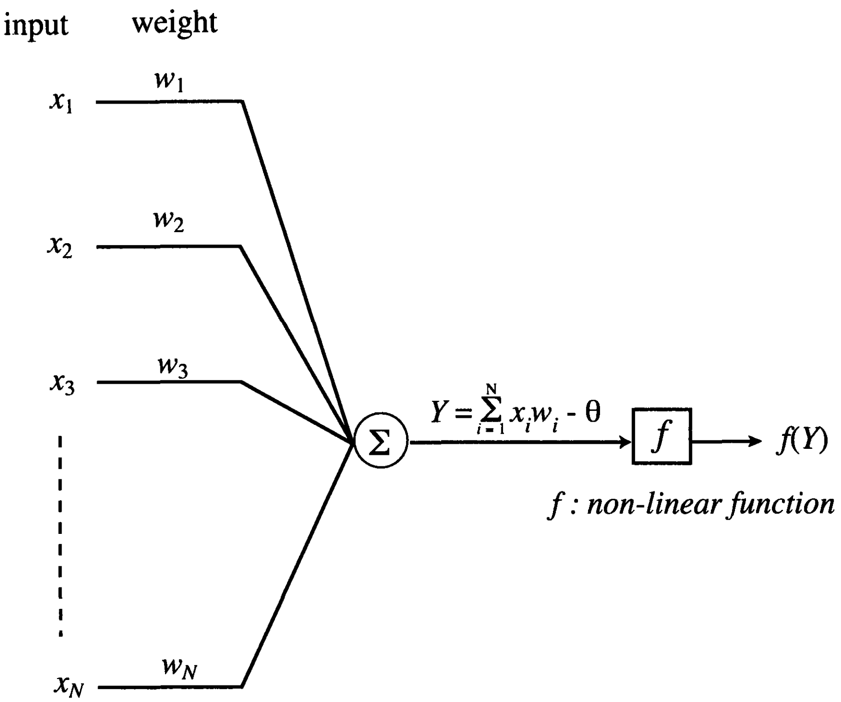

Figure 5-1: A basic building block of the neural network consists of one node and some incoming weights.

5.1 Neural Networks

Neural networks have been studied for many years in the hope to simulate human intelligence. Because of its ability to learn, it can be trained to perform pattern recognition. It is flexible for inversion of geophysical parameters especially for multi-dimensional inputs such as multi-frequency, multi-polarization scattering data.

Neural networks are composed of many nodes which are non-linear computational elements operating in parallel. Each node is designed to simulate the behavior of a single neuron in the biological nervous system. The nodes are connected by weights whose values are adjusted during the neural network training process to improve performance. Neural networks are specified by their node characteristics, net topology, and training rule. Figure 5-1 shows the basic building block of neural networks which consists of one node and some incoming weights. The output of each node can be described by the equation

$$f(Y) = f\left(\sum_{i=1}^{N} x_i w_i - \theta\right) \tag{5.1}$$

where N is the number of inputs, x_i the ith input, w_i the ith weight, θ an offset, and f a non-linear function. The node sums N weighted inputs and passes the result through a non-linear function. Therefore, a node is characterized by the offset and the type of non-linearity. The three commonly used non-linear functions for neural networks include the hard limiter function, the threshold logic element, and the sigmoid function [46]. Figure 5-2 shows the hard limiter function which behaves like a switch since the output changes sign as the input changes sign. The threshold logic element and the sigmoid function are shown in Figures 5-3 and 5-4, respectively. The sigmoid function is a differentiable approximation of the threshold logic element. Since some of the neural network training algorithms require the non-linear function to be continuous and differentiable, the sigmoid function is often used. It can be described by the equation

$$f(Y) = \frac{1}{1 + e^{-Y}} \tag{5.2}$$

The functions of neural networks can vary significantly depending on how the nodes are connected. The often used neural network architectures include Hopfield

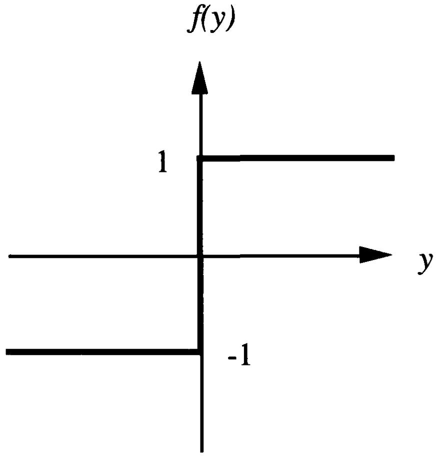

Figure 5-2: Hard limiter is one of the commonly used non-linear functions for neural networks. The output changes sign as the input changes sign.

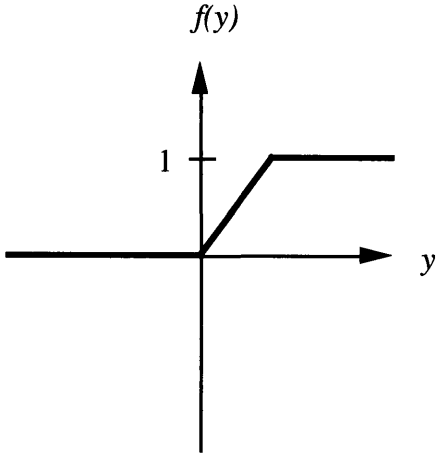

Figure 5-3: The threshold logic element is one of the commonly used non-linear functions for neural networks.

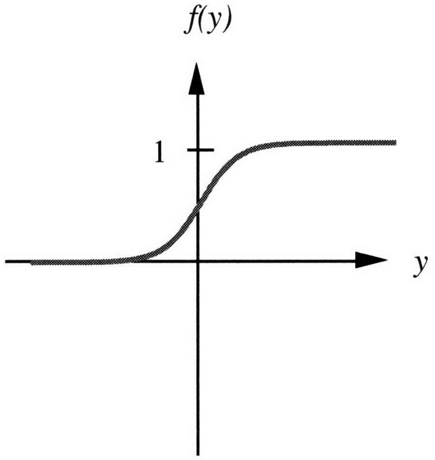

Figure 5-4: The sigmoid function is a differentiable approximation of the threshold logic element.

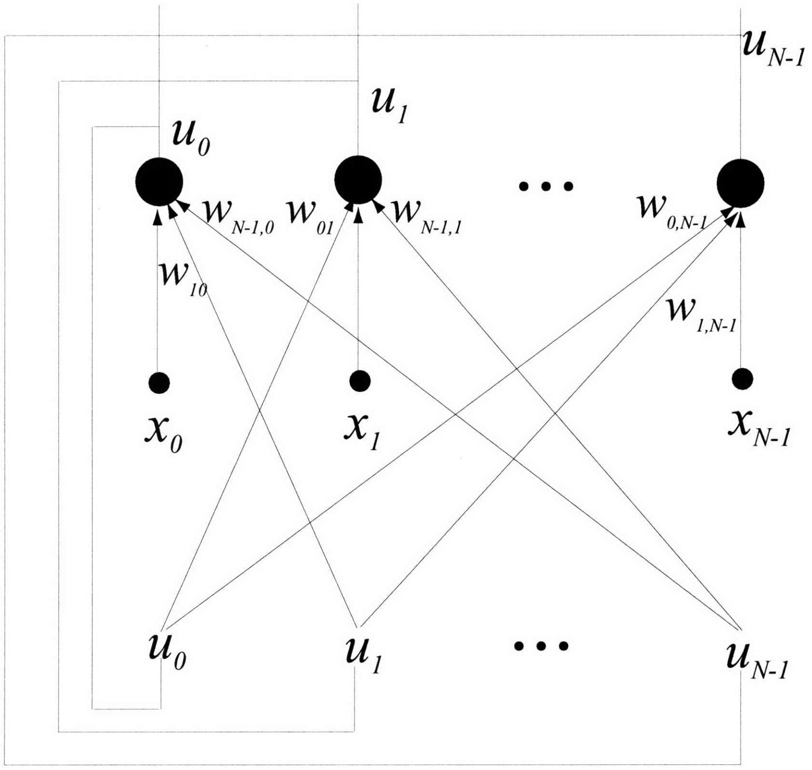

Figure 5-5: Hopfield net.

net [24] and Hamming net [92] for binary inputs, and single-layer perceptron [60] and multi-layer perceptron [46] for continuous valued inputs. The Hopfield net can be used as an associative memory or to solve optimization problems. It contains N nodes with a hard limiter function. All inputs and outputs are binary variables and can take on the values of $+1$ or -1. The output of each node is fed back to all other nodes by connection weights w_{ij}. The first step in the Hopfield algorithm is to assign weights from the exemplar patterns of M number of classes by

$$w_{ij} = (1 - \delta_{ij}) \sum_{k=0}^{M-1} x_i^{(k)} x_j^{(k)}, \quad 0 \leq i, j \leq N-1 \tag{5.3}$$

where δ_{ij} denotes the usual Kronecker function $\delta_{ij} = 1$ if $i = j$, or 0 if $i \neq j$, ω_{ij} is the connection weight from node i to node j, and $x_i^{(k)}$ is element i of the exemplar for class k. The second step is to present the unknown input pattern $\{x_0, x_1, ..., x_{N-1}\}$ to the net. The output of node i at time 0 is initialzed to x_i which is the element i of the unknown input pattern and can be $+1$ or -1.

$$u_i(0) = x_i\,, \quad 0 \leq i \leq N-1 \tag{5.4}$$

After the initialization in the second step, the net itereates in discrete time steps using the following formula until convergence is reached.

$$u_j(t+1) = f_h \left[\sum_{i=0}^{N-1} w_{ij} u_i(t) \right], \quad 0 \leq j \leq N-1 \tag{5.5}$$

where $u_i(t)$ is the output of node i at time t and f_h is the hard limiter function shown in Figure 5-2. When the node outputs remain unchanged with more iterations, the net is considered to have converged. The node outputs represent the exemplar pattern that best matches the unknown input pattern.

Like Hopfield network, the Hamming network is normally used with binary inputs. It is a minimum Hamming distance classifier which calculates the number of bits in the input which do not match the corresponding exemplar bits (Hamming distance) and selects the stored classes that are at a minimum Hamming distance value. The Hamming network architecture contains two subnets. The lower subnet contains N elements in the input and is of the feedforward type. The upper subnet selects the node with the maximum output. It has M output nodes since there are M number of classes. The first step in the operation of the Hamming net is assigning connection weights and offsets from the exemplar patterns of M number of classes. In the lower subnet,

$$w_{ij} = \frac{x_i^{(j)}}{2} \tag{5.6}$$

$$\theta_j = \frac{N}{2} \tag{5.7}$$

$$0 \leq i \leq N-1, \qquad 0 \leq j \leq M-1$$

where w_{ij} is the connection weight from input i to node j, θ_j is the threshold in that node, and $x_i^{(j)}$ is the element i of exemplar j. In the upper subnet,

$$t_{kl} = \begin{cases} 1 & \text{if } k = l \\ -\epsilon & \text{if } k \neq l, \text{and } \epsilon < \frac{1}{M} \end{cases}$$

$$0 \leq k, l \leq M-1$$

where t_{kl} is the connection weight from node k to node l. All thresholds in this subnet are zero. After weights and thresholds have been assigned, a binary unknown input pattern with N elements is presented at the bottom of the Hamming net. The output of node j at time 0 is

$$u_j(0) = f_t\left(\sum_{i=0}^{N-1} w_{ij}x_i - \theta_j\right)$$

$$0 \leq j \leq M-1$$

where x_i is the element i of the unknown input pattern and f_t is the threshold logic element shown in Figure 5-3. After the initialization, the upper subnet then iterates in time using

$$u_j(t+1) = f_t\left(u_j(t) - \epsilon\sum_{k\neq j} u_k(t)\right)$$

$$0 \leq j,k \leq M-1$$

The process is repeated until convergence is achieved, after which the output of only one node remains positive. The selected class corresponds to the node with a positive output.

Among the neural network architectures, the multi-layer perceptron is the most widely used neural network architecture at present. It has the ability to learn a mapping of any complexity. Therefore, it can be used for a wide variety of applications although it may require a lengthy training with many iterations. Multi-layer perceptron is a feed-forward network, and has one or more layers of nodes between the input and output layers. Figure 5-6 shows a three-layer perceptron which contains two hidden layers between the input and output layers. The number of nodes in the hidden layers does not have to be the same.

Although multi-layer perceptron has been known for more than a quarter of a century, the lack of effective training algorithms has prevented its successful applica-

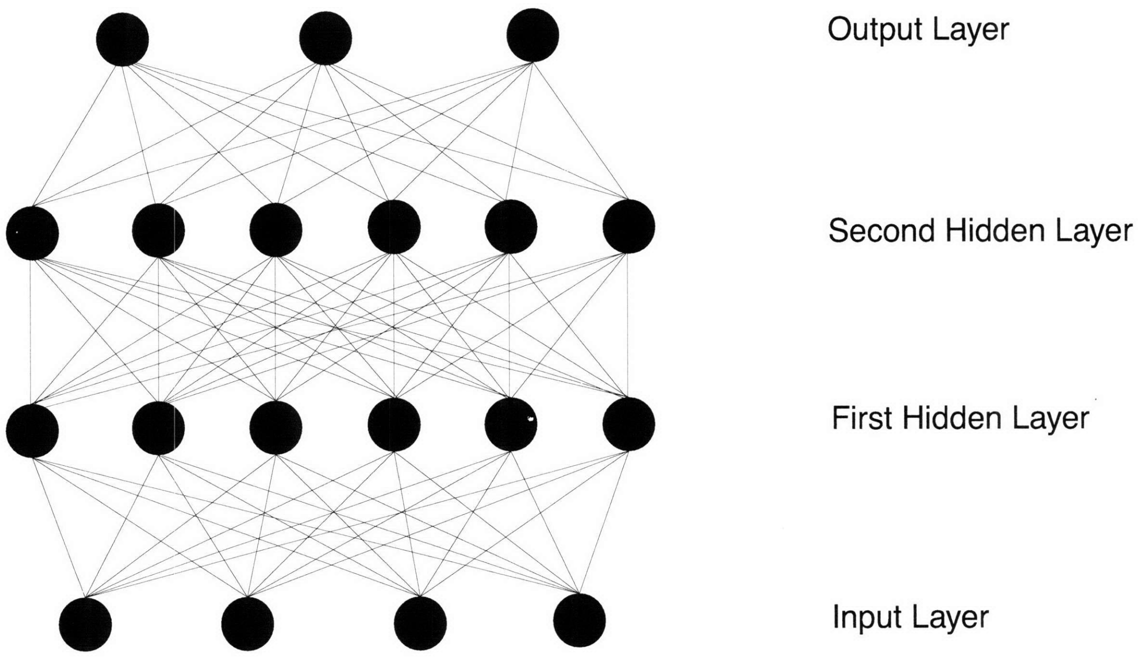

Figure 5-6: A three-layer perceptron contains two hidden layers of nodes between the input and output layers.

tions to practical tasks. The development of the back-propagation training algorithm [63] has led to the widespread and successful present use of multi-layer perceptron. Back-propagation algorithm is a generalization of the least-mean-square algorithm. It uses the gradient search technique to minimize the mean square difference between the desired and actual net outputs. It is called "back-propagation" because during training, the output errors can be propagated into hidden layers such that the error information passes backward. This backward error transmission mechanism is used to adapt the weights. It requires a continuous differentiable non-linear function such as the sigmoid function. The training procedure using the back-propagation algorithm is shown in Figure 5-7. The first step in the training procedure is to initialize weights and offsets to be trained at small random values. The second step is to present an input vector $\{x_1, x_2, ..., x_N\}$ and the corresponding desired outputs $\{d_1, d_2, ..., d_M\}$ to the network. Given the presented inputs, the number of nodes in each layer, and the weights and the offset associated with each node, the actual outputs $\{y_1, y_2, ..., y_M\}$ are calculated using equations 5.1 and 5.2 in the third step of the training procedure. The fourth step is to adapt weights to reduce the output error. The weights are adjusted according to the following equation

$$w_{ij}(t+1) = w_{ij}(t) + \eta \delta_j x_i^{'} \tag{5.8}$$

where $w_{ij}(t)$ is the weight from an input or hidden node i to node j at time t, $x_i^{'}$ is either the output of node i or is an input, η is a learning gain term, and δ_j is an error term for node j. The error term δ_j must be determined in the output layer first, and then it is propagated toward the network input nodes. If the node j is an output

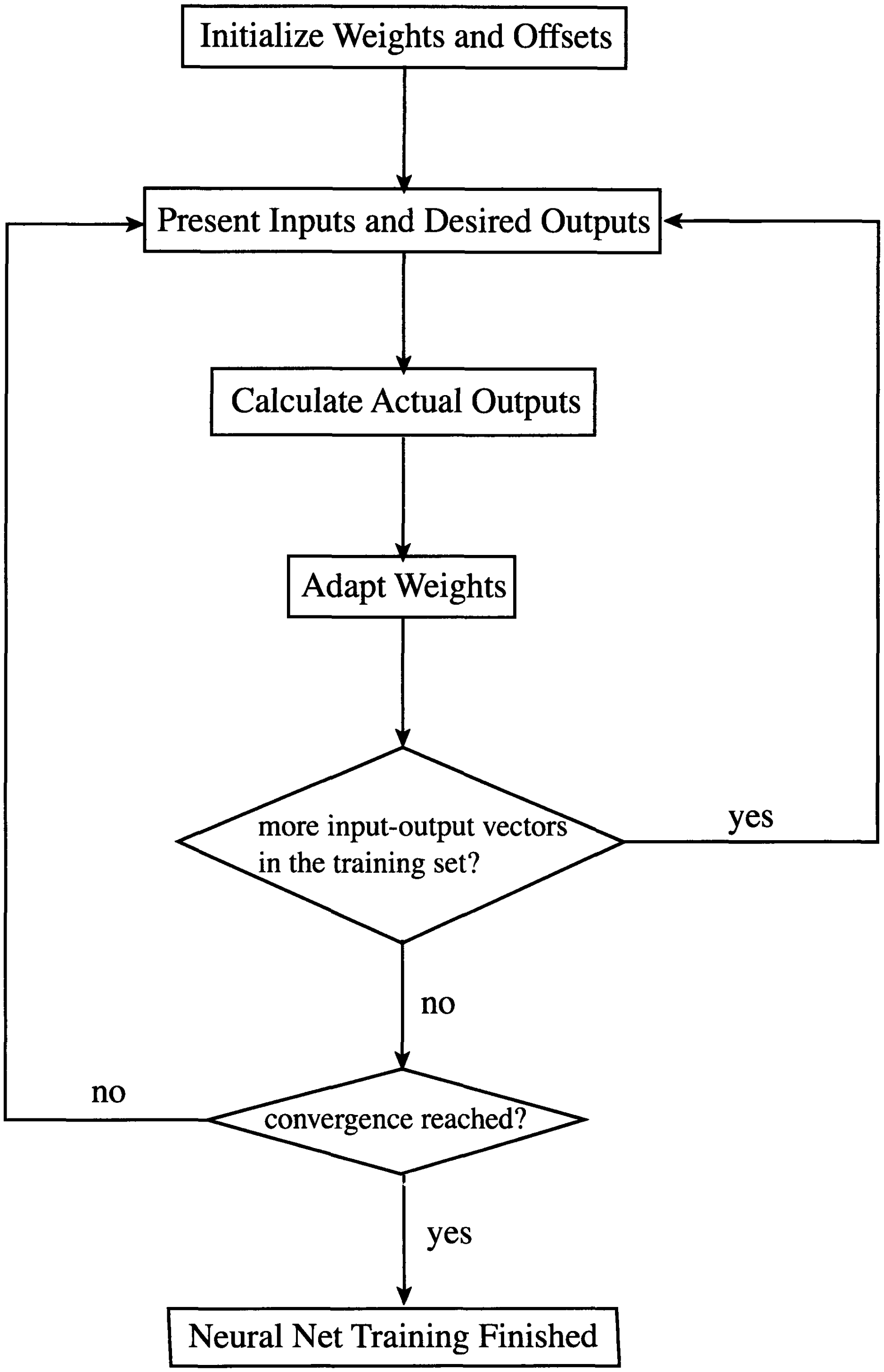

Figure 5-7: Flow chart of the back-propagation training algorithm

node,

$$\delta_j = y_j(1 - y_j)(d_j - y_j) \tag{5.9}$$

where d_j is the desired output of node j, and y_j is the actual output. If node j is an internal hidden node,

$$\delta_j = x_j'(1 - x_j')\sum_k \delta_k w_{jk} \tag{5.10}$$

The summation in equation 5.10 is performed over all nodes in the layers above node j. The speed of convergence can be improved if a momentum term α is included in equation 5.8. The modified weight equation becomes

$$w_{ij}(t+1) = w_{ij}(t) + \eta\delta_j x_i' + \alpha(w_{ij}(t) - w_{ij}(t-1)) \tag{5.11}$$

where $0 < \alpha < 1$. The momentum term helps prevent oscillation during the training phase.

The above steps complete a single learning process based on an input vector and its corresponding desired outputs from the training set. Subsequently, the next input vector in the training set is presented and Steps 2 to 4 described above are repeated. The training steps proceed until all input vectors in the training sets are exhausted. This terminates the complete training cycle. The process is then repeated for the entire training set until convergence in the output error is reached. Since the back-propagation training algorithm uses the gradient search technique, it may converge to a local minimum instead of the desired global minimum. These can be avoided by starting the training from different initial weight values. After the training is completed, the weights in the neural net which produces the best result are obtained.

When we apply an input to the trained neural net, the outputs can be computed immediately on the basis of the weights obtained.

5.2 Retrieval of Soil Moisture and Surface Parameters

Retrieval of soil moisture information from remote sensing data has been a subject of great interest for the past two decades [59, 80]. To perform the inversion, the soil surface roughness parameters are needed because the radar backscattering coefficient has a strong dependence on the variations of the parameters characterizing the surface roughness. Unfortunately, ground truth measurements usually have large uncertainties due to the spatial variation of the surface roughness. Additional information (e.g. from multiple frequencies) will be helpful in reducing the influence of surface roughness on the soil moisture inversion. In subsequent sections, we will utilize neural networks for the inversion of soil parameters, and analyze the inversion results obtained using different combinations of backscattering data as inputs to the neural networks.

5.2.1 Approach for the Inversion

There are two major steps in the approach to retrieve soil moisture and surface parameters using neural networks (Figure 5-8). First, the neural network needs to be trained before inversion can be performed. The training data include the polari-

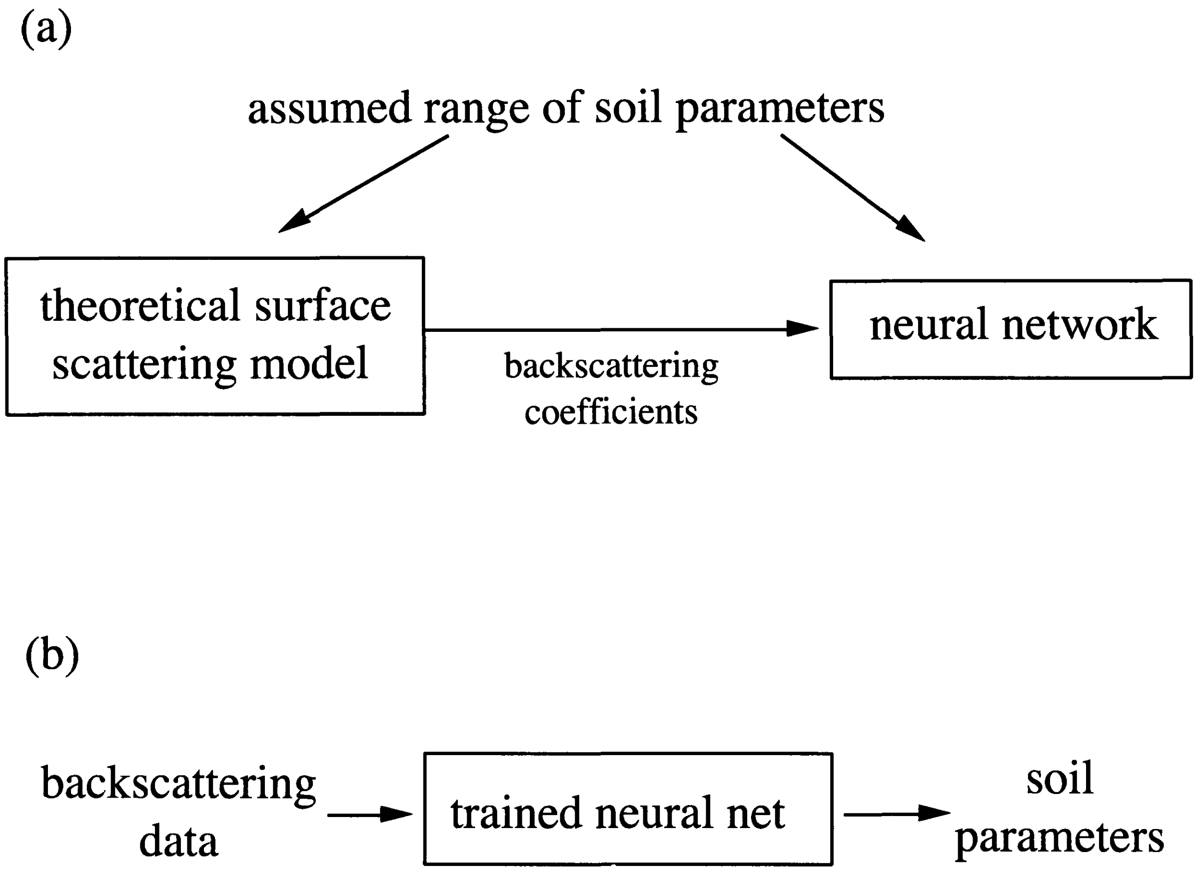

Figure 5-8: Two major steps in the retrieval of soil moisture and surface parameters using neural networks: (a) training and (b) inversion.

metric backscattering coefficients obtained from theoretical surface scattering models together with an assumed range of soil parameters, which are comprised of the soil moisture and surface roughness parameters. The geometry of backscattering from a rough soil surface is shown in Figure 5-9, where an incident wave from the radar system impinges upon a boundary described by the function $z = f(x, y)$ between two media and is scattered. The backscattering returns from the rough surface are obtained by the radar system. In our approach, $f(x, y)$ is a Gaussian random variable with a mean of zero. The roughness parameters—root-mean-square (rms) height σ and correlation length ℓ—are described by a Gaussian random process. The surface scattering models include the small perturbation method (SPM) [34], and the Kirchhoff approximation (or physical optics approximation) [74]. In the small perturbation model, field solutions are expanded in a perturbation series assuming that $k_{zi}f(x', y')$, $k_{1zi}f(x', y')$, $\frac{\partial f(x',y')}{\partial x'}$ and $\frac{\partial f(x',y')}{\partial y'}$ are small parameters, where k_{zi} and k_{1zi} are the $\hat{z}$-components of the incident and transmitted wave vectors, respectively. Therefore, SPM is valid if the surface variations are much smaller than the wavelength and the slope of the rough surface is relatively small. The HH and VV backscattering coefficients obtained from the first-order SPM are

$$\begin{aligned}\sigma_{hh} &= 4k^4\sigma^2\ell^2\cos^4\theta_i|R_h|^2 e^{-k^2\ell^2\sin^2\theta_i} \\ \sigma_{vv} &= 4k^8\sigma^2\ell^2\cos^4\theta_i\left|\frac{(k_1^2-k^2)(k_1^2\sin^2\theta_i+k_{1zi}^2)}{(k_1^2k_{zi}+k^2k_{1zi})^2}\right|^2 e^{-k^2\ell^2\sin^2\theta_i}\end{aligned} \qquad (5.12)$$

where k is the wavenumber in the region above the rough soil surface and, in our case, is equal to k_0, the free space wavenumber; k_1 is the wavenumber in the soil region;

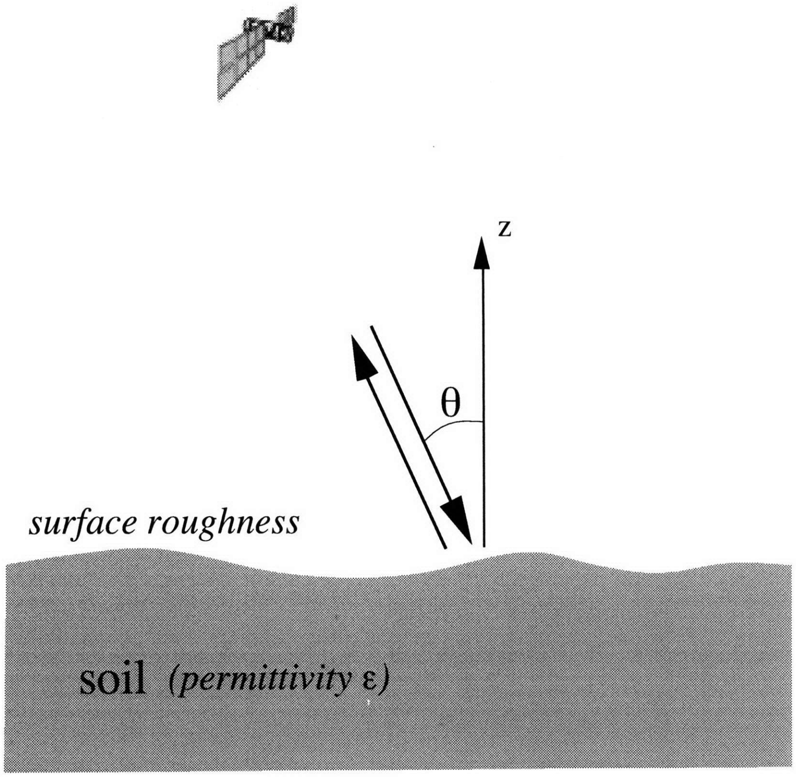

Figure 5-9: The geometry of backscattering from a rough soil surface.

θ_i is the incident angle from the vertical direction; σ and ℓ are the rms height and correlation length of the rough soil surface, respectively. R_h is the Fresnel reflection coefficient for the horizontally polarized wave and can be expressed as

$$R_h = \frac{k_{iz} - k_{1iz}}{k_{iz} + k_{1iz}} \tag{5.13}$$

where $k_{iz} = k\cos\theta_i$ and $k_{1iz} = k_1\cos\theta_i$. The small perturbation model is used to obtain the P-band (0.4 GHz) and L-band (1.25 GHz) backscattering coefficients for training. The Kirchhoff approximation approximates the field at any point on the surface by the field which would exist on the tangent plane at that point. Therefore, at every point on the surface, the radius of curvature should be large compared to the incident wavelength. In the high frequency limit, the Kirchhoff approximation reduces to the geometric optics solution [74], which can be obtained using the method of stationary phase. The scattered intensity is proportional to the probability of having the slopes such that the incident and scattered wave directions form a specular reflection. The HH and VV backscattering coefficients are

$$\sigma_{hh} = \sigma_{vv} = \frac{|R|^2\ell^2}{4\cos^4\theta_i\sigma^2} e^{-\frac{\ell^2(k_{dx}^2+k_{dy}^2)}{4\sigma^2 k_{dz}^2}} \tag{5.14}$$

where

$$\begin{aligned}
k_{dx} &= 2k\sin\theta_i\cos\phi_i \\
k_{dy} &= 2k\sin\theta_i\sin\phi_i \\
k_{dz} &= 2k\cos\theta_i
\end{aligned} \tag{5.15}$$

R is the reflection coefficient at normal incidence and can be expressed in terms of ϵ_1, the dielectric constant of the soil region, as follows

$$|R| = \left| \frac{1 - \sqrt{\epsilon_1}}{1 + \sqrt{\epsilon_1}} \right| \tag{5.16}$$

This approximation is used to obtain the C-band (5.3 GHz) backscattering coefficients for training. Soil permittivity is calculated from the soil moisture and the assumed soil texture on the basis of an empirical formulae for C- and L-bands [19], and for P-band [83].

During the training process, we have tested several combinations of the backscattering coefficients as the inputs to the neural net. For each case, the outputs from the net are compared with desired soil parameters in order to adjust the interconnecting weights. The process is repeated for each input-output data entry and then for the entire training data set until convergence is reached. After training, the values of weights which render the best result are obtained. The inversion can be performed by supplying backscattering data to the trained neural net to retrieve the soil parameters.

5.2.2 Inversion Results

To verify the effectiveness of this technique, the retrieved soil parameters are compared with the desired soil parameters. For the cases considered, the incident angle is 40 degrees, and the neural network used is a three-layer perceptron with six nodes in each of the two hidden layers. The results can be divided into two cases. The first one is the inversion of three soil parameters—soil moisture, rms height, and correlation length. The input vector in a training data set contains multi-frequency, multi-polarization backscattering coefficients which are generated from surface scattering models with the assumed range of soil moisture from 2% to 40% in 20 increments, rms height from 1 to 2 cm in 6 increments, and correlation length from 9 to 13 cm in 5 increments. There are a total of 600 input vectors in a training data set. Soil moisture, rms height, and correlation length are specified for each input vector. We want to determine whether these three parameters can be retrieved correctly when we apply the backscattering data to the trained neural net.

In reality, surface roughness parameters are difficult to measure and to characterize. If there is a set of data containing information on soil moisture only, not rms height or correlation length, we want to know whether we can utilize this set of data to train the neural net and retrieve soil moisture for another set of data. This is the second case to be shown. For this case, the backscattering coefficients again are generated from the surface scattering models with the assumed range of soil moisture from 2% to 40% in 20 increments, rms height from 1 to 2 cm in 6 increments, and correlation length from 9 to 13 cm in 5 increments. However, only soil moisture is specified for each input vector in the training data set. We want to determine whether soil moisture can be inverted correctly when we apply the backscattering data to the trained neural net.

Table 5.1 summarizes the results for the two cases described above. The rms error

e is defined as

$$e = \sqrt{\frac{\sum_{k=1}^{M}(y_k - d_k)^2}{M}} \tag{5.17}$$

where y_k and d_k are the actual output and desired output for the kth input vector in the backscattering data, respectively. There are M input vectors in the backscattering data to be inverted. The first two rows in Table 5.1 correspond to the first case in which three soil parameters are inverted. For the inversion result shown on the first row, there are four inputs to the neural net—the HH and VV backscattering coefficients in the P-band and L-band. The rms error of the retrieved soil moisture is 1.97. The rms errors of the inverted rms height and correlation length are 0.13 cm and 0.1 cm, respectively. For the inversion result shown on the second row, there are six inputs to the neural net—the HH and VV backscattering coefficients in the P-band, L-band, and C-band. The rms errors of the retrieved soil moisture, rms height, and correlation length are 0.99, 0.06 cm, and 0.06 cm, respectively. Therefore, using either 4 inputs or 6 inputs to the neural network gives good inversion results for all three soil parameters. However, the inversion is better with 6 input nodes than with 4 input nodes because the amount of ambiguity can be reduced with more inputs. The third row in Table 5.1 corresponds to the second case in which only soil moisture is retrieved without knowing the surface roughness parameters. There are four inputs, namely, the HH and VV backscattering coefficients in the P-band and L-band. The rms error of the retrieved soil moisture is 0.39. The result for this case is better than the result for the first case where three soil parameters are retrieved.

Number of Inputs	Number of Outputs	RMS Error in Moisture (%)	RMS Error in RMS Height (cm)	RMS Error in Correlation Length (cm)
4	3	1.97	0.13	0.10
6	3	0.99	0.06	0.06
4	1	0.39	N/A	N/A

Table 5.1: RMS error of the retrieved soil parameters using neural networks with different number of inputs and outputs.

Instead of trying to improve the results for all three parameters, the neural net in this case only needs to improve the result for soil moisture, but at the expense of surface roughness parameters. Although the rms errors in the inversion of soil moisture are small as shown in Table 5.1, in reality, the rms errors in the inversion are larger with experimental data since there is noise present. The inversion in this section is used as an initial test to see the effectiveness of neural networks for retrieval of geophysical parameters.

5.3 Inversion of Sunflower Biomass

In Chapter 3.3, the developed structural model is applied to interpret the multi-frequency, multi-polarization radar backscattering returns from sunflower fields acquired during three flights for the airborne Remote Sensing Campaign Mac-Europe 91 at the Montespertoli test site in Italy [5]. The result shows a good agreement between the model simulation and the experimental data. Since the model has been validated with experimental data which contain both co-polarized returns and cross-polarized returns, the scattering returns obtained from the model are utilized to train the neural network for the inversion of sunflower biomass. The inversion results obtained using different combinations of backscattering coefficients as inputs to the neural networks will be analyzed.

5.3.1 Approach for the Inversion

The training data for the inversion of sunflower biomass include the polarimetric backscattering coefficients from the developed structural model for sunflower fields based on the ground truth measured at the Montespertoli test site in Italy during the campaign, and the information of the sunflower biomass. The topology of the neural network used is a three-layer perceptron with twelve nodes in each of the two hidden layers shown in Figure 5-10. To determine the number of nodes to use in each hidden layer, a systematic study is performed starting with zero node and then increasing the number until the performance of the network does not change significantly. Unlike the inversion of soil moisture described in the previous section, the use of HH and VV backscattering returns alone may not be enough for the training of the neural net because there is not enough dynamic range between different sunflower biomass. Therefore, during the training process, different combinations of the backscattering coefficients are used as the input to the neural net including HV backscattering coefficients. For each case, the output from the neural net is compared with the desired sunflower biomass to adjust the interconnecting weights. The process is repeated for each input-output pair and then for the whole training set until convergence is reached. After training, the backscattering coefficients are applied to the trained neural network to retrieve the sunflower biomass.

5.3.2 Inversion Results

In the final step of the inversion process, different cases are analyzed by changing the components of the neural network input. Starting with one element in the input vector, six cases are examined since three backscattering coefficients for both L-band and C-band are available. The smallest RMS error in sunflower biomass is obtained with L-band HV backscattering coefficient. The result is consistent with the observation made from the HV backscattering data shown in Chapter 3.3 since there is more dynamic range across different sunflower biomass. Increasing the number of components in the neural network input progressively decreases the RMS error. Neural network is capable of combining the information from each input node constructively. Table 5.2 summarizes some of the retrieval results with different neural network inputs. The first column shows the input to the neural net. The root-mean-square errors in forest biomass are displayed in the second column. From the table, the best result is obtained by using a six component input which includes L-band and C-band HH, VV, and HV backscattering coefficients. Figure 5-11 shows the inversion result with L-band and C-band HH, VV, and HV backscattering coefficients as the neural net input. The horizontal axis is the actual sunflower biomass. The vertical axis is the

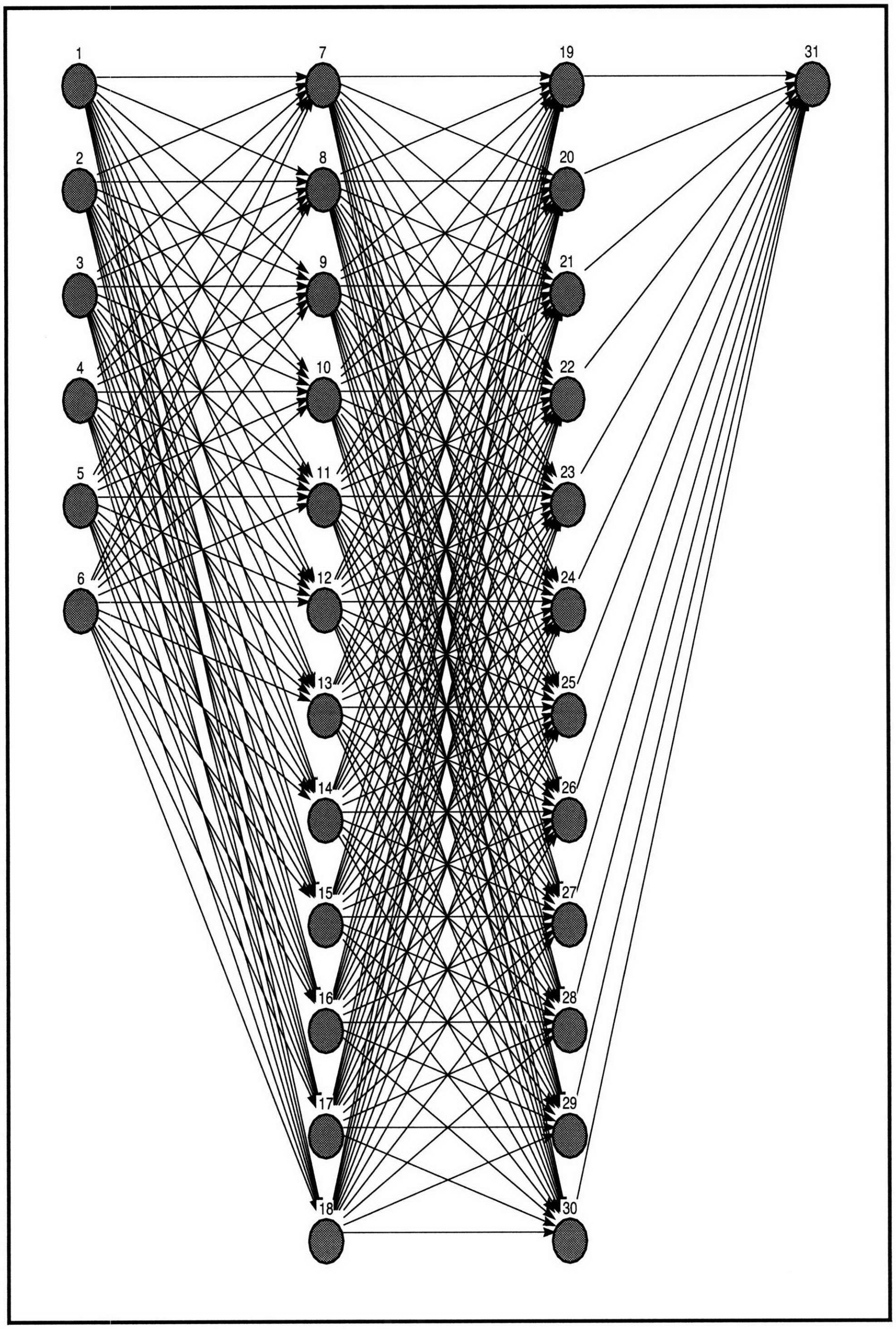

Figure 5-10: A three-layer perceptron for the inversion of sunflower biomass. Each circle represents a node with bias associated with it.

Input	RMS Error in Sunflower Biomass (kg/m^2)
L-band HH	2.21
L-band VV	2.30
L-band HV	0.49
L-band HH, VV	2.00
L-band HH, HV	0.47
L-band VV, HV	0.47
L-band HH, VV, HV	0.38
L- & C-band HH, VV, HV	0.31

Table 5.2: Root-mean-square errors in retrieved sunflower biomass for different neural network inputs

retrieved biomass. If the sunflower biomass obtained from the neural net is the same as the actual sunflower biomass, the plot should be a straight line. Good retrieval results are obtained since the root-mean-square error in sunflower biomass is very low (0.31 kg/m^2) compared to the standard deviation of the biomass in the training set (2.69 kg/m^2). The retrieval result shows that this inversion model is capable of performing the estimation with good level of precision.

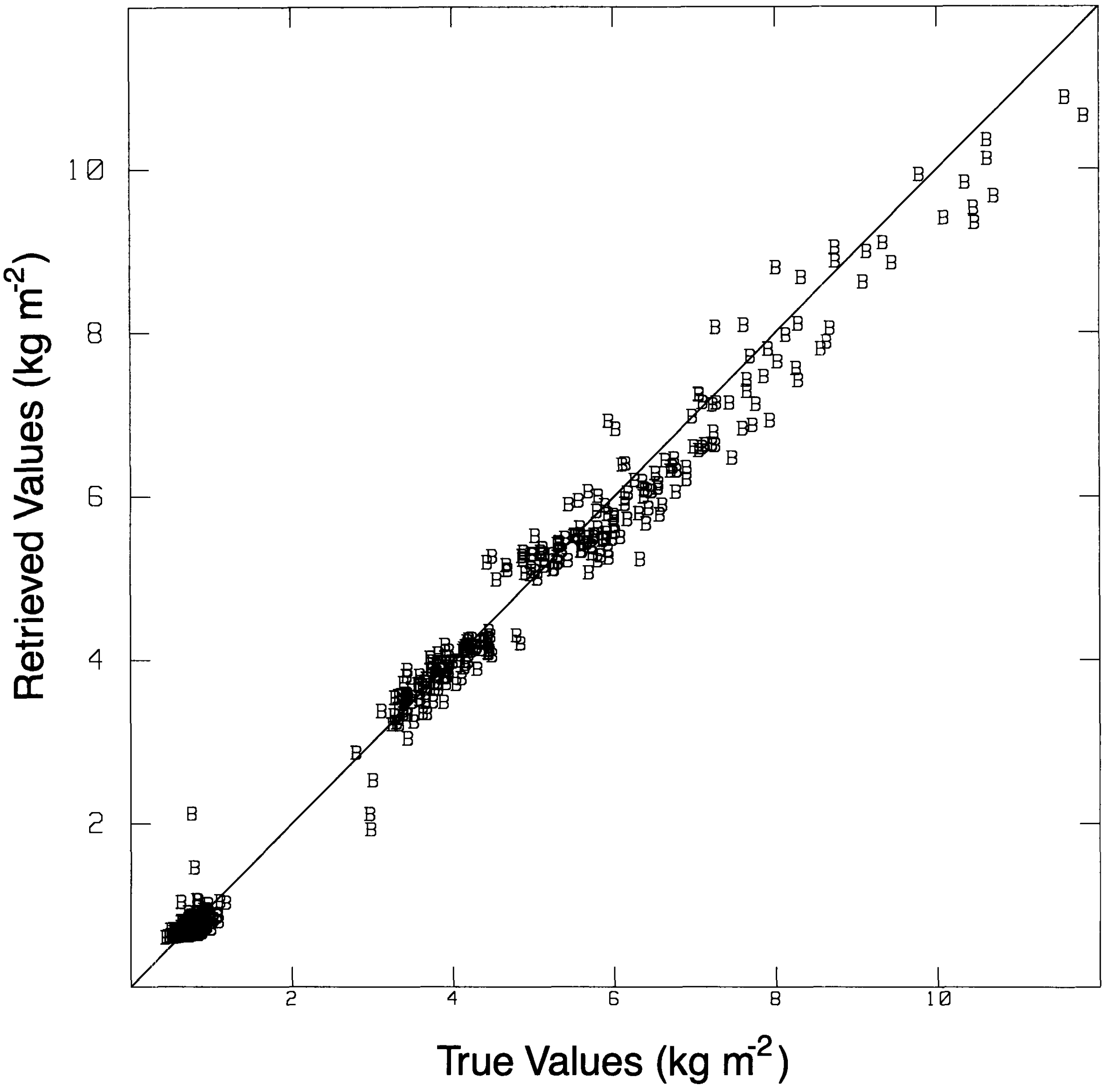

Figure 5-11: Inversion of sunflower biomass with L-band and C-band HH, VV, HV backscattering coefficients as the input to the neural network. The root-mean-square error in sunflower biomass is 0.31 kg/m^2.

5.4 Inversion of Forest Age or Forest Biomass

The retrieval of forest age (or equivalently, forest biomass) from remote sensing data is important in the studies of global change and has been a subject of great interest in recent years [40, 6, 13]. Neural networks will be applied to assess the capability of spaceborne polarimetric data for the inversion of forest age. The polarimetric radar data are acquired by the Spaceborne Imaging Radar-C (SIR-C) over the Landes Forest in France.

5.4.1 SIR-C Data at Landes Forest

The training data for inversion of forest age include the polarimetric radar data acquired by SIR-C in April 1994 over the Landes Forest in France, and the information of the forest age from the biomass map of that area [40]. The Landes Forest is a man-made forest in the southwestern part of France. The forest is formed of maritime pine and is managed in such a way that the canopy is homogeneous. The forest age and forest biomass for the pine trees in the Landes Forest can be described by a linear relationship.

$$\text{forest biomass (ton/ha)} \approx 3.17 \times \text{forest age (year)} + 1.53 \tag{5.18}$$

SIR-C is the first spaceborne radar capable of obtaining multi-frequency and multi-polarization radar data simultaneously. There are two operating frequencies. One is at L-Band (1.28 GHz), and the other is at C-Band (5.17 GHz). The incident angle over the Landes Forest is 26.4°. From the SIR-C data, we have information on the four polarization combinations HH, VV, HV, VH, and the phase difference between them. In addition to those backscattering coefficients as inputs to the neural networks, we also consider the correlation coefficients ρ between HH and VV.

$$\rho = \frac{\langle f_{vv} f_{hh}^{*} \rangle}{\sqrt{\langle |f_{vv}|^2 \rangle \langle |f_{hh}|^2 \rangle}} \tag{5.19}$$

where f_{hh} and f_{vv} are the HH and VV scattering matrix elements, respectively.

From the biomass map for the Nezer site in the Landes Forest (Figure 5-12) which provides information on the location and age of maritime pine trees, 20 forest stands ranging from 2 to 20 years old (with biomass from 8 to 65 tons/ha), and 6 areas of bare soil surface are selected. From each of these areas, an average is calculated for the HH, VV, and HV backscattering coefficients and for the correlation coefficient between HH and VV. The results are shown in Figures 5-13 to 5-18. Figure 5-13 shows the L-Band backscattering coefficient versus the forest age. There are 26 data points in the plot, which are from the 20 forest stands and 6 clear-cut areas previously chosen. The two major contributions for co-polarized scattering from the pine forest are the scattering from trees and that from the rough soil surface. When trees grow older, the scattering from trees is expected to increase until it reaches a point where the scattering doesn't change much because of attenuation. However, scattering from the soil surface is stronger for young forest than the older forest. As a consequence, the co-polarized backscattering returns are almost constant as a function of forest age.

The cross-polarized returns have an increasing trend because as the tree grows

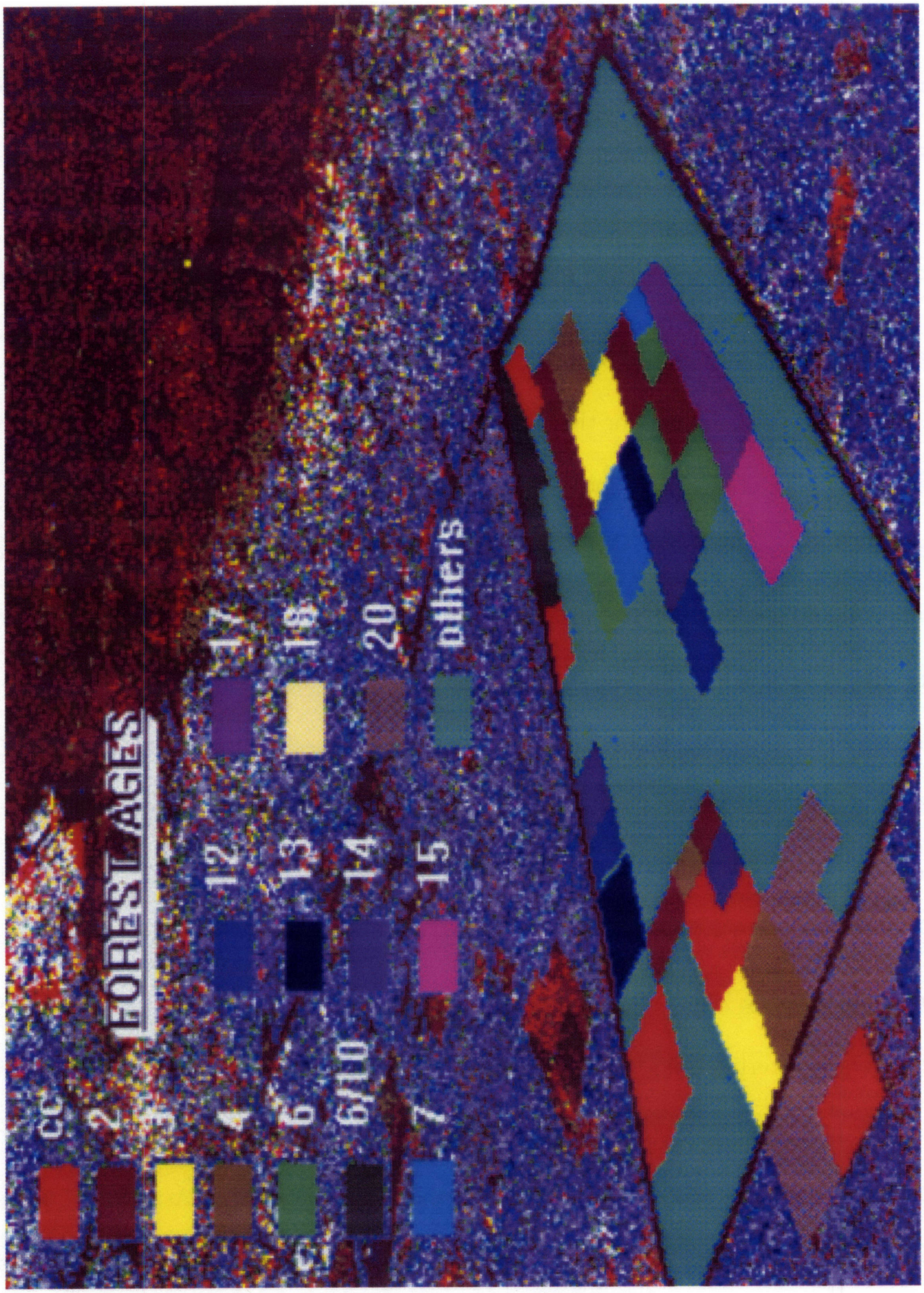

Figure 5-12: Biomass map for the Nezer site in the Landes Forest provides information about the location and age of maritime pine trees.

older, the total volume of branches increase. However, for forest stands with age greater than 15 years (or with biomass greater than 50 tons/ha), the backscattering response becomes flat. The cross-polarized returns show more sensitivity to age than the co-polarized returns.

The plot of C-Band backscattering coefficients versus the forest age is shown in Figure 5-14. The HH and VV backscattering coefficients decrease as the forest grows older until they approach a constant at around 12 years (with biomass of 40 tons/ha). This occurs because the scattering at C-band from the rough soil surface is very strong for young forest. This decreasing trend is not observed at L-band because at lower frequencies, the backscattering from the soil is not significantly higher than the backscattering from trees.

Figures 5-15 and 5-16 show the depolarization ratio HV/VV versus the forest age for the L-band and the C-band, respectively. One of the advantages of using this ratio is that the effect of miscalibration of data on the normalized term is reduced. Both plots show that the depolarization ratio appears to be a good discriminator among different forest ages. The plots of the magnitude of the correlation coefficient between the HH and VV polarizations ($|\rho|$) as a function of forest age for L-band and C-band are shown in Figures 5-17 and 5-18, respectively. From the plots, we can see that the soil surfaces are characterized by a correlation coefficient which is close to one in magnitude. This is consistent with the theoretical simulation using the Kirchhoff approximation. We expect lower $|\rho|$ for trees since they are more randomly distributed. When the forest stands are considered, $|\rho|$ drops to a value of 0.35 for older stands.

Like the inversion of sunflower biomass described in the previous section, the use of HH and VV backscattering returns alone may not be enough for the training of the neural net because there is not enough dynamic range between different forest ages. Since with the SIR-C data, we have additional information on the phase difference between HH and VV polarizations, during the training, the correlation coefficients are also used as input to the neural network. The output from the neural network is compared with the desired geophysical parameters to adjust the interconnecting weights. This process is repeated for each input-output data entry and then for the entire training data until convergence is achieved. After training, the backscattering coefficients are applied to the trained neural network to retrieve the geophysical parameters, which are then compared with the desired geophysical parameters to verify the effectiveness of this technique.

5.4.2 Inversion Results

Neural networks trained with SIR-C backscattering data and/or correlation coefficients are applied to the inversion of the forest age. Different combinations of backscattering data are used as input to the neural net in order to determine the combination which gives the best inversion result. Figure 5-19 shows the inversion result with the magnitude of the correlation coefficient, $|\rho|$, as the neural net input. The horizontal axis is the actual forest age, that is, the desired forest age presented to the neural net during the training. The vertical axis is the retrieved forest age

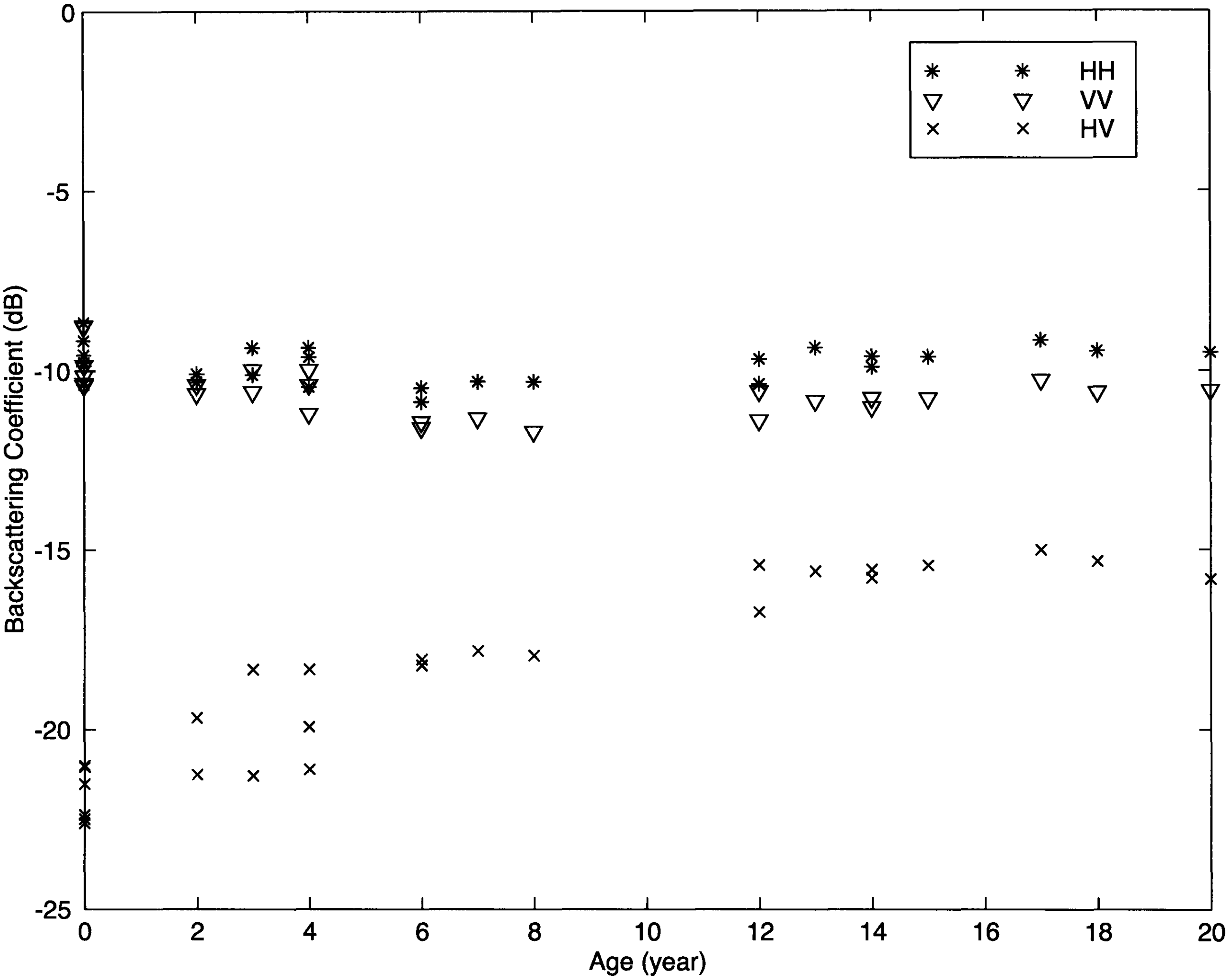

Figure 5-13: L-Band backscattering coefficients as a function of forest age are obtained from SIR-C over the Landes Forest in France [40].

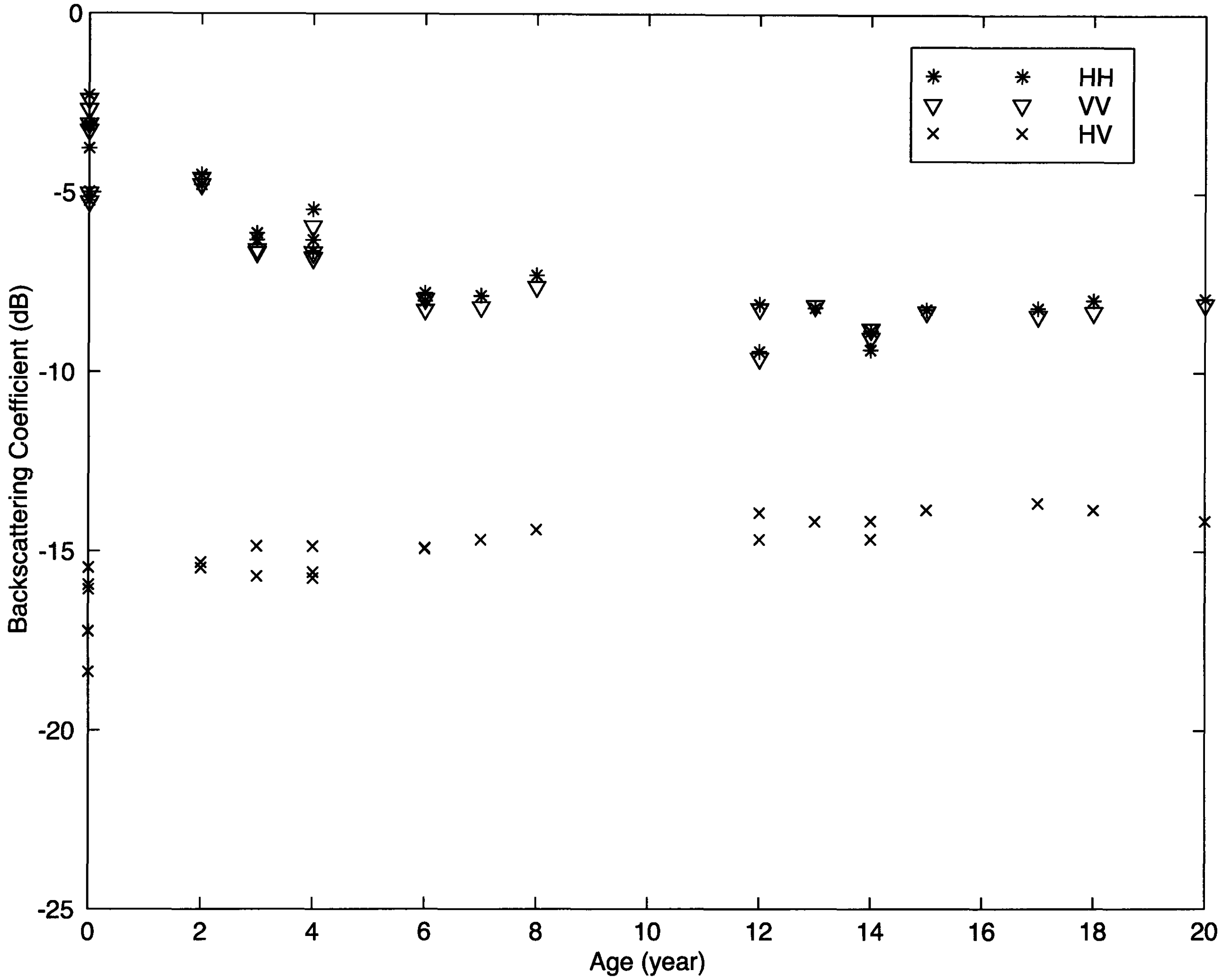

Figure 5-14: C-Band backscattering coefficients as a function of forest age are obtained from SIR-C over the Landes Forest in France [40].

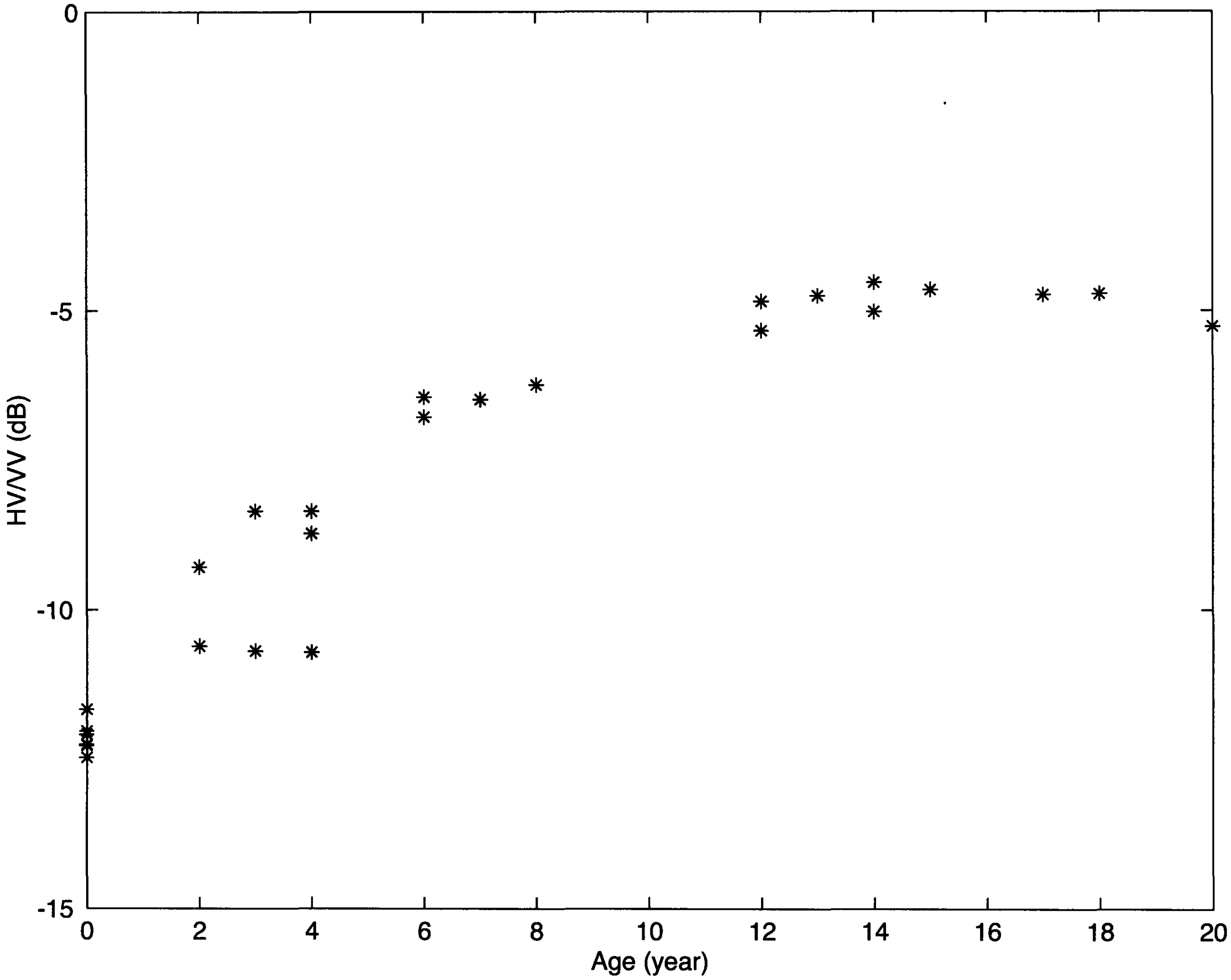

Figure 5-15: L-band depolarization HV/VV as a function of forest age are obtained from SIR-C data of the Landes Forest in France [40].

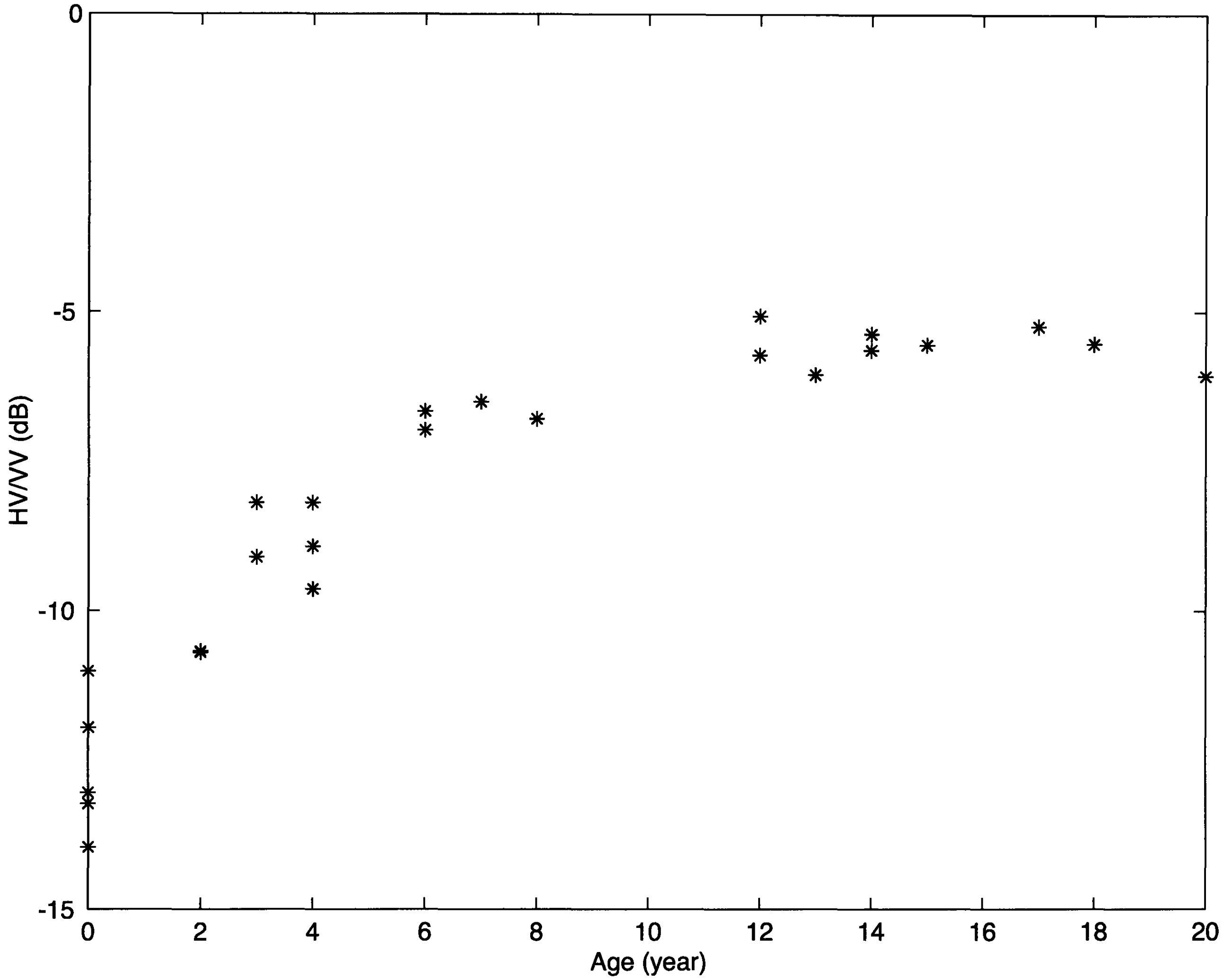

Figure 5-16: C-band depolarization HV/VV as a function of forest age are obtained from SIR-C data of the Landes Forest in France [40].

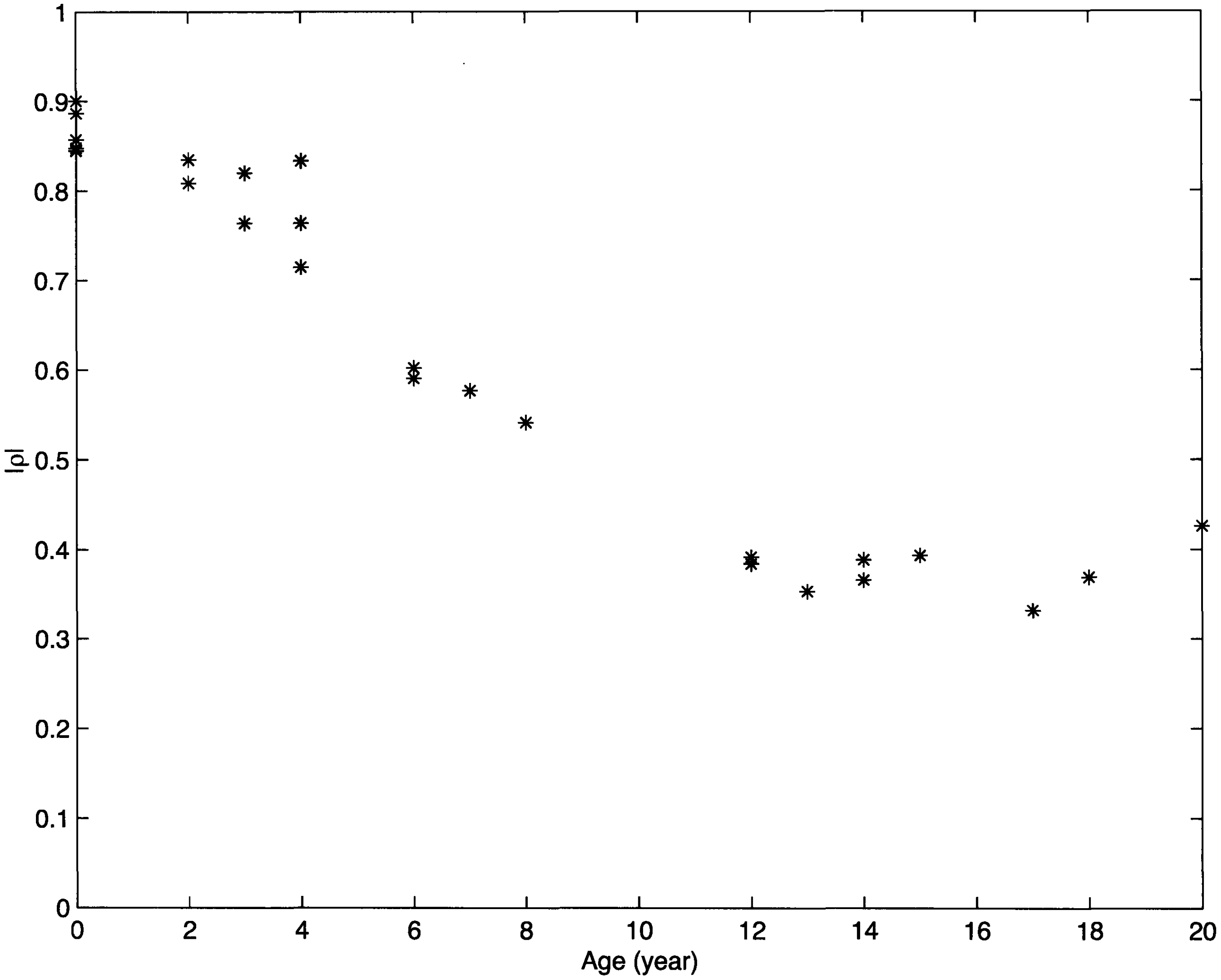

Figure 5-17: L-band $|\rho|$ as a function of forest age are obtained from SIR-C data of the Landes Forest in France [40].

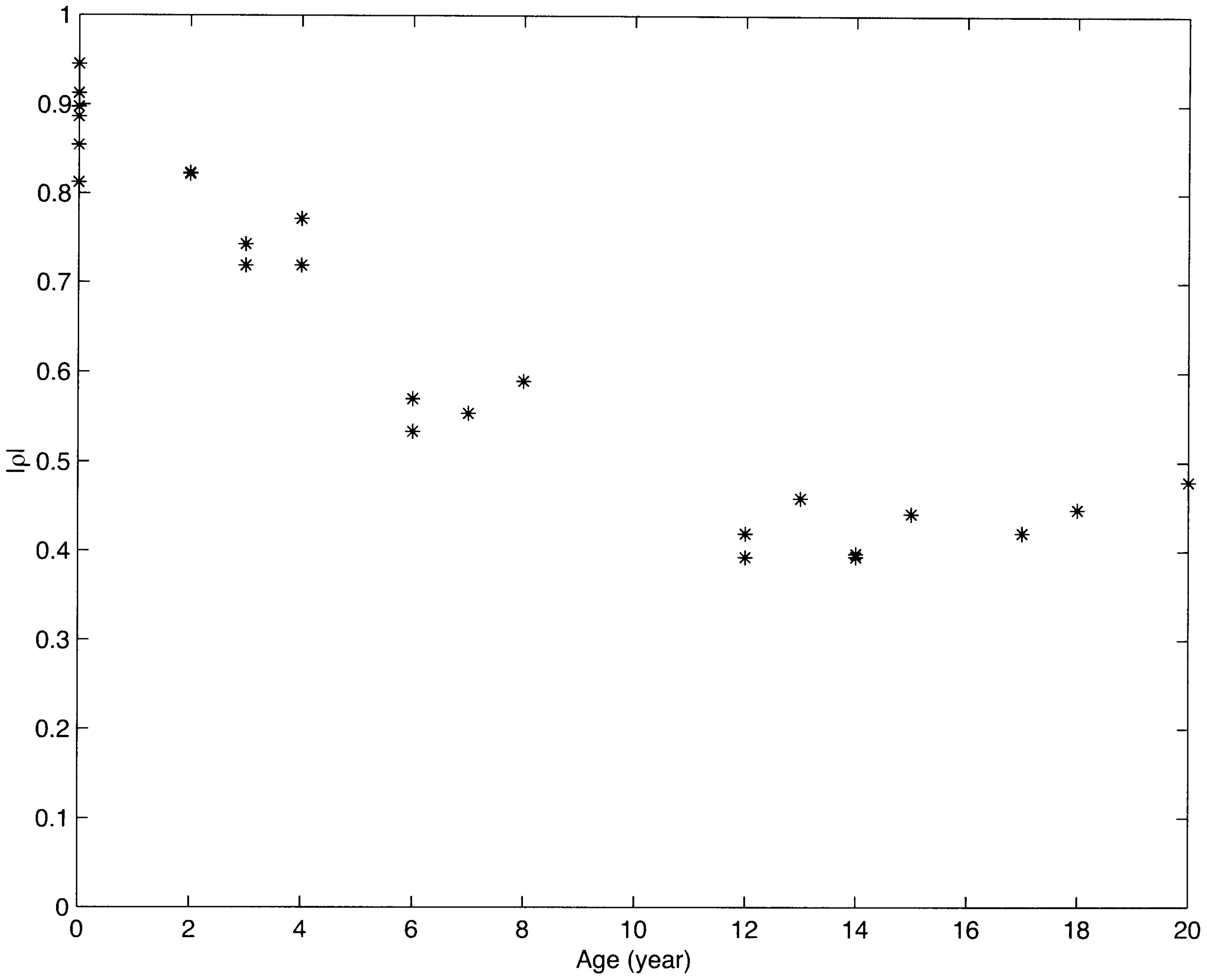

Figure 5-18: C-band $|\rho|$ as a function of forest age are obtained from SIR-C data of the Landes Forest in France [40].

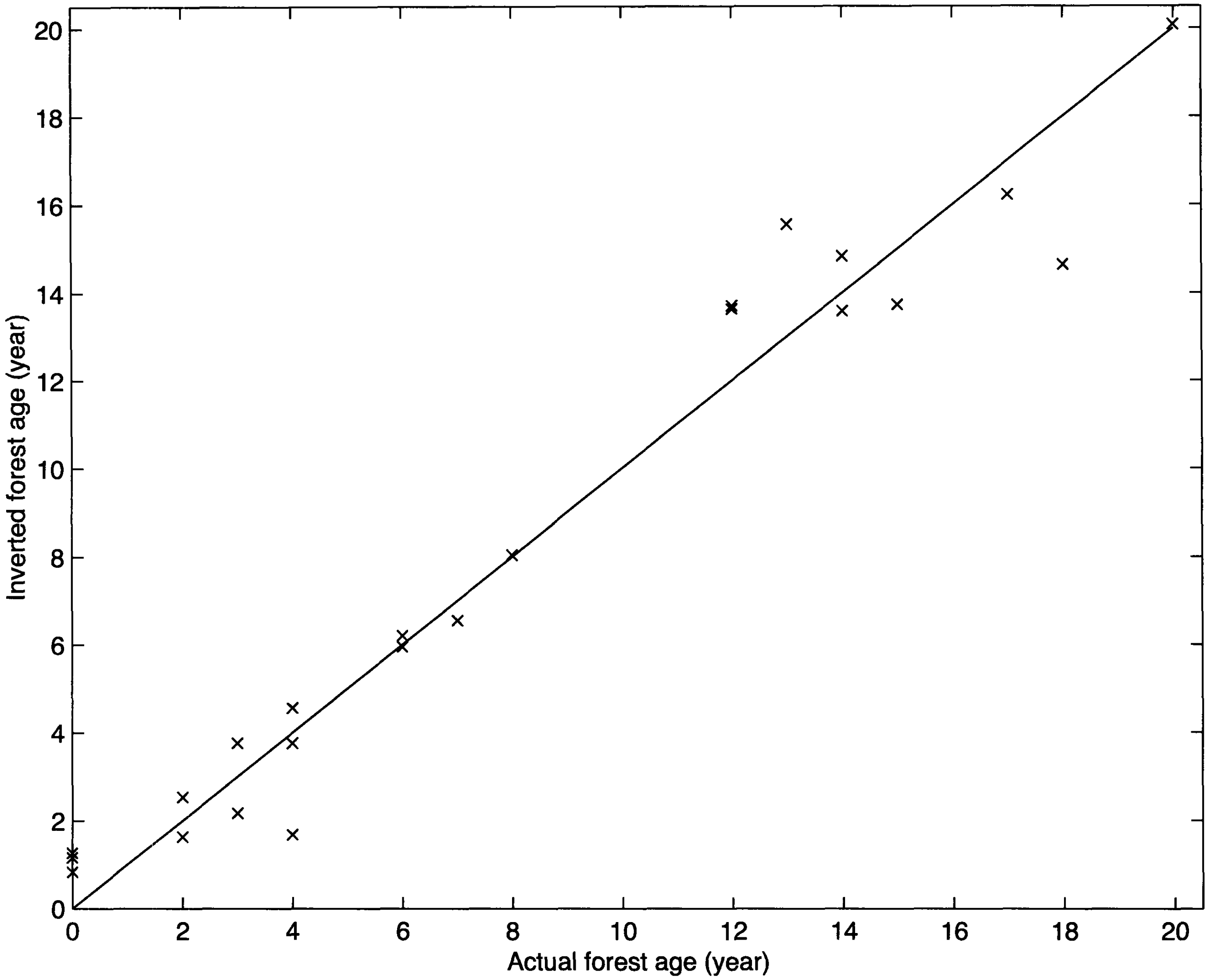

Figure 5-19: Inversion of forest age with SIR-C L-band magnitude of ρ as the input to the neural network. The root-mean-square error in forest age is 1.2 years.

which is obtained by applying the trained neural net to the backscattering data. If the forest age obtained from the neural net is the same as the actual forest age, the plot should be a straight line. Figure 5-19 is obtained by training the neural net with the average values of $|\rho|$ from the twenty-six areas selected. After training, the forest age is retrieved by presenting $|\rho|$ from the twenty-six areas to the trained neural net. The root-mean-square error in forest age is 1.2 years. This is an initial test to determine which parameters give better retrieval results. As can be predicted on the basis of the results presented in Figures 5-13 to 5-18, the inversions using the backscattering coefficients are not as accurate as the inversions using the correlation coefficients and the ratio of backscattering coefficients. In order to obtain an accurate inversion, there needs to be enough dynamic range across different forest ages. We are more interested in determining whether the correlation coefficient or the ratio yields better results. Table 5.3 summarizes some of the retrieval results with different neural network inputs. The first column shows the input to the neural net. The root-mean-square errors in forest age are displayed in the second column. It is clear from the table that using $|\rho|$ alone yields better results than using HV/HH or HV/VV by itself. In addition, the root-mean-square errors are smaller if the input includes both L-band and C-band frequencies for either $|\rho|$ or the ratios because the amount of ambiguities is reduced.

After the neural network is trained with the average values of backscattering data from the twenty-six areas we selected, the trained neural net can be applied to retrieve the forest age for the entire image. Figures 5-20, 5-21 and 5-22 show three resulting

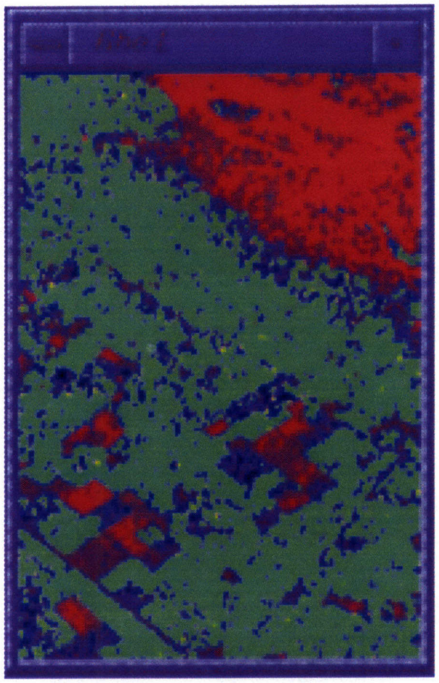

Figure 5-20: Image of retrieved forest age when the neural network is trained with L-band ρ. The colors red, black, and blue represent non-forest area, and areas populated by 2-to-6-year-old trees and 6-to-10-year-old trees, respectively. The rest of the forest is displayed in green.

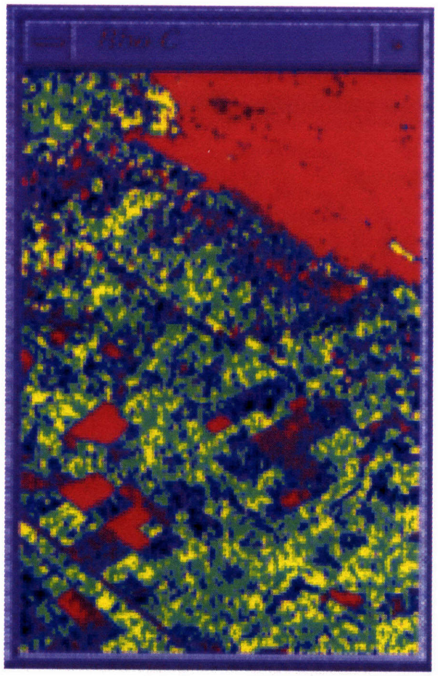

Figure 5-21: Image of retrieved forest age when the neural network is trained with C-band $|\rho|$. The colors red, black, and blue represent non-forest area, and areas populated by 2-to-6-year-old trees and 6-to-10-year-old trees, respectively. The rest of the forest is displayed in green.

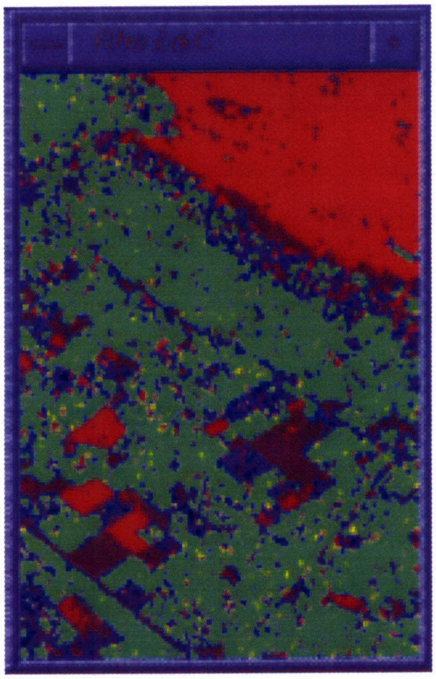

Figure 5-22: Image of retrieved forest age when the neural network is trained with both L- and C-band $|\rho|$. The colors red, black, and blue represent non-forest area, and areas populated by 2-to-6-year-old trees and 6-to-10-year-old trees, respectively. The rest of the forest is displayed in green.

Input	RMS Error in Forest Age (years)
L-band HV/HH	1.73
L-band HV/VV	1.64
C-band HV/VV	1.63
L-band $\|\rho\|$	1.23
C-band $\|\rho\|$	1.32
L- & C-band HV/VV	1.34
L- & C-band $\|\rho\|$	1.01

Table 5.3: Root-mean-square errors in retrieved forest age for different neural network inputs

images when the neural network is trained with L-band $|\rho|$, C-band $|\rho|$, or both L- and C-band $|\rho|$, respectively. Red color shows the non-forest area. Black and blue colors represent 2-to-6-year-old trees and 6-to-10-year-old trees, respectively. The rest of the forest is displayed in green. Comparing the results between the case where L-band $|\rho|$ is the neural net input to the case where C-band $|\rho|$ is the neural net input, it is clear that it is easier to distinguish the non-forest area from the young forest area using C-band $|\rho|$. However, for the older forest areas, the retrieval result using L-band $|\rho|$ is better than that using C-band $|\rho|$. As can be seen from Figure 5-18, C-band $|\rho|$ allows us to distinguish between the non-forest area and the young forest area before it reaches a plateau. With the use of both L-band and C-band $|\rho|$ as input to the neural net, we obtain an overall better result because the inversion result is similar to the C-band case for the younger forest, and to the L-band case for the older forest. Figure 5-23, 5-24 and 5-25 display the images of the retrieved forest age when the neural network is trained with HV/VV backscattering in the L-band alone, in the C-band alone, and in both the L- and C-bands, respectively. We can see that the use of HV/VV does not distinguish between different forest ages well. Table 5.4 summarizes some of the retrieval results with different neural network inputs when the trained neural network is applied to the whole image. The first column shows the input to the neural net. The root-mean-square errors in forest age are displayed in the second column. We select certain areas in which we know the forest age, and compare the retrieved values for these areas with the known values. Table 5.4 displays the rms errors for forest areas 2, 4 and 8 years of age. Again, the result of using the L- and C-band $|\rho|$ is better than using the L- and C-band HV/VV. For the inversion of forest age or biomass, the use of $|\rho|$ as the neural net input yields the best result.

5.5 Summary

Neural networks offer a computational approach which mimics biological nervous systems. They are flexible for the inversion of geophysical parameters, especially when multi-dimensional input such as multi-frequency, multi-polarization scattering data are involved. In this chapter, an overview of neural networks and a description of their use for the inversion of soil parameters and forest age are presented.

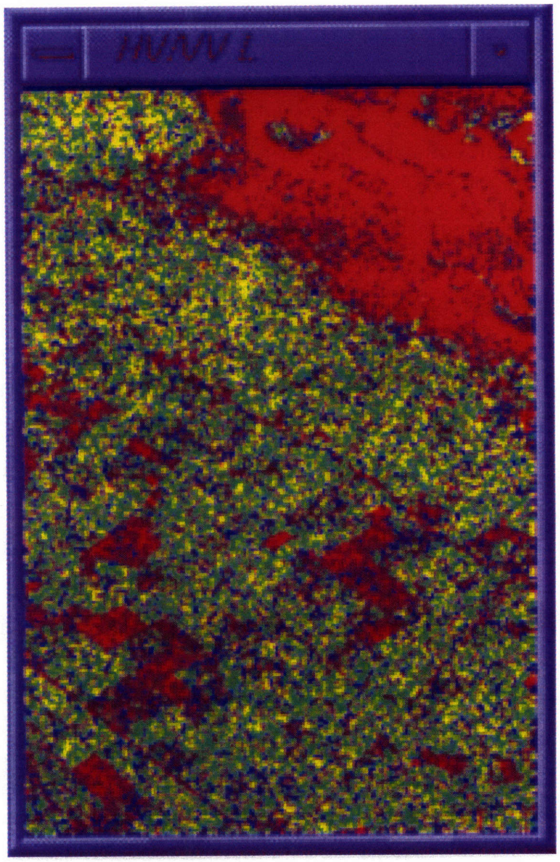

Figure 5-23: Image of retrieved forest age when the neural network is trained with L-band HV/VV. The colors red, black, and blue represent non-forest area, and areas populated by 2-to-6-year-old trees and 6-to-10-year-old trees, respectively. The rest of the forest is displayed in green.

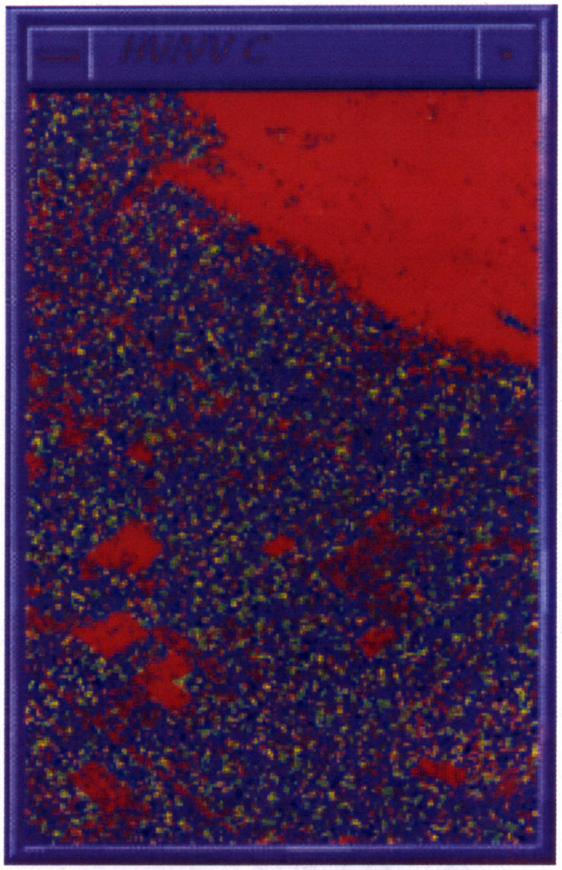

Figure 5-24: Image of retrieved forest age when the neural network is trained with C-band HV/VV. The colors red, black, and blue represent non-forest area, and areas populated by 2-to-6-year-old trees and 6-to-10-year-old trees, respectively. The rest of the forest is displayed in green.

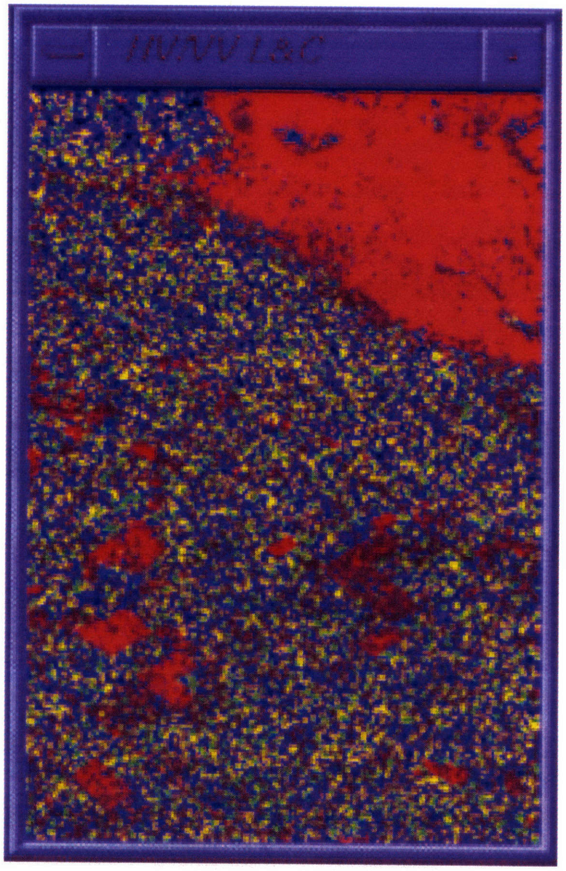

Figure 5-25: Image of retrieved forest age when the neural network is trained with both L- and C-band HV/VV. The colors red, black, and blue represent non-forest area, and areas populated by 2-to-6-year-old trees and 6-to-10-year-old trees, respectively. The rest of the forest is displayed in green.

Input	RMS Error in Forest Age		
	2 years	4 years	8 years
L-band $\|\rho\|$	1.29	2.80	4.63
L-band HV/VV	3.08	4.10	5.02
C-band $\|\rho\|$	1.19	1.91	4.50
C-band HV/VV	3.45	3.85	4.50
L- & C-band $\|\rho\|$	1.09	1.78	3.67
L- & C-band HV/VV	3.06	3.47	4.28

Table 5.4: Root-mean-square errors in retrieved forest age for different neural network inputs when the trained neural network is applied to the whole image.

The neural network architecture used in this chapter is a multi-layer perceptron trained with the back-propagation algorithm. During the training process, each input vector and its corresponding desired output from the training set are presented to the neural network so that the weights in the neural net can be adjusted to reduce the output error. The process is repeated for the entire training set until convergence in the output error is achieved. After the training is completed, the weights which produce the best result are obtained. When an input is applied to the trained neural net, the output can be computed immediately on the basis of these weights.

For the inversion of soil moisture and surface roughness parameters, the training data consist of multi-frequency polarimetric backscattering coefficients obtained from theoretical surface scattering models with an assumed range of soil parameters. Inversion results are obtained using different combinations of backscattering data as input to the neural networks. Two cases are considered. The first case involves the inversion of three soil parameters—soil moisture, rms height, and correlation length. An input vector in a training data set is a combination of P-band, L-band and C-band HH and VV backscattering coefficients. The use of multi-frequency input to the neural network is shown to provide good inversion results for all three soil parameters. However, the inversion is improved with more input nodes because the amount of ambiguity is reduced. The second case deals with the inversion of soil moisture using a neural network trained with a set of data for which only soil moisture information, but not the rms height or the correlation length of the soil surface is available. This is a practical application since surface roughness parameters in the real world are difficult to measure and to characterize. Our results suggest that a large data set containing information on soil moisture only without rms height or correlation length can be used to train a neural net intended for the retrieval of soil moisture from another set of data.

Neural networks are also applied to the inversion of sunflower biomass using neural networks. The training data are the scattering returns obtained from the developed vegetation scattering model based on the Monte Carlo approach. The simulated results from the structural model are validated by airborne Remote Sensing Campaign Mac-Europe 91 multi-frequency and multi-polarization data [5] (Chapter 3.3). Unlike the inversion of soil parameters, the use of HH and VV backscattering returns alone may not be sufficient for the training of the neural net because there is not enough dynamic range in the sunflower biomass. Therefore, the HV backscattering coefficient is also used as input to the neural network during training. Different combinations of backscattering coefficients are used as inputs to the neural networks. With only one input node, the smallest root-mean-square error in sunflower biomass is obtained with L-band HV backscattering coefficient. Increasing the number of input nodes in the neural network input progressively decreases the root-mean-square error. Although the sunflower biomass is more sensitive to cross-polarized backscattering coefficients, the neural network takes advantage of the information carried by all its inputs. The best result is obtained with six input nodes which includes L-band and C-band HH, VV, and HV backscattering coefficients. This suggests that the inversion result may be improved further with the use of additional frequencies and/or angles of observation.

To examine the performance of the use of experimental data in training the neural networks, the polarimetric radar data obtained by the Spaceborne Imaging Radar-C (SIR-C) over the Landes Forest in France [40] are utilized to train the net in order to retrieve the forest age (or equivalently, forest biomass). The training data include the information on the forest age from the biomass map of the Landes forest, and the polarimetric radar data acquired by SIR-C in April 1994 at two operating frequencies—one at L-Band (1.28 GHz) and the other at C-Band (5.17 GHz). Like the inversion of sunflower biomass, the use of HH and VV backscattering returns alone may not be enough for the training of the neural net because there is not enough dynamic range between different forest ages. Since with the SIR-C data, additional information on the phase difference between HH and VV polarizations is available, the correlation coefficients are also used as the input to the neural network during training. As we predicted, the inversions using the backscattering coefficients are not as accurate as those using the correlation coefficients and the ratio of backscattering coefficients. The neural network trained with the average values of backscattering data from the twenty-six selected areas is applied to retrieve the forest age for the entire radar image. The best inversion result is obtained with the use of both L-band and C-band magnitude of correlation coefficients as input to the neural net.

Chapter 6

Conclusion

A coherent scattering model for microwave remote sensing of vegetation canopy is developed on the basis of Monte Carlo simulations. The effects of coherent wave interactions are especially important in scattering from vegetations with closely spaced or clustered elements. The conventional analytic wave theory approach requires a knowledge of the probability density functions and the pair-distribution functions, which are usually difficult to obtain for natural vegetation. The Monte Carlo approach obviates the need of prior knowledge of these functions, and makes possible the use of more accurate and detailed structural models of complex vegetation structures. Although it is computationally more intensive, the ever increasing speed and memory capacity of modern computer have made this approach practical. The scattering model developed in this research takes into account the coherent wave interactions among vegetative elements, the contribution of different scattering mechanisms from a vegetation canopy, and the effects of attenuation on the coherent wave.

Two methods can be employed to achieve a realistic description of the vegetation structure under consideration. In one method, the number of each type of component and the relative orientations of the components are specified in the structural model up to the desired level of detail. Such a structural model is applied to rice crops and sunflowers. The developed structural model for rice crops takes into account the coherent wave interactions made prominent by the clustered and closely spaced structure of rice crops, and is validated with the ERS-1 data [41]and the multi-angular RADARSAT data [57]. It correctly predicts the increasing trend of the temporal response with rice growth. The structural model for rice crops is utilized to interpret the experimental observations from the JERS-1 data [61] such as the effects of the structure of rice fields. Monte Carlo simulations for different growth stages and rice field structures demonstrate a large variation in the L-band scattering returns from rice fields with different plant spacings, as the result of the constructive and destructive interferences among rice plants. The C-band scattering returns are affected to a lesser extent by the structure of the rice field because of the shorter wavelength of C-band. Further analysis shows that the ratio of HH polarization over VV polarization at the L-band is virtually independent of the rice field structure because of cancellation of the phase interactions. Therefore, the C-band scattering returns and the ratio of HH over VV polarizations at the L-band are useful for the inversion of rice biomass without prior knowledge of plant spacings, while the L-band scattering returns alone are of limited utility in biomass inversion without available data on the rice field structure.

A structural model is also developed for sunflowers, which, in contrast to rice plants, do not have a cluster structure, has more circular shaped leaves connected to a stem through petioles, and has a flower at the developed stage. In addition, the bottom of a sunflower field is the rough soil surface instead of water. The model is validated for both co-polarized and cross-polarized returns using the airborne Remote Sensing Campaign Mac-Europe 91 multi-frequency and multi-polarization radar backscattering data acquired for sunflower fields at the Montespertoli test site in Italy [5].

Another method to characterize vegetation structures uses growth rules. This is especially useful in modeling trees, which are structurally more complex. The Lindenmayer systems are utilized to realistically capture the architecture of trees and describe their growth. Monte Carlo simulation results of the scattering returns from trees with different structures and at various growth stages are calculated and analyzed. The structure factor which extracts the structural information of a tree and provides a measure of the spatial distribution of branches is defined. It is computed for trees with different architectures at L-band and C-band frequencies with HH, VV, and HV polarizations. Its value shows a greater variation among different types of trees at L-band as compared to C-band, a result consistent with our prior prediction.

To solve the inverse scattering problem, multi-layer perceptron neural networks trained with the back-propagation algorithm are used. These neural nets are applied to the inversion of geophysical parameters including soil moisture and surface parameters, as well as forest age (or equivalently, forest biomass). They are found to be especially useful for multi-dimensional inputs such as multi-frequency polarimetric scattering data.

For the inversion of soil moisture and surface roughness parameters, neural networks are trained with multi-frequency polarimetric backscattering coefficients derived from theoretical surface scattering models with an assumed range of soil parameters. Inversion results are obtained using different combinations of backscattering data as input to the neural networks. Two cases are considered. The first case involves the inversion of three soil parameters—soil moisture, rms height, and correlation length. An input vector in a training data set is a combination of P-band, L-band and C-band HH and VV backscattering coefficients. The use of multi-frequency input to the neural network is shown to provide good inversion results for all three soil parameters. However, the inversion is improved with more input nodes because the amount of ambiguity is reduced. The second case deals with the inversion of soil moisture using a neural network trained with a set of data for which only soil moisture information, but not the rms height or the correlation length of the soil surface is available. This is a practical application since the measurement and characterization of surface roughness parameters in the real world pose a difficult problem. Our results suggest that a large data set containing information on soil moisture only without rms height or correlation length can be used to train a neural net intended for the retrieval of soil moisture from another set of data.

Neural networks are also applied to the inversion of sunflower biomass. The training data are the scattering returns obtained from the developed vegetation scattering model based on the Monte Carlo approach where the simulated results from the structural model have been validated by Mac-Europe 91 multi-frequency and multi-polarization data [5] described in Chapter 3.3. Unlike the inversion of soil parameters, HV backscattering coefficients are also used as inputs to the neural network during training. The use of HH and VV backscattering returns alone may not be sufficient for the training of the neural net since there is not enough dynamic range in the forest age. Different cases are analysed by changing the components of the input vector. Increasing the number of input nodes in the neural network input progressively decreases the root-mean-square error. The best result is obtained with six input nodes which includes L-band and C-band HH, VV, and HV backscattering coefficients. This suggests that the inversion result may be improved further with the use of additional frequencies and/or angles of observation.

The performance of the use of experimental data as the neural network training data for the inversion is also demonstrated. To retrieve the forest age (or equivalently, forest biomass), the training data include the the multi-frequency polarimetric radar data acquired by SIR-C over the Landes Forest in France and the information on the forest age from the biomass map of that area [40]. Since with the SIR-C data, additional information on the phase difference between HH and VV polarizations is available, the correlation coefficients ρ are also used as the input to the neural network during training. Inversions using the backscattering coefficients are not as accurate as those using the correlation coefficients and the ratio of backscattering coefficients. The neural network trained with the average values of backscattering data from the twenty-six selected areas is applied to retrieve the forest age for the entire radar image. We have demonstrated that the best inversion result is obtained with the use of both L-band and C-band magnitude of correlation coefficients as input to the neural network.

Bibliography

[1] Abelson, H., and A. A. diSessa, *Turtle Geometry*, M.I.T. Press, Cambridge, 1982.

[2] Aschbacher, J., A. Pongsrihadulchai, S. Karnchanasutham, C. Rodprom, D. R. Paudyal, and T. Le Toan, "Assessment of ERS-1 data for rice crop mapping and monitoring," *Proceedings of the International Geoscience and Remote Sensing Symposium*, pp. 2183-85, Florence, Italy, July, 1995.

[3] Au, W.C., J.A. Kong, and L. Tsang, "Absorption enhancement of scattering of electromagnetic waves by dielectric cylinder clusters," *Microwave and Optical Technology Letters*, Vol. 7, No. 10, pp. 454-457, 1994.

[4] Barnsley, M. F., *Fractals Everywhere*, Academic Press, San Diego, 1988.

[5] Baronti, S., F. del Frate, P. Ferrazzoli, S. Paloscia, P. Pampaloni, G. Schiavon, "SAR polarimetric features of agricultural areas," *Int. J. of Remote Sensing*, Vol. 16, pp. 2639-2656, 1995.

[6] Beaudoin, A., T. Le Toan, S. Goze, E. Nezry, A. Lopes, E. Mougin, C.C. Hsu, H.C Han, J.A. Kong and R.T. Shin, "Retrieval of forest biomass from SAR data,"

Int. J. of Remote Sensing, Vol. 15, No. 13, 1994.

[7] Binder, K., and D. W. Heermann, *Monte Carlo Simulation in Statistical Physics: An Introduction*, Springer Verlag, 1988.

[8] Bischof, H., "Multispectral classification of Landsat images using neural networks, " *IEEE Transactions on Geoscience and Remote Sensing*, Vol. 28, pp. 482-489, 1992.

[9] Borgeaud, M., S. V. Nghiem, R. T. Shin, and J. A. Kong, " Theoretical models for polarimetric microwave remote sensing of earth terrain," *J. Electromagnetic Waves and Applications*, Vol. 3, No. 1, 61-81, 1989.

[10] Chen, Z., L. Tsang, and G. Zhang, "Scattering of electromagnetic waves by vegetation based on the wave approach and the stochastic Lindenmayer system," *Microwave and Optical Technology Letters*, Vol. 8, No. 1, pp. 30-33, 1995.

[11] Cimino, J. B., C. Elachi, and M. Settle, "SIR-B—the second shuttle imaging radar experiment," *IEEE Transactions on Geoscience and Remote Sensing*, Vol. 24, pp.445-452, 1986.

[12] Dobelmann, J.-P., *Riziculture Pratique, Tome I: riz irrigué*, Presses Universitaires de France, Paris, 1976.

[13] Dobson, M. C., F. T. Ulaby, T. Le Toan, A. Beaudoin, E.S. Kasischke, and N.

Christensen, "Dependence of radar backscatter on conifer forest biomass," *IEEE Transactions on Geoscience and Remote Sensing*, Vol. 30, pp. 412-415, 1992.

[14] Durden, S. L., J. J. van Zyl, and H. A. Zebker, "Modeling and observation of the radar polarization signature of forested areas," *IEEE Transactions on Geoscience and Remote Sensing*, Vol. 27, pp. 290-301, May 1989.

[15] Elachi, C., editor, "Special issue on the shuttle imaging radar (SIR-B)," *IEEE Transactions on Geoscience and Remote Sensing*, Vol. 24, 1986.

[16] European Space Agency, *The ERS-1 System*, ESA SP-1146, 1992.

[17] Fung, A. K., and H. S. Fung, "Application of first-order renormalization method to scattering from a vegetation-like half-space," *IEEE Trans. Geosci. Electron.,* Vol. 15, pp. 189-195, 1977.

[18] Fung, A. K., and F. T. Ulaby, "A scatter model for leafy vegetation," *IEEE Trans. Geosci. Electron.,* Vol. 16, pp. 281-285, 1978.

[19] Hallikainen, M. T., F. T. Ulaby, M. C. Dobson, M. A. El-Rayes, and L. K. Wu, "Microwave dielectric behaviour of wet soil. Part I : Empirical models and experimental observations," *IEEE Transactions on Geoscience and Remote Sensing,* Vol. 23, pp. 25-34, 1985.

[20] Hammersley, J. M., and D. C. Handscomb, *Monte Carlo Methods*, John Wiley & Sons, New York, 1964.

[21] Heermann, P. D. and K. Khazenie, "Classification of multispectral remote sensing data using a back-propagation neural network," *IEEE Transactions on Geoscience and Remote Sensing*, Vol. 30, pp. 81-88, 1992.

[22] Honda, H., "Description of the form of trees by the parameters of the tree-like body: Effects of the branching angle and the branch length on the shape of the tree-like body," *Journal of Theoretical Biology*, Vol. 31, pp. 331-338, 1971.

[23] Honda, H., P. B. Tomlinson, and J. B. Fisher, "Two geometrical models of branching of botanical trees," *Annals of Botany*, Vol. 49, pp. 1-11, 1982.

[24] Hopfield, J. J., and D. W. Tank, "Computing with neural circuits: a model," *Science*, Vol. 233, 625-633, August 1986.

[25] Hsu, C. C., "Theoretical Models for Microwave Remote Sensing of Forest and Vegetation," *Ph.D. Dissertation, MIT*, 1996

[26] Huet, M., "Evolution des paramètres de structure et de biomasse d'un couvert de blé: Utilization des techniques de télédétection microondes," *Thèse de l'Université Paul Sabatier*, Spécialité Astronomie et Techniques Spatiales, Toulouse, France, 1983.

[27] Imhoff, M. L., "A theoretical analysis of the effect of forest structure on synthetic aperture radar backscatter and the remote sensing of biomass," *IEEE Transactions on Geoscience and Remote Sensing,* Vol. 33, No. 2, pp. 341-352, March 1995.

[28] IRRI, *1993-1995 IRRI Rice Almanac*, International Rice Research Institute, Philippines, 1995.

[29] Ishimaru, A., *Wave Propagation and Scattering in Random Media, Vol. I*, Academic Press, New York, 1978.

[30] Johnson, J. T., "Application of numerical models for rough surface scattering," *Ph.D. Dissertation, MIT*, 1996

[31] Karam, M. A. and A. K. Fung, "Scattering from randomly oriented circular discs with application to vegetation," *Radio Science,* Vol. 18, No. 4, pp. 557-565, July 1983.

[32] Karam, M. A., A. K. Fung, and Y. M. M. Antar, "Electromagnetic wave scattering from some vegetation samples," *IEEE Transactions on Geoscience and Remote Sensing,* Vol. 26, No. 6, pp. 799-808, November 1988.

[33] Karam, M. A. and A. K. Fung, "Electromagnetic scattering from a layer of finite length, randomly oriented, dielectric, circular cylinders over a rough interface

with application to vegetation" *Int. J. of Remote Sensing*, Vol. 9, No. 6, pp. 1109-1134, 1988.

[34] Kong, J. A., *Electromagnetic Wave Theory*, Second Edition, John Wiley & Sons, New York, 1990.

[35] Kurosu, T., T. Suitz, and T. Moriya, "Rice crop monitoring with ERS-1 SAR: a first year result," *Proc. Second ERS-1 Symp.*, Vol. 1, pp. 97-101, Hamburg, Germany, October, 1993.

[36] Kurosu, T., M. Fujita, and K. Chiba, "Monitoring of rice crop growth from space using the ERS-1 C-band SAR," *IEEE Transactions on Geoscience and Remote Sensing*, Vol. 33, 1092-1096, 1995.

[37] Lang, R. H.,"Electromagnetic backscattering from a sparse distribution of lossy dielectric scatterers," *Radio Science*, Vol. 16, No. 1, 15-30, 1981.

[38] Lang, R. H. and J. S. Sidhu,"Electromagnetic backscattering from a layer of vegetation: a discrete approach," *IEEE Transactions on Geoscience and Remote Sensing,* Vol. GE-21, No. 1, 1983.

[39] Le Toan, T., H. Laur, E. Mougin, and A. Lopes, "Multitemporal and dual-polarization observations of agricultural vegetation covers by X-band SAR images," *IEEE Transactions on Geoscience and Remote Sensing*, Vol. 27, No. 6, 709-718, 1989.

[40] Le Toan, T., A. Beaudoin, J. Riom and D. Guyon, "Relating forest biomass to SAR data," *IEEE Transactions on Geoscience and Remote Sensing*, Vol. 30, No. 2, March 1992.

[41] Le Toan, T., F. Ribbes, N. Floury, L. Wang, K. H. Ding, C. C. Hsu, and J. A. Kong, "On the retrieval of rice crop parameters from SAR data," *Proceedings of International Symposium on the Retrieval of Bio- and Geophysical Parameters from SAR Data for Land Applications*, pp. 233-243, Toulouse, France, October 1995.

[42] Le Toan, T., F. Ribbes, L. Wang, N. Floury, K. H. Ding, J. A. Kong, N. Fujita, and T. Kurosu, "Rice crop mapping and monitoring using ERS-1 data based on experiment and modeling results," *IEEE Transactions on Geoscience and Remote Sensing*, Vol. 35, No. 1, 41-56, 1997.

[43] Le Vine, D. M., A. Schneider, R. H. Lang, and H. G. Carter "Scattering from thin dielectric disks," *IEEE Transactions on Antennas and Propagation*, Vol. 33, No. 12, pp. 1410-1413, December 1985.

[44] Lindenmayer, A. "Mathematical models for cellular interaction in development, parts I and II ," *Journal of Theoretical Biology*, Vol. 18, No. 12, pp. 280-315, 1968.

[45] Lindenmayer, A., "Adding continuous components to L-systems," *L Systems*,

Lecture Notes in Computer Science 15, pp 53-68, Springer Verlag, Berlin, 1974.

[46] Lippmann, R. P.,“An introduction to computing with neural nets,” *IEEE Acoustics Speech and Signal Processing Magazine*, Vol. 4, No. 2, 4-22, April 1987.

[47] Mandelbrot, B. B., *The Fractal Geometry of Nature*, W. H. Freeman, San Francisco, 1982.

[48] Marchuk, G. I., G. A. Mikhailov, M. A. Nazaraliev, R. A. Darbinjan, B. A. Kargin, and B. S. Elepov, *The Monte Carlo Methods in Atmospheric Optic*, Springer-Verlag, 1980.

[49] Nemoto, Y., H. Nishino, M. Ono, H. Mizutamari, K. Nishikawa, and K. Tanaka, “Japanese Earth Resources Satellite-1 synthetic aperture radar,” *Proc. IEEE*, Vol. 79, pp. 800-809, 1991.

[50] Pak, K., L. Tsang, C. H. Chan, and J. Johnson, “Backscattering enhancement of electromagnetic waves from 2-D perfectly conducting random rough surfaces based on Monte Carlo simulations,” *Journal of the Optical Society of America A (Optics, Image Science and Vision)*, Vol. 12, 2491-2499, 1995.

[51] Peitgen, H., and D. Saupe, *The Science of Fractal Images*, Springer-Verlag, New York, 1988.

[52] Prusinkiewicz, P., "Graphical applications of L-systems," *Proc. Graphics Interface '86 - Vision Interface '86*, pp. 247-253, CIPS, 1986.

[53] Prusinkiewicz, P., "Applications of L-systems to computer imagery," *Graph Grammars and their Applications to Computer Science; Third International Workshop*, pp. 534-548, Berlin, 1987.

[54] Prusinkiewicz, P., A. Lindenmayer, and J. Hanan, "Developmental models of herbaceous plants for computer imagery purposes," *Proc. SIGGRAPH '88*, Atlanta, Georgia, August, 1988.

[55] Prusinkiewicz, P., and A. Lindenmayer, *The Algorithmic Beauty of Plants*, Springer-Verlag, New York, 1990.

[56] Prusinkiewicz, P., and J. Hanan, "Visualization of botanical structures and processes using parametric L-systems," *Scientific Visualization and Graphics Simulation*, pp 183-201, John Wiley & Sons, 1990.

[57] Raney, R. K., A. P. Luscombe, E. J. Langham, and S. Ahmed, "RADARSAT (SAR imaging)," *Proc. IEEE*, Vol. 79, pp. 839-849, 1991.

[58] Rosenbaum, S. and L. W. Bowles, "Clutter return from vegetated areas," *IEEE Transactions on Antennas and Propagation*, Vol. 22, No. 2, 227-236, 1974.

[59] Rao, K. S., S. Raju, and J. R. Wang, "Estimation of soil moisture and surface

roughness parameters from backscattering coefficient," *IEEE Transactions on Geoscience and Remote Sensing*, Vol. 31, pp. 1094-1099, 1993.

[60] Rosenblatt, R., *Principles of Neurodynamics*, Spartan Books, New York, 1959.

[61] Rosenqvist, Å., and H. Oguma, "Phenological characteristics of cultivated vegetation covers in JERS-1 and ERS-1 synthetic aperture radar data," *Proceedings of International Symposium on Vegetation Monitoring*, pp. 194-198, Japan, August, 1995.

[62] Ruck, G. T., D. E. Barrick, W. D. Stuart, and C. K. Krichbaum, *Radar Cross Section Handbook, Vol. I*, Plenum Press, New York, 1970.

[63] Rumelhart, D. E., G. E. Hinton, and R. J. Williams, "Learning internal representation by error propagation," *Parallel Distributed Processing: Explorations in the Microstructure of Cognition. Vol. 1: Foundations*, MIT Press, Cambridge, 1986.

[64] Saatchi, S. S., D. M. Le Vine, and R. H. Lang, "Microwave backscattering and emission model for grass canopies," *IEEE Transactions on Geoscience and Remote Sensing*, Vol. 32, No. 1, pp. 177-186, Jan. 1994.

[65] Sabelfeld, K. K., *Monte Carlo Methods in Boundary Value Problems*, Springer-Verlag, 1991

[66] Seker, S. S., "Microwave backscattering from a layer of randomly oriented discs with application to scattering from vegetation," *IEE Proceedings H Microwave, Antennas and Propagation*, Vol. 133, No. 6, pp. 497-502, Dec. 1986.

[67] Shao, Y., C. Wang, X. Fan, and H. Liu, "Estimation of rice growth status using RADARSAT data," *Proceedings of the International Geoscience and Remote Sensing Symposium (IGARSS'97)*, pp. 1430-1432, Singapore, August, 1997.

[68] Shebell, M., "Modeling branching plants using attribute L-systems," *Master Thesis, Worcester Polytechnic Institute*, 1986

[69] Shin, R. T., and J. A. Kong, "Radiative transfer theory for active remote sensing of two-layer random medium," *Progress in Electromagnetics Research (PIER)*, J. A. Kong, Ed., Vol. 1, Chapter 4, Elsevier, New York, 1989.

[70] Smith, K. S., *Monte Carlo Methods, Their Role for Econometrics*, Lexington Books, 1973.

[71] Stofan, E. R., D. L. Evans, C. Schmullius, B. Holt, J. J. Plaut, J. van Zyl, S. D. Wall, and J. Way, "Overview of results of Spaceborne Imaging Radar-C, X-Band Synthetic Aperture Radar (SIR-C/X-SAR)," *IEEE Transactions on Geoscience and Remote Sensing,* Vol. 33, No. 4, 817-828, 1995.

[72] Tsang, L. and J. A. Kong, "Wave theory for remote sensing of a half-space random medium with three-dimensional variations," *Radio Science*, Vol. 14, No.

3, pp. 359-369, 1979.

[73] Tsang, L., J. A. Kong, and R. T. Shin, "Radiative transfer theory for active remote sensing of a layer of nonspherical particles," *Radio Science*, Vol. 19, pp. 629-642, 1984.

[74] Tsang, L., J. A. Kong, and R. T. Shin, *Theory of Microwave Remote Sensing*, Wiley-Interscience, New York, 1985.

[75] Tsang, L., Z. Chen, S. Oh, R. J. Marks, and A. T. C. Chang, "Inversion of snow parameters from passive microwave remote sensing measurements by a neural network trained with multiple scattering model," *IEEE Transactions on Geoscience and Remote Sensing*, Vol. 30, pp. 1015-1024, 1992.

[76] Tsang, L., C. Mandt, and K. H. Ding, "Monte Carlo simulations of the extinction rate of dense media with randomly distributed dielectric spheres based on solution of Maxwell's equations," *Opt. Lett.*, Vol. 17, No. 5, 314-316, 1992.

[77] Tsang, L., C. H. Chan, and K. Pak, "Backscattering enhancement of a two-dimensional random rough surface (three-dimensional scattering) based on Monte Carlo simulations," *Journal of the Optical Society of America A (Optics, Image Science and Vision)*, Vol. 11, 711-715, 1994.

[78] Tsang L., K.-H. Ding, G. Zhang, C. C. Hsu, and J. A. Kong, "Backscattering enhancement and clustering effects of randomly distributed dielectric cylinders

overlying a dielectric half space based on Monte-Carlo simulations," *IEEE Transactions on Antennas and Propagation,* Vol. 43, No. 5, pp. 488-499, May 1995.

[79] Tsang, L., J. A. Kong, K. H. Ding, and C. O. Ao, *Scattering of Electromagnetic Waves: Numerical Simulations*, Wiley-Interscience, New York, 2001.

[80] Ulaby, F. T., "Radar measurements of soil moisture content," *IEEE Transactions on Antennas and Propagation*, Vol. 22, pp. 257-265, 1974.

[81] Ulaby, F. T., R. K. Moore, and A. K. Fung, *Microwave Remote Sensing, Active and Passive, Vol. III*, Artech House, 1986.

[82] Ulaby, F. T., and M. A. El-Rays, "Microwave dielectric spectrum of vegetation—part II: dual-dispersion model," *IEEE Transactions on Geoscience and Remote Sensing,* Vol. 25, No. 5, pp. 550-557, September 1987.

[83] Wang, J. R., and T. J. Schmugge, "An empirical model for the complex dielectric permittivity of soils as a function of water content," *IEEE Transactions on Geoscience and Remote Sensing*, Vol. 18, pp. 288-295, 1980.

[84] Wang, L., R. T. Shin, J. A. Kong, and S. H. Yueh, "Application of neural network to remote sensing of soil moisture using theoretical polarimetric backscattering coefficients," *PIERS*, Pasadena, CA, July 1993.

[85] Wang, L., C. C. Hsu, J. A. Kong, J. C. Souyris, and T. Le Toan, "Inversion of forest biomass using neural networks," *IEEE International Symposium*, Toulouse, France, 1995.

[86] Wang, L., J. T. Johnson, C. C. Hsu, J. A. Kong, J. C. Souyris, and T. Le Toan, "Application of neural networks to the inversion of geophysical parameters," *PIERS*, Seattle, Washington, July 1995.

[87] Wang, L., K. H. Ding, C. C. Hsu, Y. E. Yang, and J. A. Kong, "Electromagnetic scattering model for vegetation based on L-systems," *PIERS*, Seattle, Washington, July 1995.

[88] Wang, L., Y. E. Yang, J. A. Kong, F. Del Frate, and D. Solimini, "Electromagnetic scattering from sunflower fields," *PIERS*, Boston, MA, July 1997.

[89] Wang, L., J. A. Kong, K. H. Ding, T. Le Toan, F. Ribbes-Baillarin, and N. Floury, "Electromagnetic scattering model for rice canopy based on Monte Carlo simulation," *Progress in Electromagnetic Research, PIER*, Vol. 52, pp. 153-171, 2005.

[90] Yueh, S. H., J. A. Kong, J. K. Jao, R. T. Shin, and T. Le Toan, "Branching model for vegetation," *IEEE Transactions on Geoscience and Remote Sensing*, Vol. 30, No. 2, pp. 390-402, March 1992.

[91] Zuniga, M., and J. A. Kong, "Active remote sensing of random media," *Journal of Applied Physics*, Vol. 51, No. 1, pp. 74-79, 1980.

[92] Zurada, J. M., *Introduction to Artificial Neural Systems*, West Publishing Company, St. Paul, 1992.

[93] Zurk, L. M. , L. Tsang, K. H. Ding, and D. P. Winebrenner, "Monte Carlo simulations of the extinction rate of densely packed spheres with clustered and non-clustered geometries," *Journal of the Optical Society of America A (Optics, Image Science and Vision)*, Vol. 12, pp. 1772-1781, 1995.